Investigation of Bragg Gratings in Few-Mode Fibers with a Femtosecond Laser Point-by-Point Technique

Tong Qiu

Dissertation submitted to the Faculty of the
Virginia Polytechnic Institute and State University
in partial fulfillment of the requirements for the degree of

Doctor of Philosophy
in
Electrical Engineering

Anbo Wang, Chair
Gary R. Pickrell
Yang (Cindy) Yi
Wei Zhou
Yizheng Zhu

December 09, 2021
Blacksburg, Virginia

Keywords: Few-mode fibers, fiber Bragg gratings, femtosecond laser, point-by-point, mode-division multiplexing

Investigation of Bragg Gratings in Few-Mode Fibers with a Femtosecond Laser Point-by-Point Technique

Tong Qiu

(ABSTRACT)

The higher-order modes (HOMs) of an optical fiber has been demonstrated as a new dimension to transmitting signals with the development of mode-division multiplexing (MDM) technique. This dissertation aims to explore the HOMs as an extra degree of freedom for device innovation. In particular, with femtosecond (FS) laser point-by-point (PbP) inscription technique which opens up a unique possibility to explore the HOMs for device innovation, we design, fabricate, and characterize novel-structured fiber Bragg gratings (FBGs) written in the step-index two-mode fibers. We also develop a numerical model for the PbP gratings which has the potential for inverse design problem.

Chapter 2 begins with a general framework of MDM with adaptive wavefront shaping in few-mode fibers (FMFs) and multimode fibers (MMFs), followed by two examples in slightly more detail. The fabrication setup and an short overview of the FS laser system will also be covered.

In Chapter 3, we show the design, fabrication, and characterization of off-axis Bragg gratings in a step-index two-mode fiber (TMF). Through measuring the transmission and reflection spectra along with the associated reflected mode intensity profiles under different input polarization, we experimentally investigate the off-axis TM-FBGs (FBGs in a TMF) with multiple characteristics reported for the first time to our best knowledge. To highlight, we report the laser-induced birefringence exhibits strong offset dependence, the reflectivity heavily depends on the offset and polarization, and particularly the mode pattern can be

controlled solely through polarization.

The design and characterization of cross-axis TM-FBGs are presented in Chapter 4. Specifically, these gratings show six primary reflection peaks, which are identified through mode-decomposition based on the intensity profiles through nonlinear optimization problem. We also show in this chapter the development of a numerical model for the general PbP gratings, implementation of this model into standard coupled-wave analysis shows reasonable agreement to the experimental findings.

In Chapter 5, discussions and suggestions for future studies are given.

Investigation of Bragg Gratings in Few-Mode Fibers with a Femtosecond Laser Point-by-Point Technique

Tong Qiu

(GENERAL AUDIENCE ABSTRACT)

The higher-order modes (HOMs) of an optical fiber has been demonstrated as a new space for signal transmission, in the "mode space" one can use the modes as distinct multiplexing channel and therefore increase the data capacity of a single fiber. This work aims to explore if the the higher-order modes can also add some extra degree of freedom for device innovation. In particular, we use femtosecond (FS) laser point-by-point (PbP) technique for device fabrication, since the structural change induced by this fabrication methods is highly localized, typically ranging from a few hundred nanometers to a few micrometers. Hence this particular fabrication technique offers a unique possibility of exploiting the HOMs for device innovation. In this work, we fabricate, and characterize fiber Bragg gratings (FBGs) with novel structural designs written within the step-index two-mode fibers, with multiple characteristics reported for the first time as far as we know. We also develop a numerical model for the PbP gratings which has the potential for inverse design problem.

Dedication

To my parents for your love and everything

Acknowledgments

During my six-and-half-year of PhD studies, there are a lot of people I would like to thank. Foremost, I would like to express my greatest gratitude to my advisor Dr. Anbo Wang, who gave me a free but instructive environment to pursue my PhD degree, shared with me his invaluable wisdom about research and life, and entirely reshaped my research vision: He has taught me how to be a real researcher capable of driving independent research.

My sincere thanks also goes to the rest of my committee: Dr. Gary R. Pickrell, Dr. Yang (Cindy) Yi, Dr. Wei Zhou, and Dr. Yizheng Zhu, for those inspirational discussions we had about research and/or coursework. I also thank Dr. Xiaoting Jia for her support in the past summer and during my preparation for future career.

I would also like to express my heartfelt gratitude to Dr. Yong Xu, who led me into the area of scientific research, supported and supervised me in my first two and half years.

I also thank Dr. Daniel Homa for the support in Summer 2020, Dr. Islam Ashry and Dr. Peng Lu for their help when I was a fresh PhD student, Dr. Shuo Yang for training me using femtosecond laser system and countless discussions on research; and all of my colleagues, Logan Theis, Guannan Shi, Ruixuan Wang, Dr. Jiaji He etc. for the discussions, suggestions, and help. I am also grateful to the Physics department and ECE department for offering me teaching assistantship over these years.

Personally, I would like to thank my boyfriend for his consistent encouragement, support in every aspect, and accompanying through these years.

Lastly, I give my deepest gratitude to my parents, for their supports, for raising me up in such a nice way, for their love and everything.

Contents

List of Figures

List of Tables

List of Abbreviations

AO Adaptive Optics

BS Beam Splitter

DAQ Data Acquisition

DM Deformable Mirror

DMG Degenerate-Mode Group

DoLP Direction of Linear Polarization

FBG Fiber Bragg Grating

FMF Few-Mode Fiber

FS Femtosecond

LP Linearly-Polarized (refer to the linearly-polarized modes)

MDM Mode-Division-Multiplexing

MEMS Micro-Electromechanical system

MMF Multimode Fiber

PbP Point-by-Point

PD Photodiode

RIM Refractive Index Modulation

SLM Spatial Light Modulator

SM Single-Mode

SMF Single-Mode Fiber

TMF Two-Mode Fiber

TS Ti:Sapphire

UV Ultraviolet

Chapter 1

Introduction

1.1 Motivation

Recently, few-mode fibers (FMFs) and multimode fibers (MMFs) have seen significant attention for their applications in optical communication, sensing, and imaging, mainly stimulated by the development of the technique of mode-division multiplexing (MDM). Similar to wavelength-division multiplexing [1] that uses different wavelengths as independent data-carrying channel, MDM utilizes individual guided fiber modes as distinct multiplexing channels. To achieve good performance for the MDM-based applications, one must develop strategies that can reduce the impact of intermodal coupling and control the propagation of the optical signal along a fiber. My previous work has experimentally realized selective mode excitation in FMF/MMFs under the framework of adaptive optics (AO), which treats the entire optical system as a black box if a proper feedback signal can be identified, and therefore requires no prior system knowledge and inherently has higher tolerance to the ambient disturbance, as compared to the setups based on computer-generated holography, pre-calibration of transfer matrix, digital phase conjugation [2, 3, 4], etc. In short, researchers including us have demonstrated that the fiber modes can add a new dimension (from the "mode space") to further pushing the limit of data transmission capacity. However, to the best of our knowledge, it remains almost-unexplored whether the fiber modes can also introduce extra degree of freedom for device innovation from the fabrication point-of-view.

In general, to exploit in the "mode space" of the optical fiber from the angle of device fabrication, one needs to employ a certain fabrication technique with featured footprint in the level of a few micrometers. This is because the fiber core where the guided modes are mostly presented typically ranges from ∼4 µm to ∼100 µm, it is likely that only a footprint with comparable or even smaller featured size is capable of distinguishing varied fiber modes. Consequently, thanks to the multi-photon process and ultra-short pulse duration [5], femtosecond (FS) laser point-by-point (PbP) inscription technique opens up a unique possibility of experimentally investigating the potential extra-dimension of device innovation added by the higher-order modes (HOMs) of the optical fibers.

Fiber Bragg gratings (FBGs) are one of the key passive components for various optical systems ranging from telecommunication, fiber sensing, to fiber laser technology [6, 7, 8, 9, 10, 11, 12, 13, 14, 15, 16], etc. In general, an FBG is created by periodic perturbations to the fiber along the propagation direction, hence its spectral response can be featured by one or multiple narrow-band reflection peaks, depending on the number of modes that can interact with the periodic structure; the reflection peaks are formed by either the self-coupling of an individual mode, or by the cross-coupling of two modes, as a result of phase-matching condition [17]. Furthermore, there are primarily two conditions that can quantify the spectral response of an FBG, one is the phase-matching condition that involves the grating pitch and determines the spectral location of the reflection peak. The other one, of our particular interest, is the 2D integral of the transverse overlap between the perturbation and the electric fields of the two fiber modes being studied, the two modes can be the same or not. The HOMs, with varied spatial distributions, can therefore induce variations to the 2D integral, and hence have the potential to modify the properties of an FBG. In addition, the FBG in FMF/MMFs are also a natural mode separator which has been demonstrated for MDM-based applications as outlined in one of my previous work [18].

1.2 Summary of dissertation

This work aims to demonstrate the HOMs of an optical fiber can add a new dimension to device innovation. In particular, with FS laser PbP inscription technique, we fabricated and characterized FBGs with novel structural designs in a step-index two-mode fiber (TMF), with multiple characteristics reported for the first time to our best knowledge. Specifically, to fully characterize the HOMs, we designed and constructed a free-space spectrometer/imaging system that can deterministically control the wavelength and polarization of the incident beam, and alter the excitation conditions at the input end of the TMF. We also developed a numerical model of PbP gratings that can be used for the synthesis of PbP grating with more complicated structural design and more fiber modes involved. It should be noted that we present our results on the basis of Linearly-polarized (LP) mode group but with polarization and spatial degeneracies considered, as a balance between the LP approximation and the true vector eigenmodes [19].

This report is organized as follows:

- Chapter 2 gives a brief overview over the general principles behind MDM under the framework of AO with two examples in slightly more detail, followed by another overview over the FS laser system we used for fabrication.
- Chapter 3 contains detailed characterization results of the off-axis TM-FBGs, as well as qualitative analyses on the gratings based on finite-difference time domain (FDTD) simulation conducted with commercial software.
- In Chapter 4, we show the experimental measurements of the cross-axis TM-FBGs as well as the development of a numerical model for the PbP gratings.
- Chapter 5 describes the conclusion and future work.

1.3 List of Publications

(Corresponding author*)

[1] **T. Qiu**, I. Ashry, A. Wang, and Y. Xu*, "Adaptive mode control in 4-and 17-mode fibers," IEEE Photonics Technology Letters, vol. 30, no. 11, pp. 1036-1039, 2018.

[2] **T. Qiu**, I. Ashry, A. Wang, and Y. Xu*, "Adaptive control of degenerate mode groups in a highly multimode fiber," IEEE Photonics Technology Letters, vol. 30, no. 22, pp. 1976-1979, 2018.

[3] **T. Qiu***, S. Yang, and A. Wang, "Experimental investigation of point-by-point off-axis Bragg gratings inscribed by a femtosecond laser in few-mode fibers," Optics Express, vol. 28, no. 25, pp. 37553-37565, 2020.

[4] **T. Qiu***, S. Yang, and A. Wang, "Cross-axis Bragg gratings in few-mode fibers inscribed with a femtosecond laser point-by-point technique," (under review)

Chapter 2

Research Background

We start this chapter with a brief overview over the general principles behind mode-division multiplexing (MDM) under the framework of adaptive optics (AO) in few-mode and multi-modes fibers, with two examples in slightly more detail. We then give an introduction to the FS laser system (Coherent Libra series) we used for FBG fabrication.

2.1 Mode-division multiplexing with adaptive optics

Optical fibers are one of the key components in various optical systems, ranging from telecommunication, fiber sensing, biomedical imaging, to fiber laser technology, etc. In order to improve the data transmission capacity of a single optical fiber, several multiplexing techniques have been proposed and studied since decades ago, such as wavelength-division multiplexing and time-division multiplexing [1, 20]. Recently, few-mode fibers (FMFs) and multimode fibers (MMFs) have attracted renewed interest with the development of MDM technique, which utilizes individual guided fiber mode as distinct multiplexing channel [21, 22]. An extension of such concept to fiber sensing results in simultaneous multi-parameter sensing [23, 24], provided that individual fiber mode can respond differently to the ambient environment. However, one of the practical issues one need to address for the MDM-based applications is the random and unpredictable inter-modal coupling which can significantly complicate the data processing [25]. It is therefore desirable to have the capability of con-

trolling the propagation of optical signals in the fibers.

To date, numerous mode control techniques have been successfully demonstrated, such as those based on computer-generated holography [2, 26], phase plates [21, 22], photonic lanterns [27, 28], and fiber Bragg gratings (FBGs) [18, 29], to name just a few. Adaptive mode control treats the entire optical system as a black box with a proper feedback signal pre-defined, and hence requires no prior system knowledge. Furthermore, it inherently has higher tolerance to the ambient disturbance since the feedback is provided by the ambient environment and can be updated in real time.

Figure 2.1 depicts a schematic of a general adaptive mode control system, where a spatial light modulator (SLM) is used for adaptive wavefront shaping. In particular, a collimated

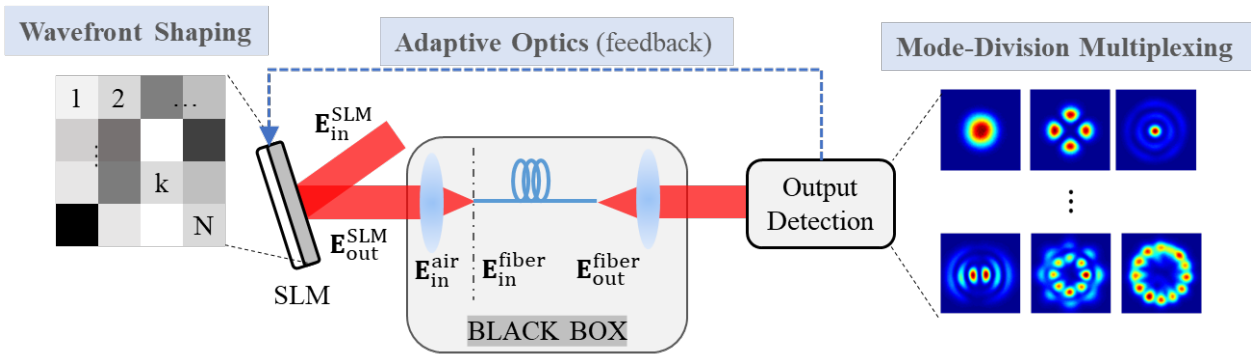

Figure 2.1: Schematic of adaptive mode control system in general. SLM: Spatial light modulator.

incident beam $\mathbf{E}_{\text{in}}^{\text{SLM}}$ is modulated on the surface of an SLM displaying certain "phase map" (illustrated as the blocks in gray scale, colors represent different phase shifts). The collimated beam is then transmitted into the "black box" which is an optical fiber with a focusing lens in our case. Certain output of the black box is detected and monitored in real time, and in turn it can provide a feedback signal to the spatial light modulator (SLM) to update the phase map shown on and modulate the optical wavefront in an adaptive manner.

2.1.1 Wavefront shaping and selective mode excitation

We now give a brief derivation of the mathematical relationship between the phase map on the SLM and the selective mode excitation at the fiber output end, this derivation is general regardless of the feedback signal one might be using. We may start with the spatial light modulator, which shows a block-wised phase map. A block represents a group of identical pixels for the SLM based on nematic liquid crystals [30], or an individual actuator for the ones based on micro-electromechanical system (MEMS) [18]. The phase map can in general be expressed as

$$V(x,y) = \sum_{k=1}^{N} v_k s_k(x,y), \tag{2.1}$$

where v_k is the phase shift of the k-th block of the SLM, taking the form of $\exp(j\phi_k)$ for a phase-only SLM; $s_k(x,y)$ is a logic function, true for and only for the regions within the k-th block:

$$s_k(x,y) = \begin{cases} 1 & (x,y) \text{ within the } k\text{-th block} \\ 0 & \text{otherwise.} \end{cases} \tag{2.2}$$

The modulated beam reflected off the surface of the SLM is therefore:

$$\begin{aligned} \mathbf{E}_{\text{out}}^{\text{SLM}}(x,y) &= \mathbf{E}_{\text{in}}^{\text{SLM}} V(x,y) \\ &= \mathbf{E}_{\text{in}}^{\text{SLM}} \sum_{k=1}^{N} v_k s_k(x,y) \\ &= \sum_{k=1}^{N} v_k \mathbf{E}_k(x,y), \end{aligned} \tag{2.3}$$

where $\mathbf{E}_k(x,y)$ signifies the collimated beam incident on the k-th block of the SLM, which is expressed as

$$\mathbf{E}_k(x,y) = \mathbf{E}_{\text{in}}^{\text{SLM}} s_k(x,y). \tag{2.4}$$

Without loss of generality, here we assume a collimated beam after phase modulation, and only consider the focusing of the lens and Fresnel diffraction between the lens and the fiber input, the optical field in free-space right before coupled into the fiber is therefore:

$$\begin{aligned}\mathbf{E}_{\text{in}}^{\text{air}}(x',y') &= \mathbb{L}\Big[\mathbf{E}_{\text{out}}^{\text{SLM}}(x,y)\Big] \\ &= \sum_{k=1}^{N} v_k \mathbb{L}\Big[\mathbf{E}_k(x,y)\Big].\end{aligned} \tag{2.5}$$

$\mathbb{L}[.]$ denotes the linear transformation of the focusing lens with transmittance $t(x,y)$ and the Fresnel diffraction in free-space:

$$\mathbb{L}\big[\mathbf{E}_k(x,y)\big] = \frac{e^{jkz}}{j\lambda z}\iint \mathbf{E}_k(x,y)t(x,y)\exp\left\{j\frac{k}{2z}\left[(x'-x)^2+(y'-y)^2\right]\right\}dx\,dy. \tag{2.6}$$

Such an optical field $\mathbf{E}_{\text{in}}^{\text{air}}$ is then coupled into the eigenmodes of the fiber under test, and hence the optical field right after coupled into the fiber can be expressed as

$$\begin{aligned}\mathbf{E}_{\text{in}}^{\text{fiber}}(x',y') &= \sum_{n=1}^{M} c_n \mathbf{e}_n(x',y') \\ &= \sum_{n=1}^{M} \mathbf{e}_n(x',y') \sum_{k=1}^{N} v_k a_{kn},\end{aligned} \tag{2.7}$$

in which c_n describes the coupling strength of the incident free-space field to the n-th eigenmode with electric and magnetic fields respectively denoted as $\mathbf{e}_n$ and $\mathbf{h}_n$:

$$c_n = \iint \mathbf{E}_{\text{in}}^{\text{air}}(x',y') \times \mathbf{h}_n^*(x',y') \cdot \vec{e}_z\, dx'\, dy', \tag{2.8}$$

and accordingly, the coefficient a_{kn} can be expressed as

$$a_{kn} = \iint \mathbb{L}\big[\mathbf{E}_k(x,y)\big] \times \mathbf{h}_n^*(x',y') \cdot \vec{e}_z\, dx\, dy. \tag{2.9}$$

The output optical field of an ideal fiber can hence be obtained by multiplying a corresponding constant phase term $\exp(j\beta_n z)$ to the n-th eigenmode, here we implicitly include such phase shifts in to the a_{kn}. The ultimate output fields of the optical fiber $\mathbf{E}_{\text{out}}^{\text{fiber}}(x', y')$ therefore takes similar form as (2.7), which is a linear superposition of the fiber eigenmodes, weighted by the block-wised phase map $V(x, y)$ of the SLM. For example, for an optical fiber supporting 3 modes, and an SLM with 2 blocks, we can write:

$$\mathbf{E}_{\text{out}}^{\text{fiber}} = (a_{11}v_1 + a_{12}v_2)\mathbf{e}_1 + (a_{21}v_1 + a_{22}v_2)\mathbf{e}_2 + (a_{31}v_1 + a_{32}v_2)\mathbf{e}_3. \tag{2.10}$$

2.1.2 Examples of adaptive mode control in FMF/MMFs

In this section, we present two examples using different feedback signals to adaptively modulate the optical wavefront of the incident beam as shown in Fig. 2.1.

Feedback based on the image correlation

Figure 2.2 shows the schematic of the adaptive mode control system based on image correlation. A single mode fiber-coupled laser diode at 660 nm is generates a continuous wave. A liquid-crystal-based SLM (active area: 6.2mm by 6.2mm, 9 by 9 blocks) is used for wavefront shaping via varying the effective refractive index seen by the incideny beam. Accordingly, a linear polarizer is required, as the SLM requires alignment between the polarization of the incident beam and the slow axis of the liquid crystal molecules to achieve the optimal performance. The near-field at the output end of the fiber is captured a CCD, based on

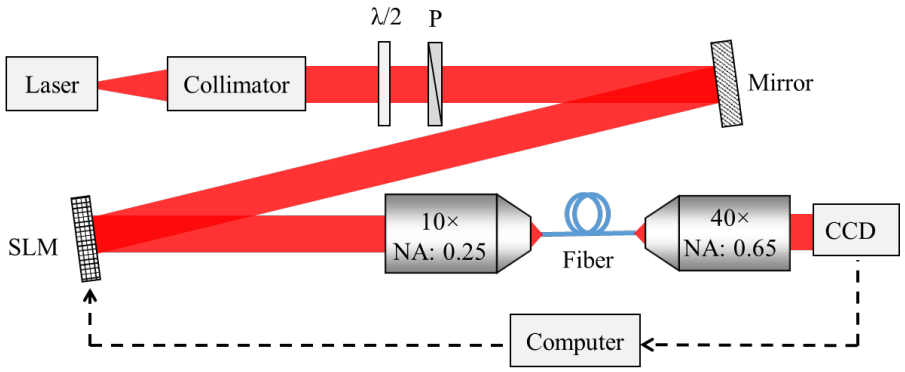

Figure 2.2: Schematic of the experimental setup. $\lambda/2$: Half-wave plate; P: Linear polarizer; SLM: Phase-only spatial light modulator based on liquid crystal.

which we define the feedback signal as

$$f(k) = 1 - \frac{\sum_{x,y} \left(I_0(x,y) - \bar{I}_0\right)\left(I_k(x,y) - \bar{I}_k\right)}{\sqrt{\sum_{x,y} \left(I_0(x,y) - \bar{I}_0\right)^2 \sum_{x,y} \left(I_k(x,y) - \bar{I}_k\right)^2}}, \tag{2.11}$$

where (x, y) represents the pixels of the CCD, I_0 is the intensity profile of the target mode (or mode superposition), I_k denote the captured image. $f(k)$ varies between 0 and 1, when $f(k) = 0$, I_0 and I_k are identical regarding their shape and relative intensity, our goal is therefore to minimize this feedback function. We sequentially modulate the phase map on the SLM block by block. At each block, we tune the phase shift at discrete value between 0 and 2π, for each of the phase shift we calculate $f(k)$, and keep the phase shift that has the minimum $f(k)$ value for this particular block. After all the blocks are updated once, we start a new cycle, and repeat the block-by-block and stepwise phase shifting.

A four-mode fiber (SMF28) and a step-index seventeen-mode fiber (19 µm core diamter, NA: 0.12) are tested, both fiber are $\sim$ 2 m long. The optimization results after nine optimization cycle are shown in Figs. 2.3 and 2.4, respectively. The initial and optimized fields are captured by the CCD, the target is the intensity profile of the desired LP mode calculated

in prior with MATLAB. As an instance, we display in Fig. 2.5 the optimized phase map

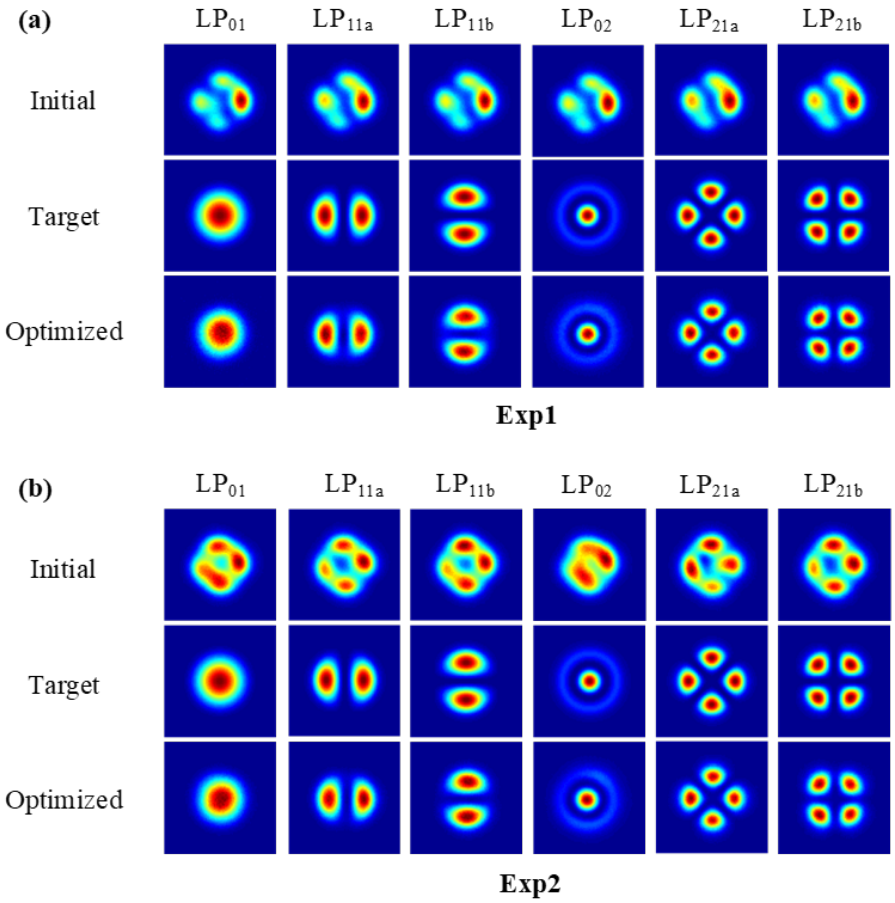

Figure 2.3: Selective mode excitation in a step-index four-mode fiber for (a) Exp1 and (b) Exp2 with different initial fields.

displayed on the SLM for the selective excitation of the LP+11a. White represents $\sim 2\pi$ phase modulation and black for 0.

In Figs. 2.6 and 2.7, we show the evolution of the feedback function during the optimization process. Note that the seventeen-mode fiber in general has a higher value of the optimized $f(k)$, this is primarily because we used the same 9 by 9 blocks (refer to Fig. 2.5 for example), whereas as suggested by Eq. (2.7), for an optical fiber with more modes, a more complicated weights combination and hence more SLM blocks are desired.

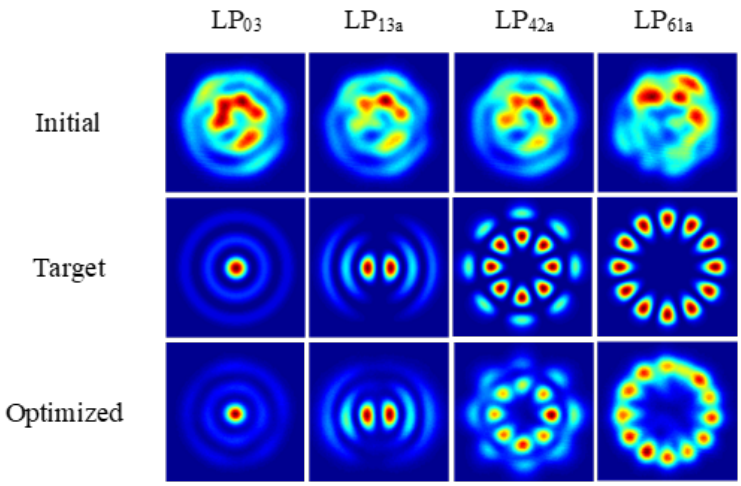

Figure 2.4: Selective mode excitation in a step-index seventeen-mode fiber.

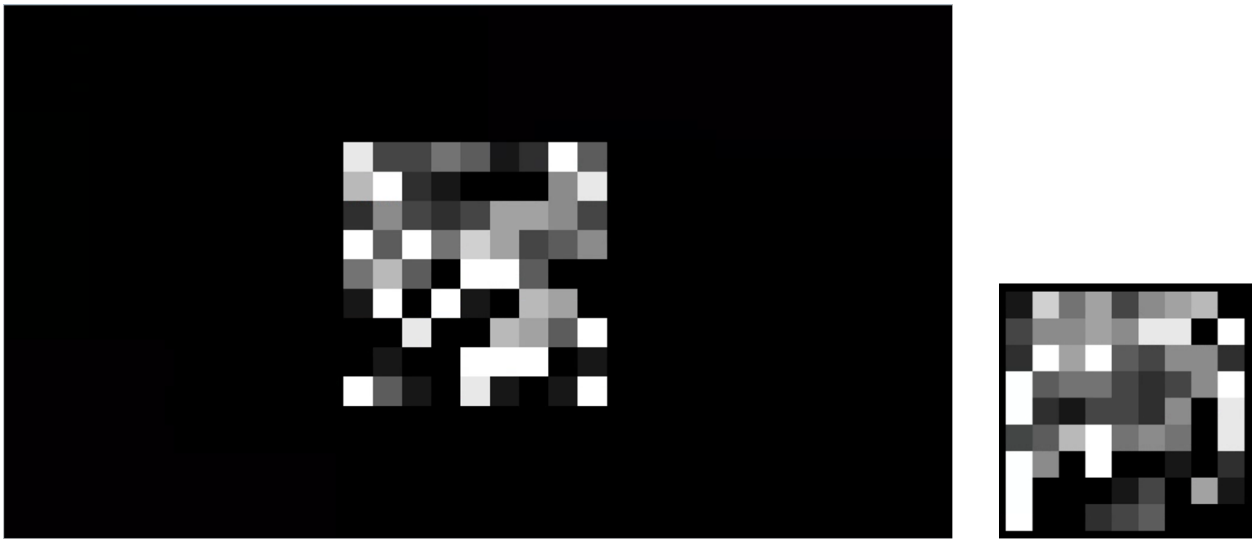

Figure 2.5: Representative phase maps after optimization for the selective excitation of the LP+11a in (a) Exp1 and a clip of the functioning area in (b) Exp2. White: $\sim 2\pi$: black: 0.

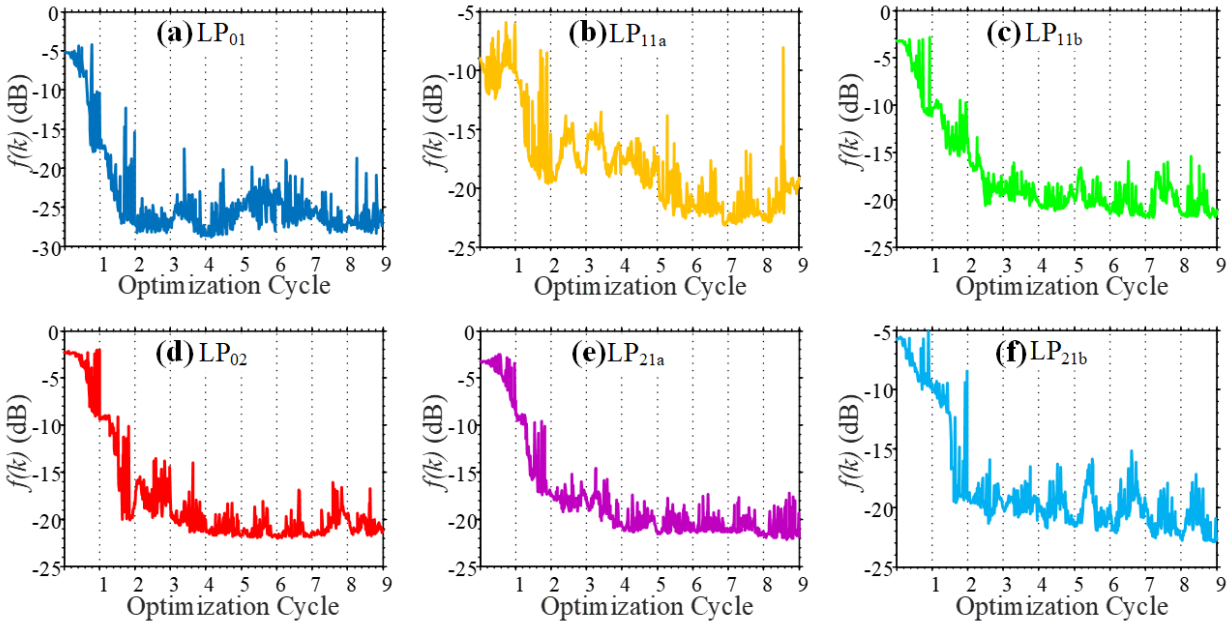

Figure 2.6: Variation of the feedback function during nine optimization cycles for the four-mode fiber in Exp1.

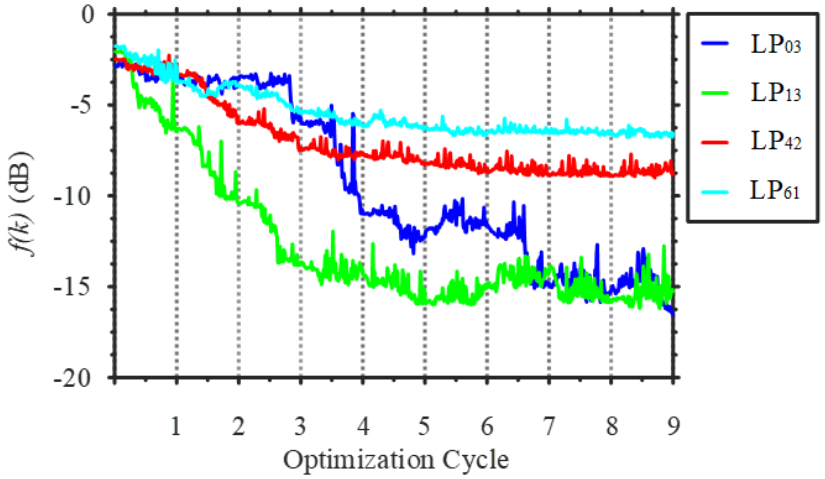

Figure 2.7: Variation of the feedback function during nine optimization cycles for the seventeen-mode fiber.

Feedback based on the FBG

In addition to the image correlation, the feedback function in Fig. 2.1 can also take other forms. For example, in Fig. 2.8, the feedback function is defined as one proportional to the optical power reflected by the MM-FBG (FBG in an MMF). In this case, an MEMS-based

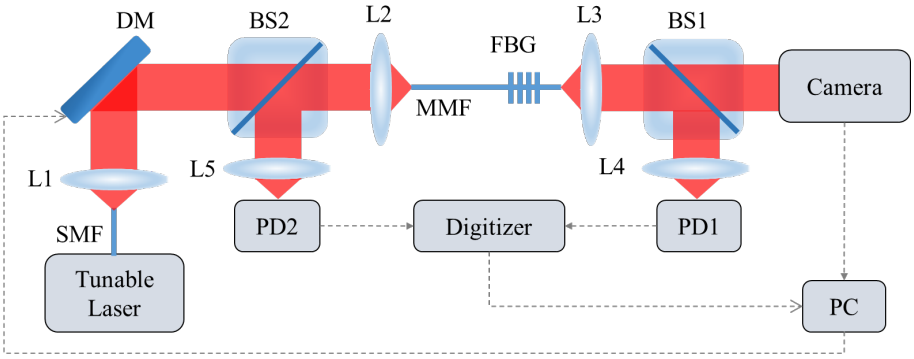

Figure 2.8: Experimental setup for MM-FBG-based adaptive mode control. DM: Deformable mirror; L1: Collimator, NA = 0.24; PD: Photodiode; L2 and L5: 10× objective lens, NA = 0.25; L3: 100× objective lens, NA = 0.9; L4, 20× objective lens, NA = 0.4.

deformable mirror(DM) is used for wavefront modulation through inducing optical path length variation. The DM has 12 by 12 independent actuators (140 active and 4 inactive at four corners) in total, each actuator covers an area of 400 µm by 400 µm. The collimated beam is modulated by the DM and then coupled into the MMF (∼1.2 m in length) with an FBG inscribed near the output end. The transmitted signal is captured by a photodide (PD1) and a camera; while the FBG-reflected signal is detected by another photodiode (PD2). The feedback function F is therefore defined as P_2/P_1 (the optical power detected by PD2 over that of PD1), which physically represents the optical signal reflected by the grating normalized to the total transmitted power. The normalization is to mitigate the undesired wavefront modulation aiming to optimizing the Fresnel reflection. In this case, our goal is to maximize the feedback function. To do so, we first fix the wavelength to the Bragg wavelength of the desired mode to be excited. In Fig. 2.9, we show a typical reflection

spectrum of an MM-FBG, note that this MM-FBG measured in Fig. 2.9 is not the MM-FBG we used in Fig. 2.8, but those two have similar spectral response. As revealed in Fig. 2.9,

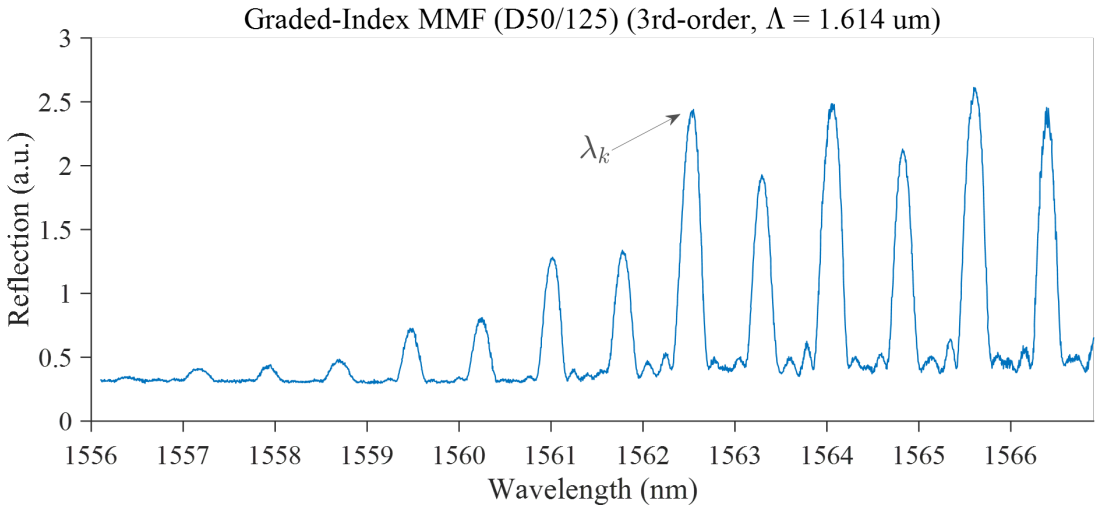

Figure 2.9: Representative reflection spectrum of an FBG inscribed in a graded-index MMF.

multiple reflection peaks are presented, each peak corresponds to either the self-coupling of one mode or the cross-coupling of two modes. For example, at the Bragg wavelength of the self-coupling of the k-th mode λ_k as marked in the plot, ideally, only the k-th mode can be reflected, all other modes propagate as in a pristine fiber. Therefore, if the reflection at λ_k is maximized, the proportion of the k-mode will be maximized accordingly. Since the FBG is close to the distal end of the fiber, the near-fields of the fiber will be dominated by the k-th mode.

With similar sequential update of the phase map on the DM as in section 2.1.2, the resulting selective mode excitation is shown in Figs. 2.10–2.12, where "Init." represent the initial optical fields, and "Opt." the optimized optical fields. Unlike the step-index four- and seventeen-mode fibers in which we can selectively excite an LP mode, for the graded-index highly MMFs, the LP modes with similar propagation constant are further grouped into degenerate-mode groups. Presented in Figs. 2.10–2.12 the three mode orders ($N = 1, N = 4$, and $N = 8$) are referring the degenerate-mode groups, whose intensity profiles are physically

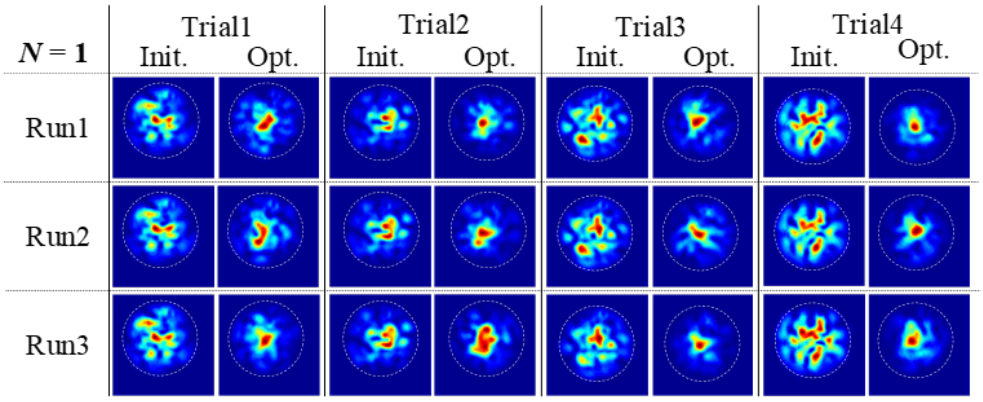

Figure 2.10: Results of adaptive control of degenerate-mode group $N = 1$ (low-order).

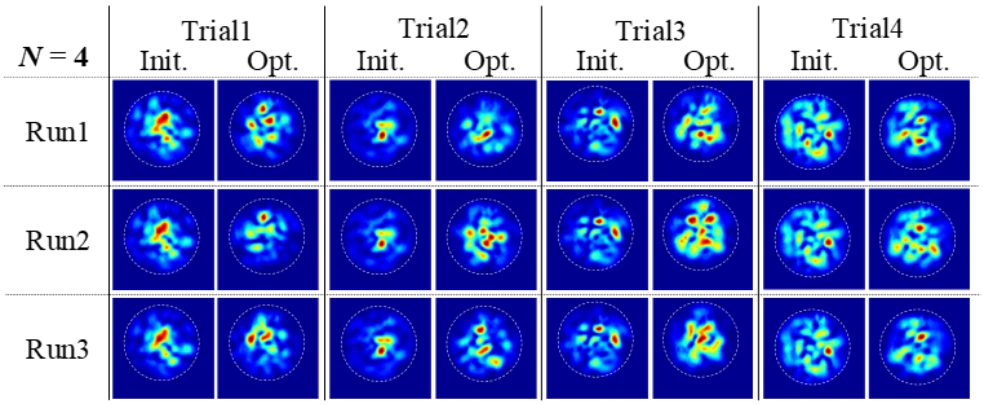

Figure 2.11: Results of adaptive control of degenerate-mode group $N = 4$ (intermediate-order).

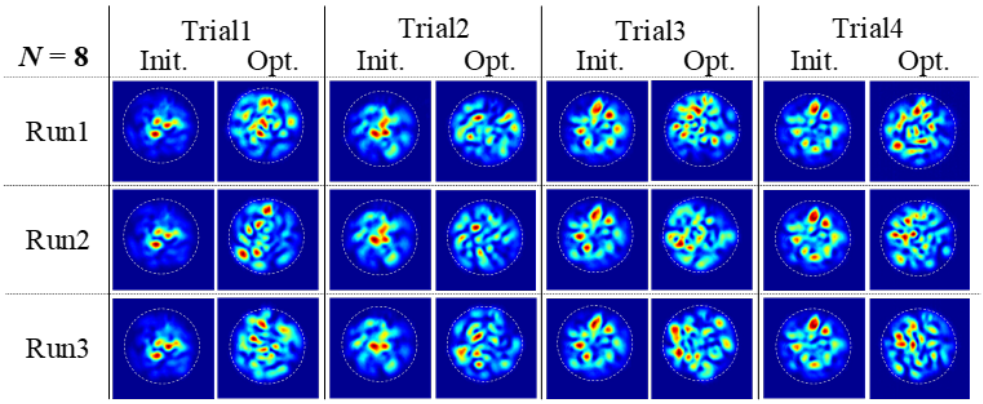

Figure 2.12: Results of adaptive control of degenerate-mode group $N = 8$ (high-order).

coherent superposition of multiple LP modes. A representative optimized phase map of Exp2-Trial2-Run1 is shown in Fig The evolution of the feedback function of

Figure 2.13: Representative phase map after optimization for Exp3-Trial2-Run2. White: $\sim 2\pi$: black: 0.

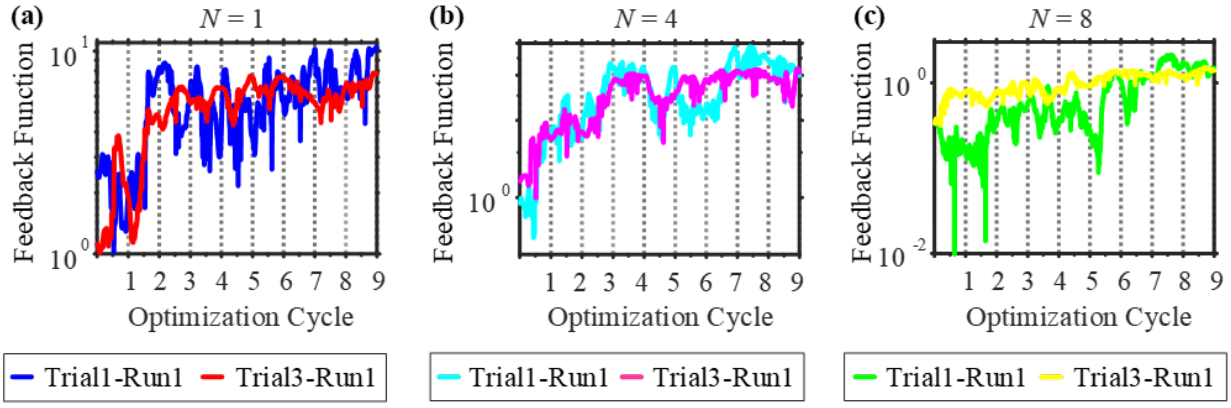

Figure 2.14: Variation of the feedback function during nine optimization cycles.

2.2 FS laser PbP inscription

In addition to serving as the mode separator for MDM-based applications, FBG itself has also been widely used in numerous optical systems as spectral filters, wavelength selectors,

and sensing elements [31, 32, 33, 34, 35, 36, 37]. FBGs are conventionally fabricated by ultraviolet (UV) irradiation after photo-sensitization (hydrogen loading) [38]. With a phase mask [39], the resulting UV-induced structural change is typically continuous along the grating length and uniform across the core region in the transverse plane perpendicular to the fiber axis; even with point-by-point (PbP) inscription using an excimer laser reported in 1993 for the first time [40], the UV irradiation still results in a large laser-modified volume. Unlike the aforementioned conventional FBG inscription methods, femtosecond (FS) laser PbP technique [41] leads to highly localized structural change, typically at the level of a few hundred nanometers to a few micrometers, and hence offers the possibility of exploring the potentially novel properties induced by the varied spatial distributions of the higher-order modes (HOMs).

2.2.1 Experimental setup for FBG fabrication

Figure 2.15 presents the schematic of the experimental setup used for FBG fabrication in this work. A Ti:Sapphire (TS) FS laser with an additional regenerative amplifier (also based on TS rod) operates at a center wavelength of 800 nm. A Gaussian beam pulse chain (beam waist: 3 mm; pulse width: $\sim$ 100 fs) is emitted with repetition rate (f_{rep}) set at 500 Hz. A linear polarizer is used to control the polarization of the pulse chain, and a half-wave plate ($\lambda/2$) is employed to fine-tune the energy per pulse accordingly. The single-pulse energy is tuned to 128 nJ, which is slightly above the damage threshold of the glass induced by a single pulse but without significant cracks [42]. The pulse chain is then focused into an optical fiber by an oil-immersion objective (100×, NA: 1.25). The index of the oil is chosen primarily to match the refractive index of the cladding of the fiber (after removing the coating) [43]. The fiber under fabrication is mounted on an air-bearing translation stage, which can tilt around x- and y-axes and linearly translate in x-, y-, and z-axes, as shown in the figure. A periodic

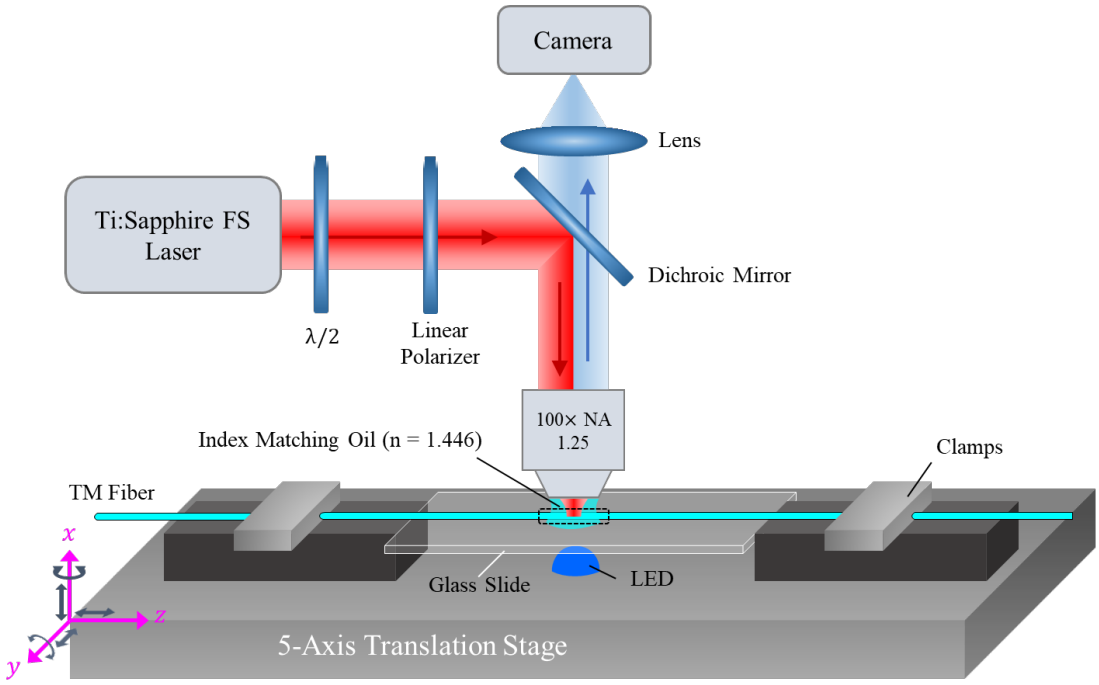

Figure 2.15: Schematic of the experimental setup for FBG fabrication. $\lambda/2$: half-wave plate.

structure can therefore be induced into the fiber by traversing the stage at a constant speed v_{stage} along certain direction, depending on the specific structure. The grating pitch Λ can be identified through

$$\Lambda = \frac{v_{\text{stage}}}{f_{\text{rep}}}. \tag{2.12}$$

In the meantime, the inscription process is monitored in real time through a transmitted bright-field optical microscopy system, this system is constructed by a blue LED, the same objective lens used for fabrication, and a CCD camera, separated from the FS pulses by a dichroic mirror.

2.2.2 Overview of the FS laser system (Coherent Libra)

The FS laser system we used consists of three major parts, a seed laser, a regenerative amplifier, and a system of chirped pulse amplification [44]. In this section, we provide a

short overview of the three sub-systems.

Seed laser

The seed laser consists of two major parts, a TS rod as the gain medium and a pump laser. The pump laser is based on the Nd-doped Yttrium Orthovanadate (Nd:YVO4) as the gain medium pumped by 808 nm laser diodes. Nd:YVO4 generate continuous wave at 1064 nm after certain frequency filtering; through second-harmonic generation in an LBO crystal, the emitting wavelength is halved to 532 nm. The 532 nm continuous wave is used for optically pumping the TS rod. TS crystals possess a relatively broad gain profile thus enabling the generation of ultrashort pulses. In addition, mode-locking is also required for ultrashort pulse generation in order to have all the longitudinal modes interfering constructively. In general, mode-locking can be achieved by periodic loss modulation, which at the same frequency of the spectral spacing of the longitudinal modes. One may qualitatively interpret the loss modulation as a trigger that enables the coupling of adjacent longitudinal modes, with gain competition, it ultimately leads to phase-locked longitudinal modes. The resulting pulse chain from the seed laser has repetition rate at 80 MHz, pulse width of $\sim$100 fs, average power greater than 250 mW, and is horizontally polarized.

Regenerative amplifier

The regenerative amplifier is in fact a cavity containing another TS rod, which is pumped by a pulsed laser with Nd:LiYF4 as gain medium. Similar to the Nd:YVO4 used for the seed laser, the Nd:LiYF4 is also optically pumped by laser diodes (AlGaAs). Through acousto-optic Q-switching at 1 kHz, it emits pulsed wave with high average power at 1053 nm. The wavelength is then halved by another LBO crystal to 527 nm with sufficient conversion

efficiency due to the high intra-cavity 1053 nm radiation fluence. The ultimate output of the Nd:LiYF4 pump laser is a horizontally polarized pulse chain with 1 kHz repetition rate, 20 W average power, and 100–350 ns pulse duration.

The 527 nm pulsed wave then optically pumps the TS rod, which is used to regeneratively amplify the seed pulse, the word "regenarative(ly)" represents that the amplification is achieved by multiple round-trips through the TS rod inside the cavity. In particular, from the 80 MHz seed pulse chain, the cavity periodically "picks" one single pulse and trap it inside the cavity. The frequency of the seed pulse picking can be modulated, but it must be smaller than the repetition rate of the pulsed pump (Nd:LiYF4 for the TS rod used here). After multiple (usually 8–10) round-trips the amplified seed pulse is then released from the cavity. One round-trip takes ∼9 ns in our system. The trapping of the seed pulse inside the amplifier cavity is realized by a pair of Pockels cells through modulating the polarization of the incident beam. The timing control of the regenerative amplification cavity is crucial, including the synchronization between the pump pulse and the pick-up of the seed pulse, the time delay between the pump pulse and the gain profile development of the TS rod (i.e., timing of the first Pockels cell), number of round-trips inside the amplifier cavity (i.e., timing of the other Pockels cell), etc.

Chirped pulse amplification

Before the seed pulse enters the regenerative amplification cavity and gets amplified, there is in fact another important step we skipped in the last part. The seed pulses firstly pass through a stretcher to broaden its time duration and therefore lower down its peak power. A stretcher is typically constructed by diffraction gratings that reflect different wavelengths at different angles and hence different time of flight. With proper designs and precise optical alignment, the seed pulses after the stretcher is designed to bear no spatial chirp, since the

spatial chirp is detrimental to the components inside the regenerative cavity and degrade the pulse quality. In turn, after the amplified seed pulse exits the regenerative amplifier, it then passes through a compressor as the last step. A compressor is constructed similarly to the stretcher, but aims to recover the pulse duration of the original seed pulse (∼100 fs). Figure 2.16 shows the experimentally measured spectra of the seed pulses before the stretcher and after the compressor. The full width at half maximum of the red trace is

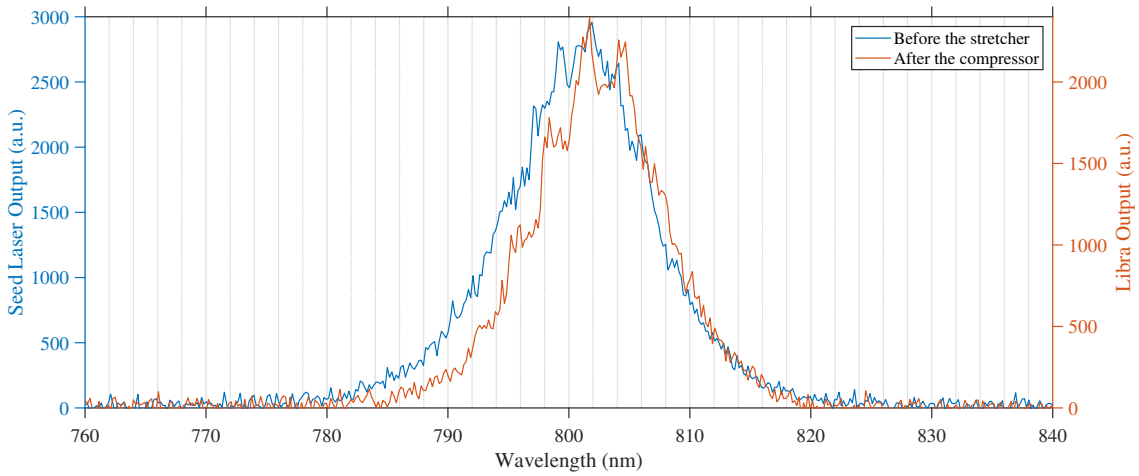

Figure 2.16: Spectra of the seed pulses measured by a USB4000.

slightly narrower than that of the blue trace, particular at the shorter wavelengths. This can be due to certain optical misalignment, and might cause pulse width broadening to some extent.

Chapter 3

Off-Axis TM-FBGs Inscribed with a FS Laser PbP Technique

In this chapter, we present the experimental characterization as well as qualitative analysis of the off-axis FBGs. Nine samples of off-axis FBGs are fabricated including one on-axis FBG as a reference. Before reporting the results, we first list in Table 3.1 some frequently-used acronyms in this chapter.

Table 3.1: Descriptions of the Acronyms Frequently Used in Chapter 3

Acronym	Description
DoLP-L	Direction of the linear polarization of the incident wave is parallel to the spatial long axis of the ellipsoidal damage points
DoLP-S	Direction of the linear polarization of the incident wave is parallel to the spatial short axis of the ellipsoidal damage points
H-FBGs	The type of off-axis FBGs with horizontal offset
V-FBGs	The type of off-axis FBGs with vertical offset
RIM	Refractive index modulation

3.1 Introduction

Fiber Bragg gratings (FBGs) inscribed by focused infrared femtosecond (FS) irradiation are of great interest in optical sensing and fiber laser applications [6, 7, 8, 9, 10, 11, 12, 13, 14, 15, 16]. The unique properties of such gratings, compared to the conventional ultraviolet

(UV)-inscribed FBGs, stem from the physical mechanisms behind grating formation. For example, the underlying nonlinear absorption of the laser energy obviates the need of photosensitization [45] thus enabling grating inscription into almost all types of optical fibers [13, 46, 47, 48]. Further, the ultrashort pulse duration leads to highly localized refractive index modulation (RIM) as a result of a-few-femtosecond-long transfer of energy from the laser pulses to the electrons [49], as well as the fact that the multi-photon process occurs most likely only within the focal volume of the FS pulses as it require a high density of photons in order to have multiple photons hitting a single electron at the same time. Currently, the most commonly used methods of FBG inscription via FS laser include point-by-point (PbP) [41], line-by-line [50], and phase mask scanning [51] techniques. Among them, PbP inscription takes an added advantage through providing full position control over each grating pitch.

To date, FBGs inscribed by FS laser PbP technology have been extensively studied for optical sensing. For instance, in [6, 7, 8], off-axis FBGs written in single-mode fibers (SMFs) have been employed for bending sensing. The FBGs in SMFs, limited by their single resonant wavelength, are usually incapable to sense multiple parameters simultaneously. In fact, such capability is often desirable, particularly in the situation where multiple parameters are coexisted and coupled. To overcome this limitation, few-mode fibers (FMFs) and multimode fibers (MMFs) instead can be used to inscribe the Bragg gratings into. Most of the recent designs of FBGs in FMF/MMFs written by FS lasers for sensing purpose, however, are limited to phase mask scanning method [9, 10, 11]. The utilization of phase mask reduces the inscription flexibility inherent of PbP technique. Furthermore, owing to the chaotic multimode nature in practice, MM-FBGs suffer severer signal degradation than FM-FBGs [25] and hence require more sophisticated interrogation techniques. Consequently, FM-FBGs fabriacted by FS PbP technique are of our particular interest for optical sensing. It therefore

necessitates a precise study of such FBGs. FM-FBGs fabricated with phase mask scanning technique have been studied in [11, 52, 53, 54]. The employment of the phase mask, however, leads to different grating morphology and thus grating properties compared to the FBGs fabricated by PbP technique. Moreover, the polarization dependence were not considered in the aforementioned work.

In this Chapter, we present detailed design and experimental characterizations of the FBGs inscribed into a step-index two-mode fiber (TMF) with a FS laser PbP technique, with multiple characteristics reported for the first time as far as we are concerned. The grating samples are designed to have varied horizontal and vertical offset distances from the fiber center. Take into consideration the elliptical shape of the RIM induced by FS pulses [55, 56], we first determine the spatial orientation (i.e., the long and short axes of the RIM) of each FBG sample via the polar plots of the scattering patterns generated by the visible light propagating in the fiber with FBG inscribed. By means of polarization control of the incident wave and image acquisition of the grating-reflected optical signals, we study the dependence of the transmission and reflection spectra on the offset position and the direction of linear polarization (DoLP) of the incident continuous laser beam. We note here that the results below are presented on the linearly-polarized (LP) mode basis, but with additional consideration of the two-fold degeneracy of the LP_{01} regarding the polarization and the four-fold degeneracy of the LP_{11} (two related to the polarization, two linked to the spatial distribution), as a balance of the LP mode approximation and the true eigenmodes (hybrid vector eigenmodes) [19]. To highlight, we report the birefringence induced by the FS pulses is offset-dependent. We also find that the reflection of the LP_{11} exhibits strong capability of polarization discrimination, and it differs in the horizontal and vertical off-axis FBGs. Moreover, we report that the forward LP_{01} couples backwardly to the LP_{11} with strong preference to only one of the two degenerate spatial distribution of the LP_{11}, and this

can be solely controlled by the DoLP of the incident light.

3.2 Design and fabrication of the off-axis TM-FBGs

3.2.1 FBG design

The schematic of the off-axis TM-FBGs is shown in Fig. 3.1, where the FS pulses, the core, and the cladding are out of scale for a better illustration. To be concise, both the vertical and horizontal off-axis FBGs are shown in the schematic. All damage points are lying on a straight line parallel to the fiber axis for one off-axis FBG sample. In particular, the damage points of H-FBGs are in the plane perpendicular to the direction of the FS pulses, whereas the V-FBGs in the plane containing the pulse direction. We fabricated eight off-axis FBGs in total, namely, H/V-2, H/V-4, H/V-6, and H/V-8, as well as an on-axis FBG (H/V-0). The numbers behind the "H" or "V" represent the distance between the damage-point-line to the fiber axis in the unit of micrometer; the fiber radius is 9.5 µm. All FBGs are 5 mm long, with grating pitch $\Lambda = 1.076$ µm.

The grating pitch and the Bragg wavelength are related by phase-matching condition of two counter-propagating modes, the k- and the n-th modes:

$$\beta_k + \beta_n = m\frac{2\pi}{\Lambda_m}, \tag{3.1a}$$

$$\lambda_{kn} = \frac{\Lambda_m}{m\big(n_{\mathrm{eff},k} + n_{\mathrm{eff},n}\big)}, \tag{3.1b}$$

where k and n can either be the same or different, m denotes the order of the FBG as designed, and Λ_m represents the physical grating pitch inscribed regardless of the value of m. For example, in Fig. 3.2, we show all the possible Bragg wavelengths of a typical step-

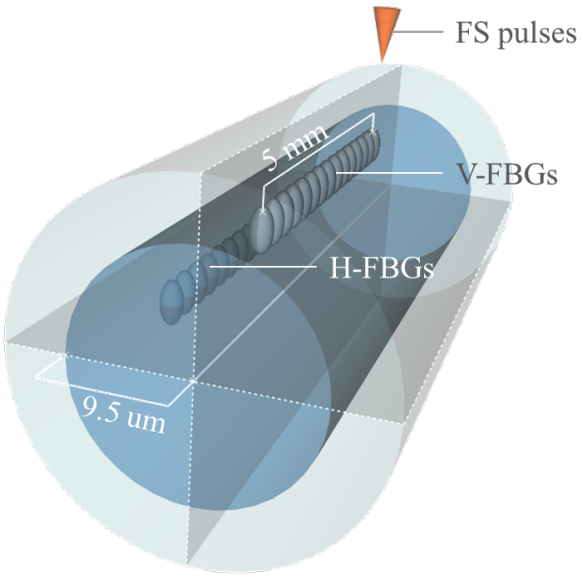

Figure 3.1: Out-of-scale schematic of the off-axis TM-FBGs, both the horizontal and vertical samples are displayed.

index four-mode fiber. Here, β_G signifies the equivalent propagation constant of the m-th order FBG; Bragg wavelengths marked at the bottom are corresponding to the self-coupling of the associated LP modes, whereas the Bragg wavelengths at the top are for the cross-coupling between two LP modes. The relationship between β and λ can be numerically obtained by solving an eigenvalue equation derived from Maxwell's equations and proper boundary conditions. One can refer to the chapter of "Fiber Optics" of [57] for more detail of the numerical implementation.

3.2.2 FBG fabrication

The microscope image of the cross-sectional area of the step-index TMF after one-minute reaction with hydrofluoric acid is displayed in Fig. 3.3. This TMF is then mounted onto the air-bearing stage depicted in Fig. 2.15, the stage is translated along the direction of the fiber axis in this case to inscribe straight lines parallel to the fiber axis. The translation speed is

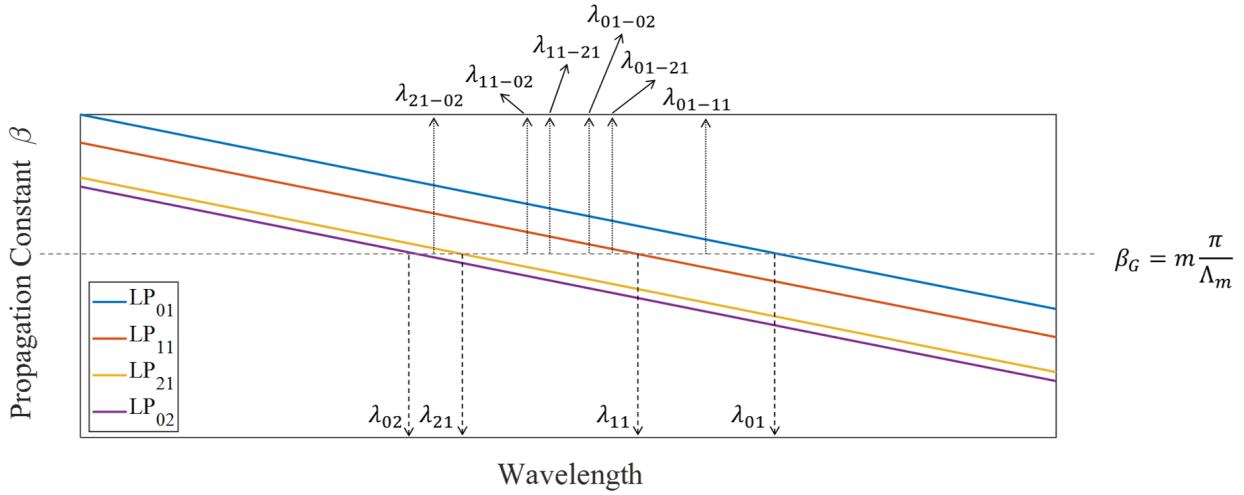

Figure 3.2: Plot of propagation constant against wavelength for a typical step-index four-mode fiber. λ_{kn}: All the possible Bragg wavelengths for an m-th order FBG with grating pitch Λ_m.

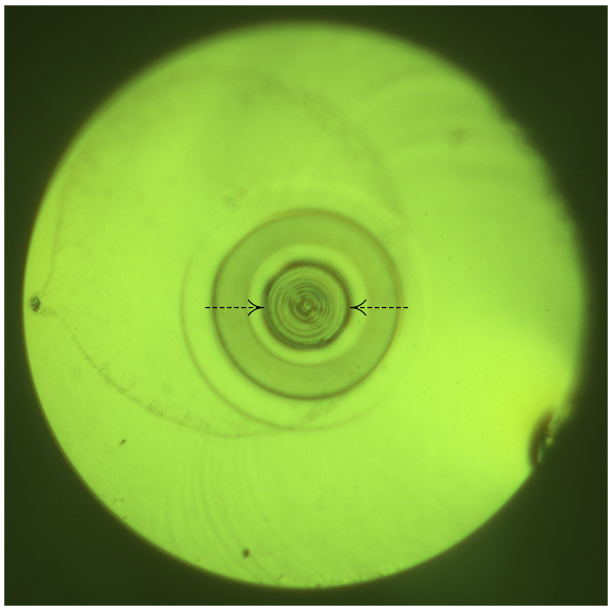

Figure 3.3: Microscope image of the cross-section of the TMF used after immersed into hydrofluoric acid solution for 1 minute. Arrows indicate the core region.

determined using (2.12). The precision of the grating pitch inscribed is later estimated by measuring the Bragg wavelength of the LP_{01} for all nine samples; the standard deviation is measured as 0.09 nm, which is likely caused by the random axial strain along the fiber when manually loaded onto the clamps shown in Fig. 2.15. In Fig. 3.4, we display representative

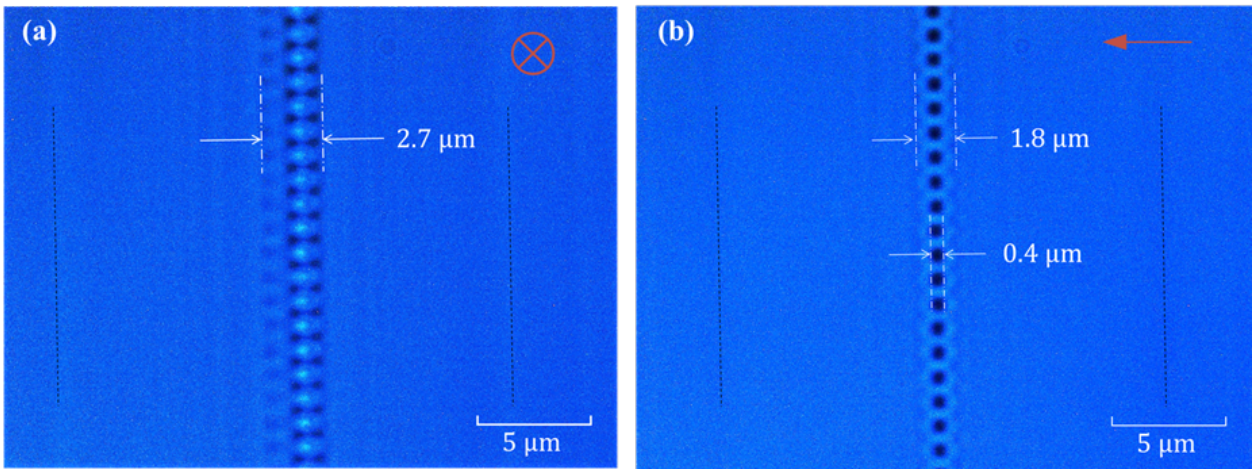

Figure 3.4: Microscope images of the (a) top-view and (b) side-view of sample V-2 (off-axis FBG with 2 µm vertical offset)

top-view and side-view of a short section of the laser-induced periodic structure of sample V-2 (off-axis FBG with 2 µm vertical offset). We mark the core-cladding interface with black dashed lines, indicate the propagation direction of the FS pulses with red arrows, and annotate the features sizes of the periodic structure in white. As can be seen in Fig. 3.4, albeit limited to image resolution, the laser-induced structural change takes the shape of ellipsoid with a center micro-void plus an outer densified shell surrounded; the spatial long axis of the ellipsoid is parallel to the direction of the FS pulses [55]. We also notice that there is additional RIM at the bottom of each damage point as shown in Fig. 3.4(b), this is likely resulted from the spherical aberration at the interface between the objective and the index-matching oil, since we deliberately match the index of the oil to the index of fiber (~ 1.45) instead of the index suggested for the objective lens (~ 1.5) [43]. Additionally, we show the top-views of all the remaining off-axis FBGs to give the readers a rough idea on

the inscription stability.

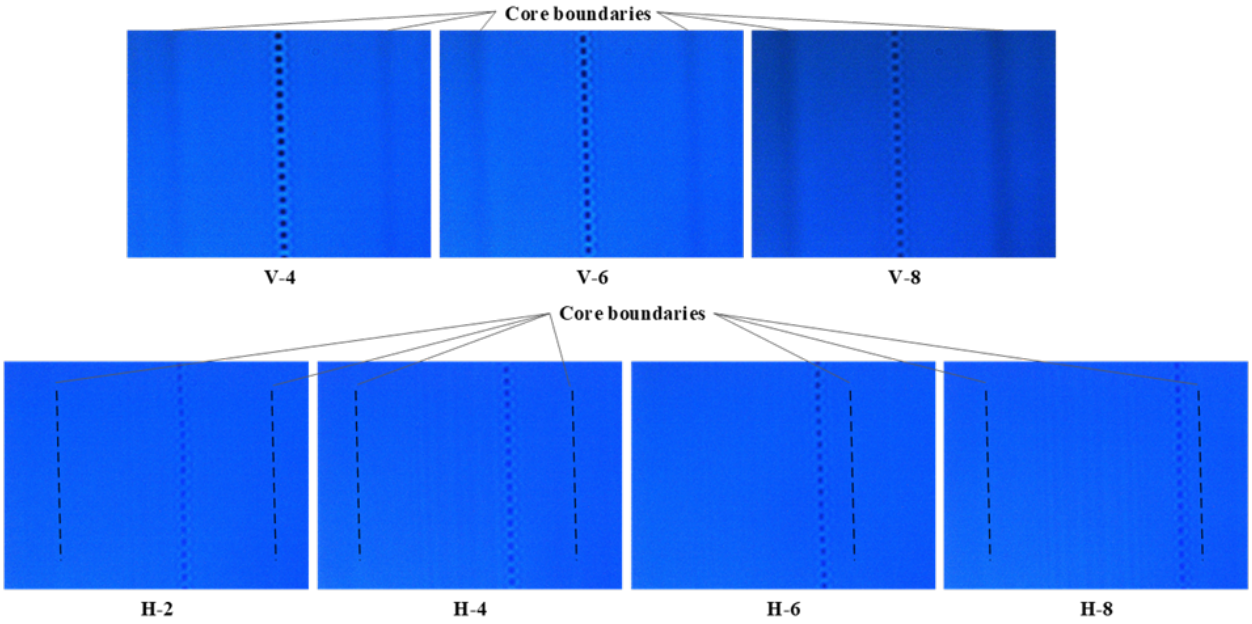

Figure 3.5: Microscope images of the top-views all remaining off-axis FBGs.

Besides, here we give a rough comparison between the feature size of the damage point and the focal volume of the focused Gaussian beam pulse chain. A Gaussian beam (beam waist $w = 3$ mm, refer to 2.2.1) after focusing by a 100× objective lens and a 200 mm tube lens, the resulting beam waist (w_0) and Rayleigh range (z_R) are calculated as

$$w_0 = \frac{\lambda f}{n\pi w} \tag{3.2a}$$

$$z_R = \frac{\pi w_0^2 n}{\lambda}, \tag{3.2b}$$

where $\lambda = 800$nm is center wavelength of the FS laser, f is determined by the tube length divided by the magnification ($f = 200/100$mm $= 2$ mm), and n is the refractive index of the oil (1.446). Taking these numbers into Eq. (3.2) yields $w_0 = 0.1151$ µm and $z_R = 0.0774$ µm. The magnitude of $2w_0$ and $2z_R$ are comparable to the measured size of the central void

(0.4 µm × 0.4 µm).

3.3 Spatial orientation of the damage points

The presence of the off-axis ellipsoidal damage points (refer to Fig. 3.4) breaks the axial symmetry of the pristine fiber and hence may induce birefringence. To fully characterize the spectral properties of the grating samples, we firstly identify the spatial orientation (i.e., the long or short axis) of the damage points with the setup depicted in Fig. 3.6(a). In this setup, a laser light operating at 660 nm is coupled into the the fiber which is kept as straight as possible, the scattered laser light off the damage points is recorded in a plane perpendicular to the fiber axis. There are two straight lines at right angle marked in the plane, one of the two is parallel to the optical table. The recorded scattering patterns of varied grating samples are presented in Figs. 3.6(b)–3.6(i). As can be seen, there are two bright regions separated by $\sim 180°$ in the ring-like scattering patterns, connected by dashed white lines. The arrow pairs in white indicate the distance between the origin and the dashed white lines. It is of our particular interest that the dashed white lines almost pass through the origin for H-FBGs as shown in Figs. 3.6(c)–3.6(e), while there are gaps between the lines and the origin in the case of V-FBGs as presented in Figs. 3.6(f)–3.6(i). Moreover, the length of such gap increases with an increasing vertical offset distance, as we expected. The FBG orientation can hence be characterized that the spatial long axis of the ellipsoidal damage points is perpendicular to the dashed white lines, as pictured in Fig. 3.6(i), where a white circle surrounded by a blue ellipse shell represent the damage point. In principle, one can relate the orientation of the damage points to their scattering patterns through the scattering theory of spheroidal particles as outlined in [58]. In this specific case, the TMF at 660 nm can support 17 LP modes, a random mixture of these LP modes can be

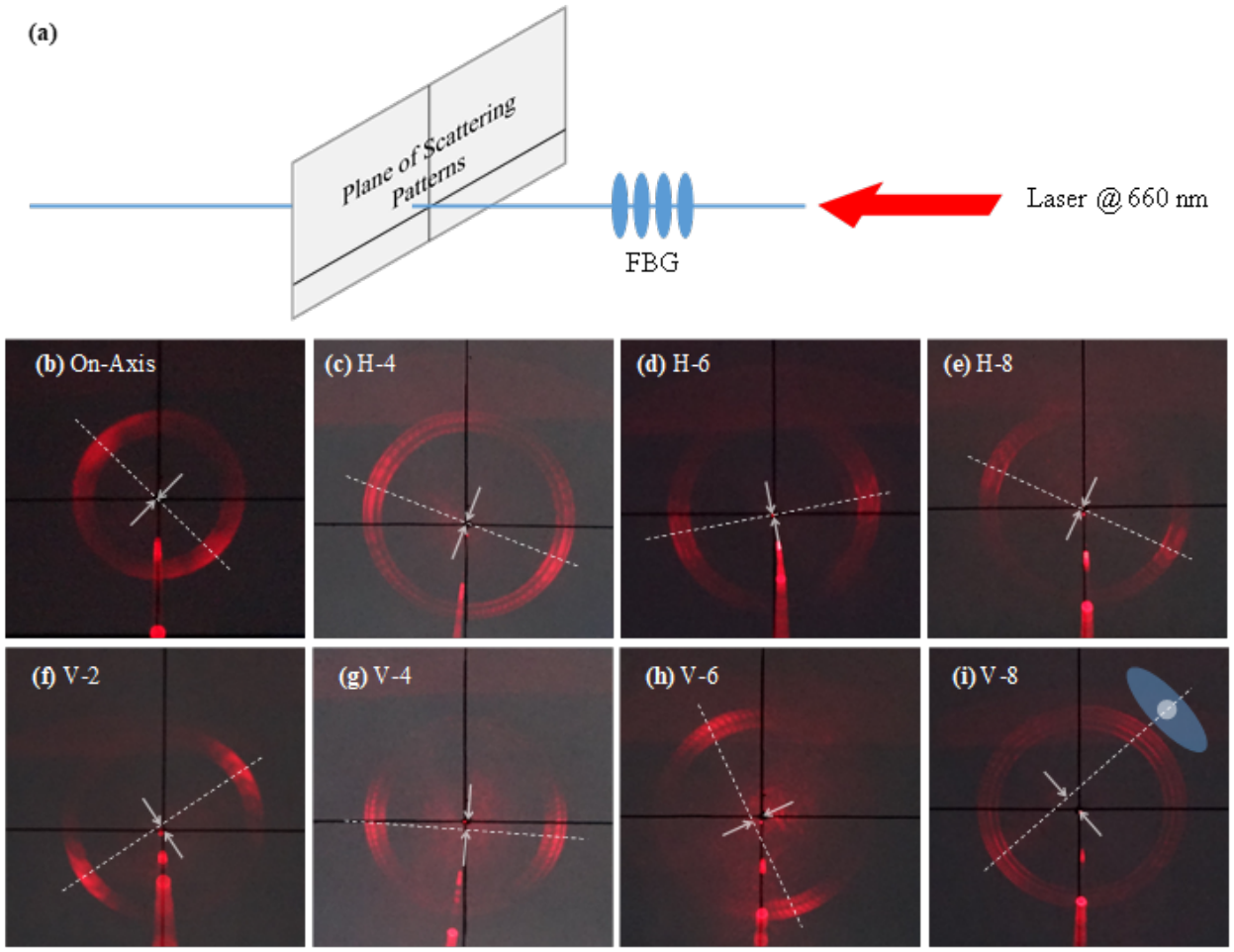

Figure 3.6: (a) Schematic of the experimental setup to identify the FBG orientation. (b)–(i) Scattering patterns of the grating samples recorded on the plane perpendicular to the fiber axis. The compound of a white circle and a blue ellipse in (i) represents the identified orientation of the damage points.

regarded as almost-equally-excited transverse magnetic and transverse electric modes. The application of the conclusion of a similar situation in [58] to our case leads to the fact that is consistent with our previous observation, i.e., the dashed white lines are perpendicular, instead of being parallel, to the spatial long axis of the damage points. Moreover, similar scattering patterns were reported for FS-inscribed filament-array gratings in an SMF [59] and also for FS-PbP-inscribed FBGs in a large mode area double clad fiber [60].

3.4 Characterization Results

Figure 3.7 shows the experimental setup used for characterization of the grating samples. A tunable laser (New Focus, TLB-6728) emits continuous wave at a desired wavelength λ

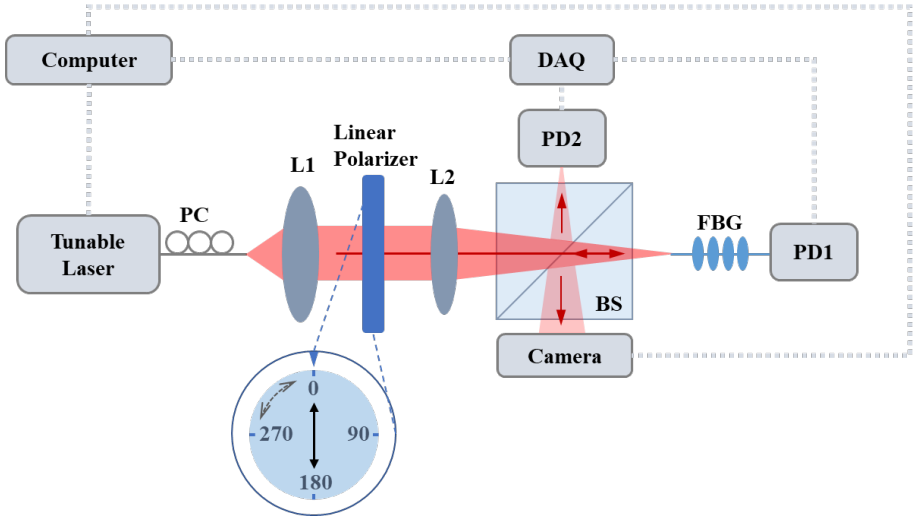

Figure 3.7: Schematic of the experimental setup used to characterize the off-axis TM-FBGs. PC: polarization controller; L1: collimator; L2: focusing lens; BS: beam splitter; PD1/PD2: photodiode; DAQ: data acquisition. Inset depicts the linear polarizer (polarization direction marked by the arrow) observed from the L1 side.

with narrow-linewidth. Then the laser beam is collimated in free-space by L1 after being modulated by a fiber-based polarization controller (PC). The polarization of the collimated beam is further tuned by a linear polarizer, details of which are depicted in the inset where

the direction of polarization is marked by the double-headed arrow. Afterwards, the beam is focused by L2 into the TMF ($\sim$ 1 m) in which an FBG is inscribed at $\sim$ 20 cm away from the output end. Again the fiber is kept as straight as possible to reduce the intermodal coupling; moreover, the output end is also immersed into index-matching liquid to mitigate Fresnel reflection at the interface between silica and air, and the transmitted signal is detected by a photodiode (PD1). Prior to launching onto the fiber core, nearly half of the focused beam is reflected off the non-polarizing beam splitter (BS) to another photodiode (PD2), which is used to compensate laser power fluctuation during wavelength scanning. Signals from the two PDs are acquired by a data acquisition (DAQ) card (National Instruments, NI USB-6211) and sent to a computer for data processing. It should be noted that the BS is deliberately tilted to separate the relatively weak optical signals reflected off the grating from the multiple reflections of the focused beam by the BS cube surfaces. In the meantime, an infrared camera (Goldeye, G-032) is used to capture the intensity profile of the optical light reflected by the grating, deflected by the same BS. The optical power can accordingly be calculated via taking a sum over all camera pixels. With PD2, we define a normalized transmitted signal $\mathbb{T}_\lambda$ and reflected signal $\mathbb{R}_\lambda$ at wavelength λ in arbitrary unit, respectively as

$$\mathbb{T}_\lambda = \frac{P_{1,\lambda}}{P_{2,\lambda}} \tag{3.3a}$$

$$\mathbb{R}_\lambda = \frac{\sum_{\text{all }(x,y)} P_{\text{cam},\lambda}(x,y)}{P_{2,\lambda}}, \tag{3.3b}$$

with P denoting the optical power. As a result, through wavelength scanning with the tunable laser, one can obtain the transmission spectra and reflection spectra in a relative manner. The scanning rate we used is 0.02 nm/s. Besides, for signal denoising purpose, we additionally average the data acquired by the PDs and camera at each wavelength. We note that since the readout mechanisms of the camera and PDs are different, $\mathbb{R}$ can only

reveal the reflectivity, but this is acceptable to us as the comparison of the subjects is of our particular interest.

3.4.1 Spectra

Three representative reflection spectra of sample on-axis (with no offset), H-4 (with intermediate offset), and V-8 (with large offset) are shown in Fig. 3.8. Both the two orthogonal directions of linear polarization are tested and presented in different colors (DoLP-L in blue, DoLP-S in red). The transmission spectra (upper, $\sim$.1) and the relative reflection spectra (lower, $\sim$.2) are both presented in linear scale; the dotted trace denotes the measured data after normalization, and the solid curve represents the Gaussian fitting [61]. In particularly, we normalize the transmission spectra to the total coupled-in power $\mathbb{T}_0$ through $\mathbb{T}/\mathbb{T}_0$, and the relative reflection spectra by the background reflection $\mathbb{R}_0$ and the total coupled-in power $\mathbb{T}_0$ via $(\mathbb{R} - \mathbb{R}_0)/\mathbb{T}_0$. Moreover, we characterize $\mathbb{R}_0$ and $\mathbb{T}_0$ at wavelengths longer than the Bragg wavelength of the LP_{01} for each of the trace. Additionally, in Fig. 3.8(b.2) as an example, we mark the reflection peaks as P1, P2, P3, and P4. We will discuss the relative intensities of these peaks in a later section. It can be seen that in Figs. 3.8(b.1) and 3.8(c.1), we fit the P3 by sum of two Gaussian. A later characterization will reveal that P3 actually includes two secondary peaks that are closely positioned. Specifically, one is formed by the self-coupling of the LP_{11} and the other one by cross-coupling of the LP_{01} and LP_{21} (refer to Fig. 3.2). The existence of the LP_{21} is likely due to the short length of the TMF which has a relatively large V-number ($\sim$ 4.6). Similar excitation of the LP_{21} has also been reported with UV-inscribed TM-FBGs [54]. Nevertheless, this may have little effect for our case, since the two secondary peaks are clearly separated. In addition to P3, P2 is formed by the cross-coupling of the LP_{01} and LP_{11} ($LP_{01\leftrightarrow 11}$), and P1 by the self-coupling of the LP_{01}. Besides, the cross-coupling of the LP_{11} and LP_{21} results in P4. Therefore, for a TM-FBG with

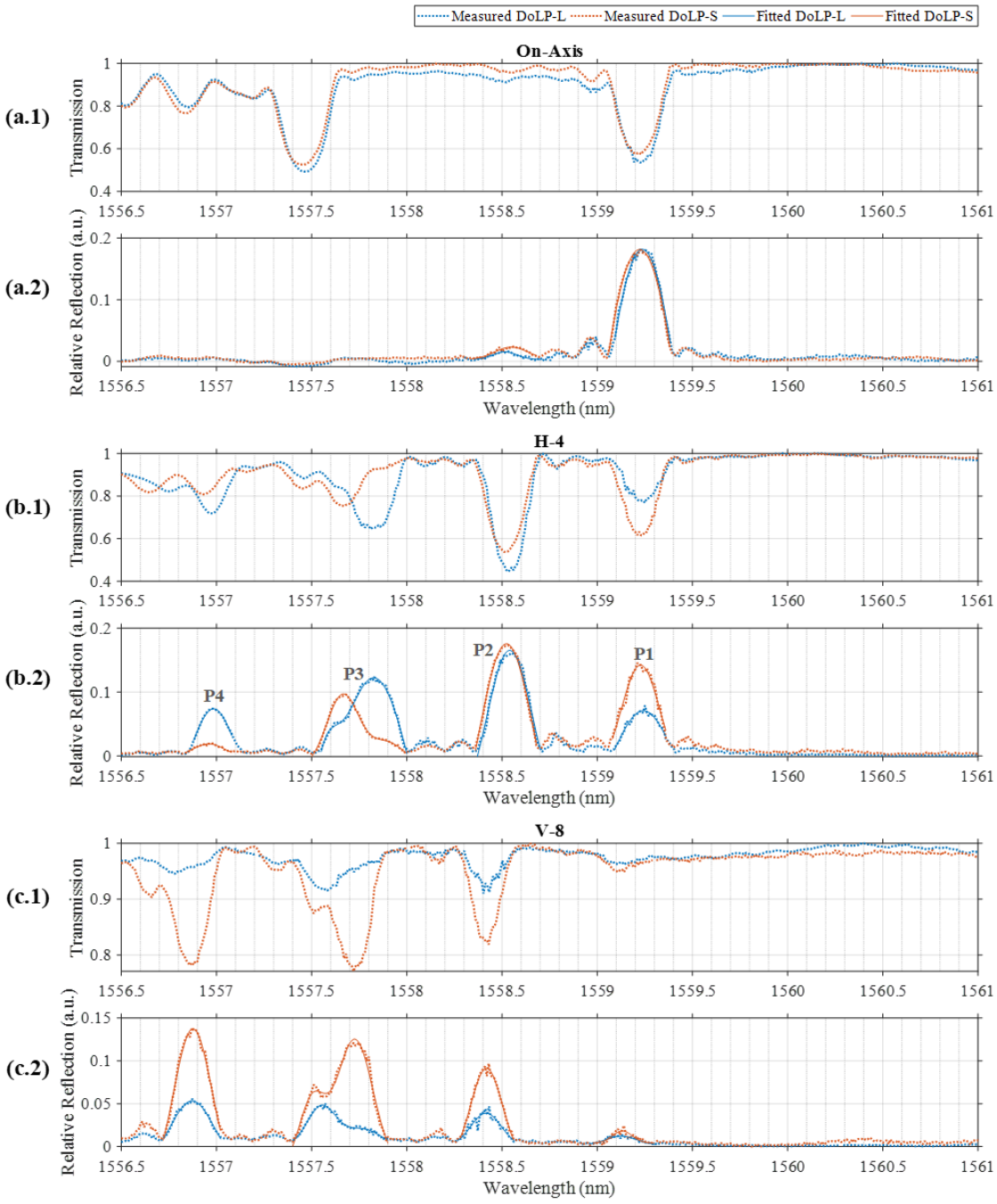

Figure 3.8: Transmission (upper, ∼.1) and reflection spectra (lower, ∼.2) of (a) on-axis, (b) H-4, and (c) V-8. Blue: DoLP-L; red: DoLP-S; dotted: measured data; solid: Gaussian fitting.

moderately long fiber length, the Bragg wavelengths can still be identified using Eq. (3.1b), in particular:

$$\lambda_{01} = \frac{2n_{\text{eff},01}}{m}\Lambda, \tag{3.4a}$$

$$\lambda_{01\leftrightarrow 11} = \frac{n_{\text{eff},01} + n_{\text{eff},11}}{m}\Lambda, \tag{3.4b}$$

$$\lambda_{11} = \frac{2n_{\text{eff},11}}{m}\Lambda, \tag{3.4c}$$

where $m = 2$ is the order of our FBG samples. We note that due to the limited frame rate of the camera (25 Hz), there are random but minor fluctuations along the traces in Fig. 3.8. Furthermore, the coupling of the forward-propagating core modes to the backward-propagating cladding modes leads to the additional dips at shorter wavelengths in the transmission spectra. The reflection spectra of the rest off-axis FBG samples are shown in Figs. 3.9 and 3.10, which are obained with Eq. (3.3b) without further normalization to $\mathbb{R}_0$ and $\mathbb{T}_0$.

3.4.2 Offset-dependent birefringence

The axial symmetry of the pristine fiber is broken by the laser-induced RIM, as a result of the ellipsoidal shape and the off-axis position of the RIM, birefringence is therefore induced. We present in this section that the induced birefringence exhibits dependence on the offset position of the RIM, such dependence is characterized as follows. In principle, the LP_{11} has four-fold degeneracy, two regarding polarization and two about spatial distribution; the LP_{01}, in contrast, possesses two-fold degeneracy concerning only the polarization [22]. Therefore the LP_{01} is utilized for our purpose of birefrigence characterization to avoid ambiguity. In particular, we characterize the birefringence from the difference of the two Bragg wavelengths of the LP_{01} under the two orthogonal directions of linear polarization (DoLP-L, DpLP-S).

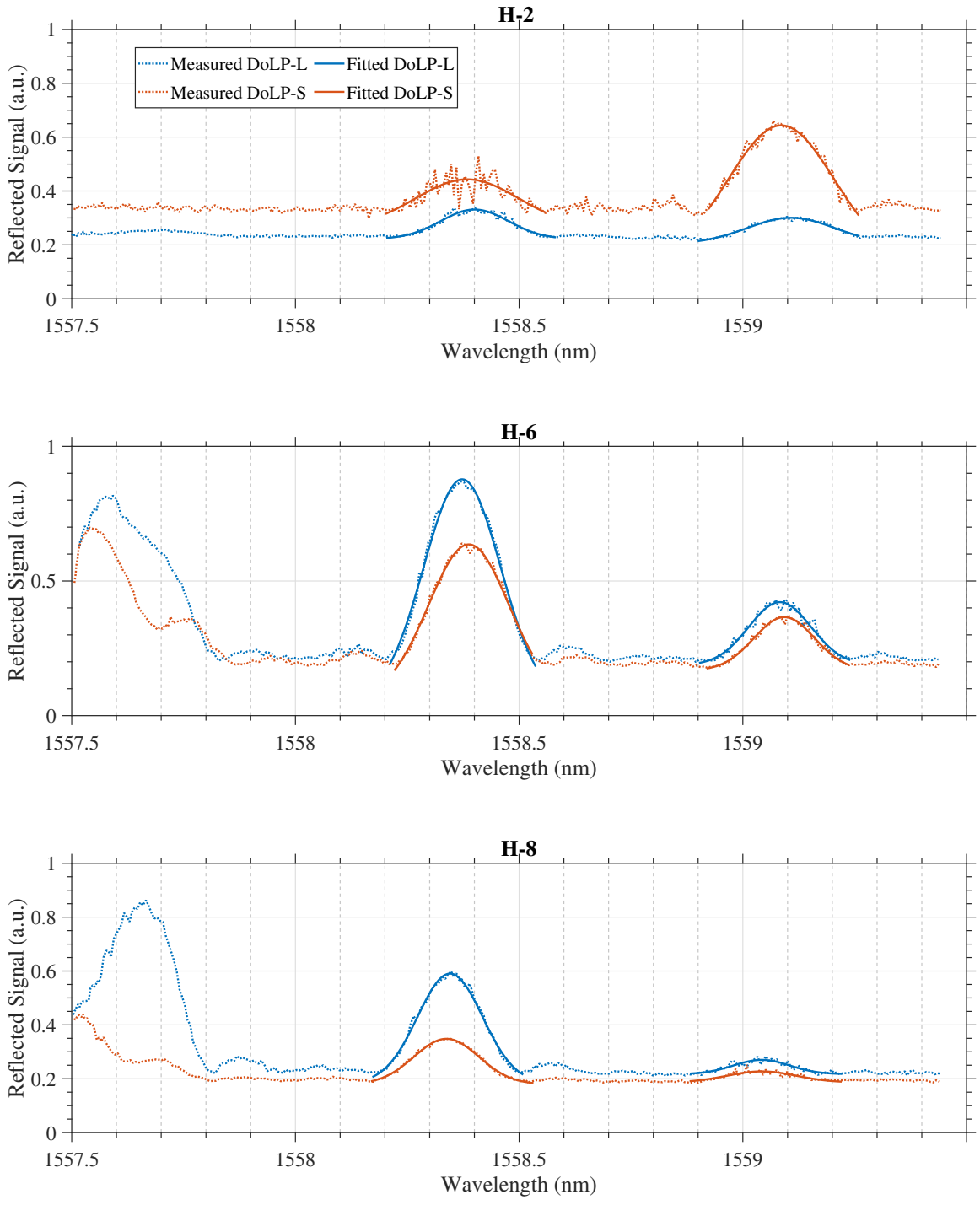

Figure 3.9: Reflection spectra (obtained with Eq. (3.3b) only, no characterization of $\mathbb{T}_0$ and $\mathbb{R}_0$) of all remaining H-FBGs.

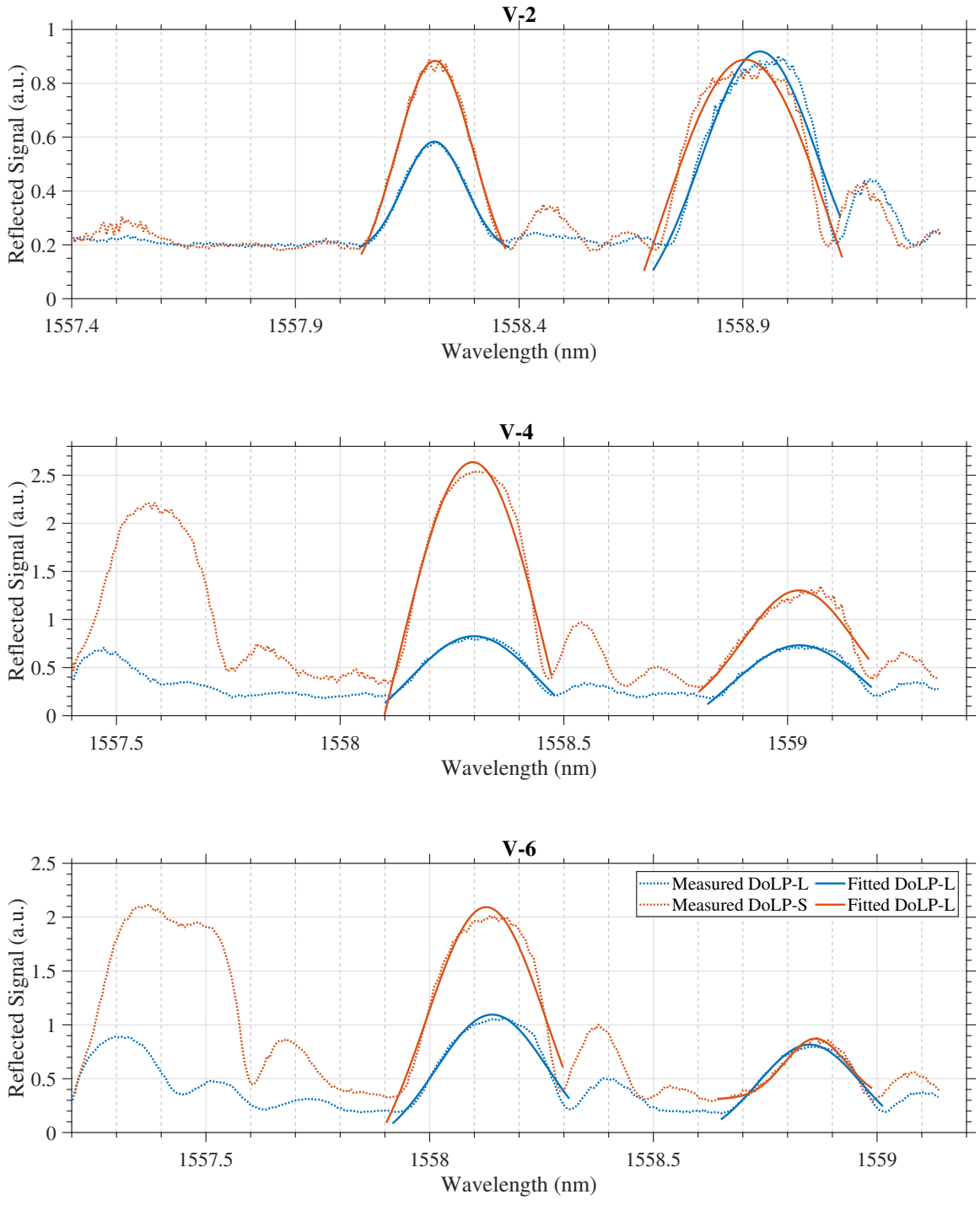

Figure 3.10: Reflection spectra (obtained with Eq. (3.3b) only, no characterization of $\mathbb{T}_0$ and $\mathbb{R}_0$) of all remaining V-FBGs.

The birefringence can therefore be defined as

$$\Delta n_B = n^L_{\text{eff},01} - n^S_{\text{eff},01} = (\lambda^L_{01} - \lambda^S_{01})\frac{m}{2\Lambda}, \tag{3.5}$$

where $m = 2$ is the order of the FBG fabricated, λ^L_{01} and λ^S_{01} are identified from the Gaussian fittings of the LP_{01} (refer to Figs. 3.8, 3.9, and 3.10). The characterized birefringence is summarized in Fig. 3.11, H-FBGs and V-FBGs are presented by different colors. In particular the on-axis sample is ploted twice as both H-0 and V-0. In general, the birefringence reaches

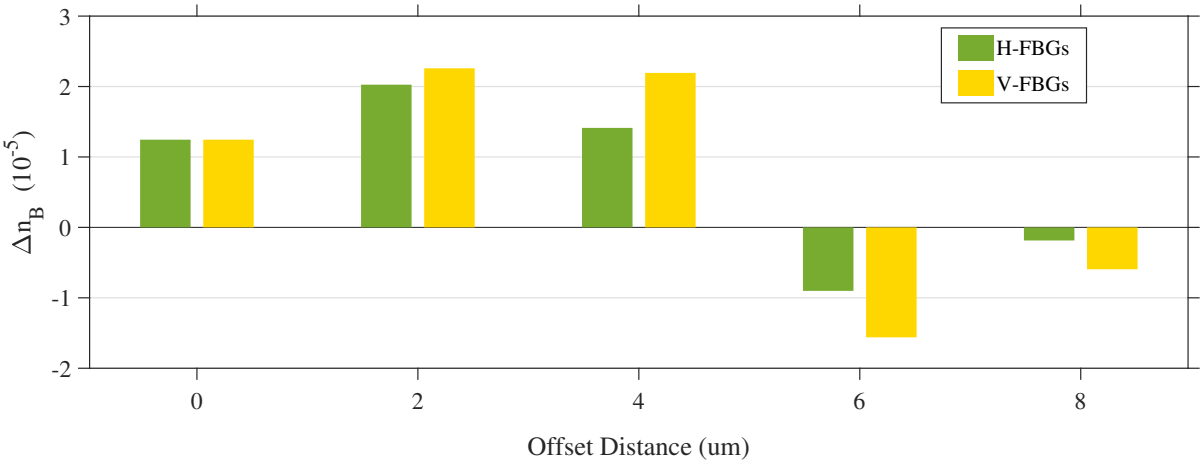

Figure 3.11: Induced birefringence of H-FBGs (green) and V-FBGs (yellow).

its maximum magnitude at an intermediate offset distance, in the meantime, the V-FBGs have stronger birefringence than their horizontal counterparts H-FBGs with the same offset. The observations are in consistence with the off-axis FBGs in standard SMF reported in [62]. It is particularly worth noting that Δn_B changes its sign between offset 4 µm and 6 µm. Although the physical mechanisms behind this phenomenon remains unclear, here we suggest two possible directions for future investigation. Firstly, one may need to consider modal structure of the pristine fiber has been altered by the strong RIM induced by FS pulses. Furthermore, one may also take into consideration the tensor nature of laser induced

material perturbation.

3.4.3 Offset- and polarization-dependent reflectivity

We next study the reflectivity in a relative manner of the individual LP mode (i.e., LP_{01}, LP_{11}, and $LP_{01\leftrightarrow 11}$) for all the FBG samples. Typically, the reflectivity characterization of each individual LP mode in an FMF requires selective mode excitation. To do so, we maximize the normalized reflected signal $\mathbb{R}$ (see Eq. (3.3b)) via manually fine-tuning the position of the fiber proximal end at the corresponding Bragg wavelength of a certain LP mode (e.g., λ_{01}^{L} for the LP_{01} under DoLP-L). Thus the reflectivity of the corresponding LP mode is equivalent to the maximized $\mathbb{R}_{\max}$ with the background reflection $\mathbb{R}_0$ subtracted; $\mathbb{R}_0$ is characterized at longer wavelength after maximizing $\mathbb{R}$ for each reflectivity measurement. Both of the two orthogonal directions of linear polarization (DoLP-L, DoLP-S) are measured, the results are presented in Figs. 3.12(a) and 3.12(b). Distinct patterns represent different LP modes; colors denote the two orthogonal directions of linear polarization, DoLP-L in blue and DoLP-S in red' error bars quantifies the uncertainty mainly from the manual fine-tuning, measured from three independent trials. It is evident that the reflectivity shows dependence on both the offset distance and polarization of the incident beam, as observed from Fig. 3.12.

Offset dependence

We first analyze the offset dependence. In principle, under the approximation of weak perturbation, the coupling coefficient (K_{kn}) between the k-th and n-th modes caused by a perturbation to the permittivity $\Delta\varepsilon(x, y)$ can be expressed as [19]

$$K_{kn} = \frac{\omega}{4} \iint \mathbf{e}_k^* \cdot \Delta\varepsilon(x, y)\mathbf{e}_n \, dx \, dy. \tag{3.6}$$

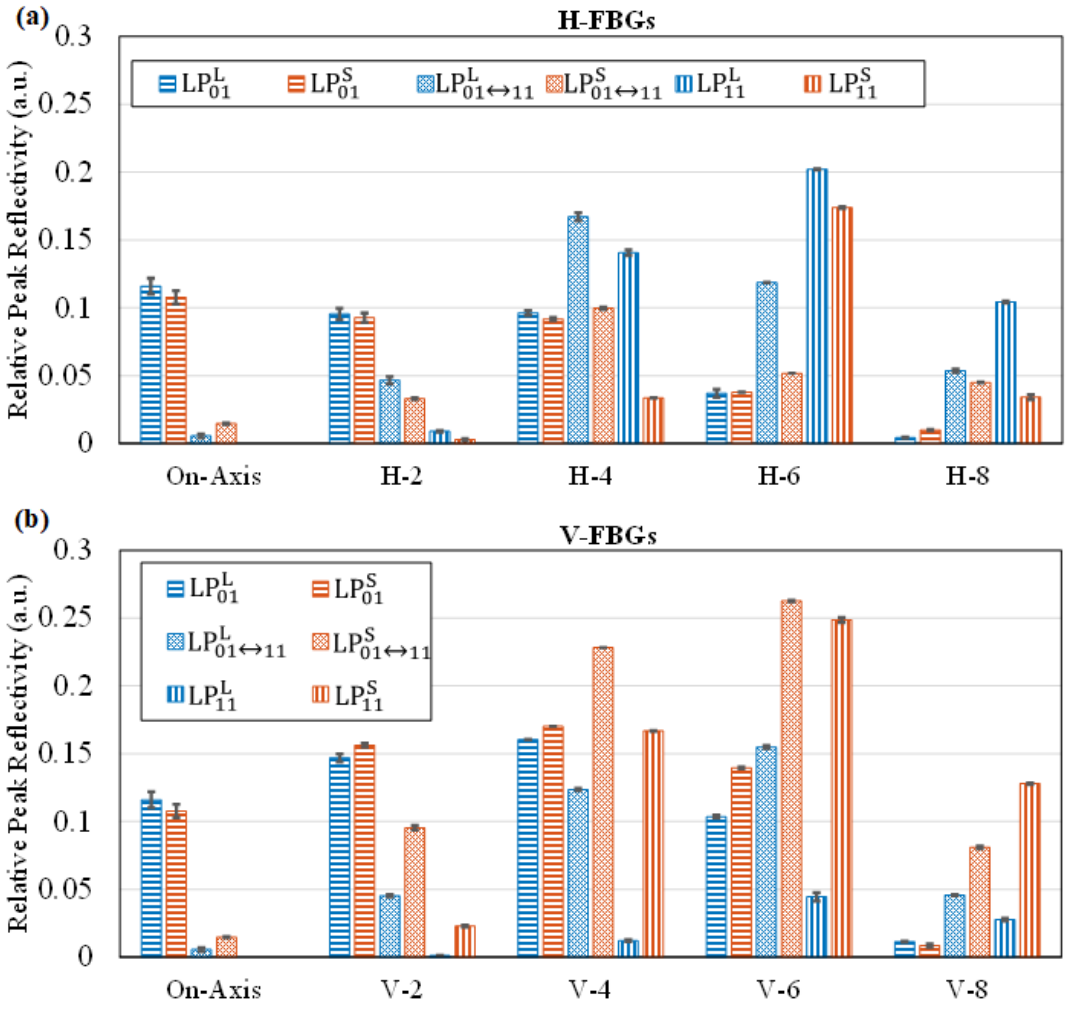

Figure 3.12: Reflectivity with error bars of (a) H-FBGs and (b) V-FBGs. LP modes are represented with distinct bar patterns; blue: DoLP-L; red: DoLP-S.

This expression basically describes the transverse overlap between the damage points and the modes under investigated, which can reveal the strength of reflection. The transverse overlap is visualized in Fig. 3.13, where the LP_{01}, and the two spatial degenerate LP_{11a} and LP_{11b} are considered without loss of generality. For better comparison, we plot together the V-FBGs (yellow) and H-FBGs (green) with the same offset distance, and mark the core-cladding interface by the dashed while circles. Furthermore, the size of the damage points is based on the measurement in Fig. 3.4. As can be seen here, the reflectivity of our Type-II FBGs

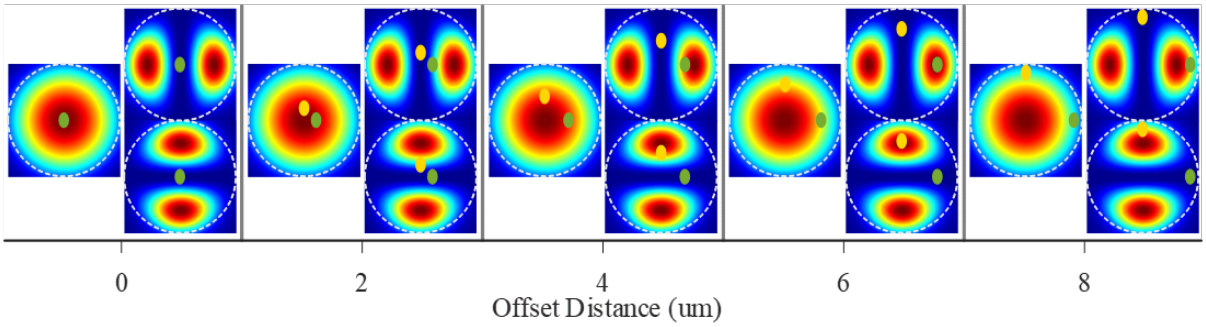

Figure 3.13: Visualization of the transverse overlap between the damage points (green for H-FBGs, yellow for V-FBGs) and the LP modes (LP_{01}, LP_{11a}, and LP_{11b})

can still be qualitatively revealed by Eq. (3.6) together with the LP modes of the pristine fiber, although the weak perturbation theory may not valid for Type-II FBGs quantitatively as suggested in [62]. In particular, the reflectivity of the LP_{01} of the H-FBGs monotonically decreases with offset increaing in general; the slightly increased reflectivity in V-FBGs at 2, 4, and 6 is likely due to the vertically elongated shape of the damage points as well as the combined effects of the void and desified shell. Similarly, the reflectivity of the LP_{11} starts with almost-zero at zero offset, then begins to rise until reaching it maximum at an intermediate offset distance, and then drops. This trend agrees with the doughnut-shaped LP_{11} intensity profile. Besides, $LP_{01\leftrightarrow 11}$ is also present in on-axis FBG, this is likely due to the asymmetric shape of the induced RIM. The reflectivity of the $LP_{01\leftrightarrow 11}$ has its maximum value at an intermediate offset distance.

Polarization dependence

In addition to the offset dependence, of more interest to us is the polarization dependence of the reflectivity, which reveals the capability of polarization discrimination. As presented in Fig. 3.12, the reflectivity of the LP_{01} is almost constant for DoLP-L and DoLP-S. In contrast, the reflectivity of the LP_{11} exhibits strong polarization dependence, we exact the reflectivity of the LP_{11} and display it in Fig. 3.14 As reported in [62], in SMF, the polarization

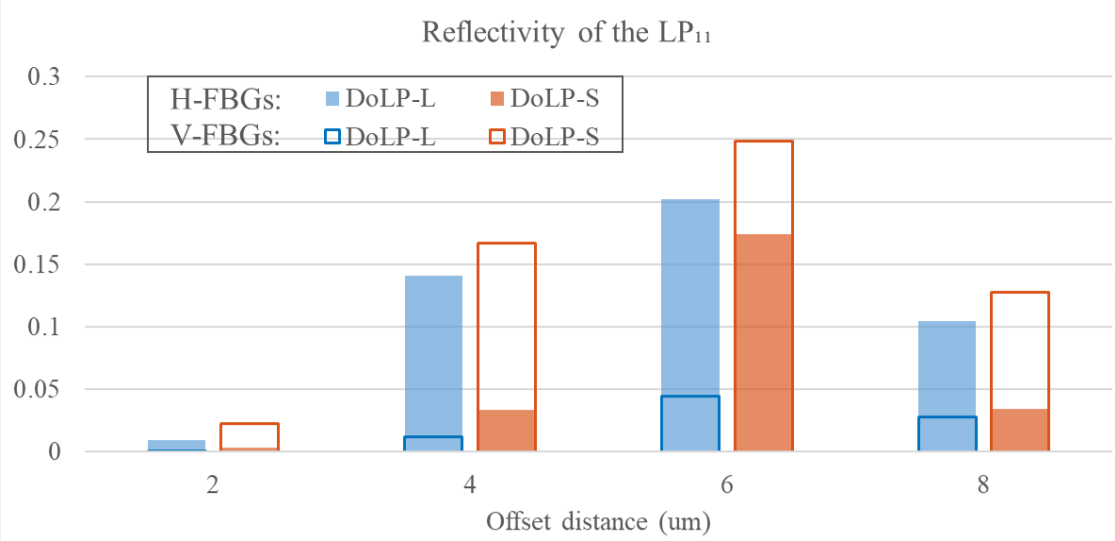

Figure 3.14: Reflectivity of the LP_{11}

discrimination capability is usually gained via using objectives with low NA to increase the eccentricity of the induced RIM. Interestingly, FM-FBGs can gain strong such capability even with tightly-focused FS irradiations, and one can accordingly expect further increased polariztaion discrimination of the FM-FBGs fabricated by loosely-focused FS irradiation. This observation also is self-consistent with the almost-constant reflectivity of the LP_{01} modes in our FBG samples fabricated by tightly-focused FS irradiation. The averaged ratio of the two LP_{11} reflectivity under DoLP-L and DoLP-S of a single FBG is measured as 7.86 for our off-axis TM-FBGs, as compared to the 1.46 for the SMFs in [62]. Furthermore, the DoLP corresponding to the much stronger reflectivity of the LP_{11} differs in H-FBGs and V-

FBGs, the direction is constantly perpendicular to the line connecting the RIM and the fiber center. As for the $LP_{01\leftrightarrow 11}$, its reflectivity follows similar polarization dependence pattern as the LP_{11}, since the $LP_{01\leftrightarrow 11}$ is in fact formed by the cross-coupling of the LP_{01} and LP_{11}, its polarization property is consequently determined by both the the LP_{01} and LP_{11}.

To further investigate the polarization dependence, we measure the $\mathbb{R}_{\max}$ under varied DoLP by rotating the polarizer shown in the inset of Fig. 3.7. Without loss of generality, FBG samples with horizontal offset (H-4) and vertical offset (V-4) are tested, the representative results are shown in Fig. 3.15. The Bragg wavelength for each of the mode is chosen as one lying in between the two peak wavelengths of DoLP-L and DoLP-S. For example, λ_{01} is set as the middle point of λ_{01}^{S} and λ_{01}^{L}. In Fig. 3.15, the solid curves in different colors are the best numerical fittings of their corresponding measured data sets represented by distinctive markers. It is noticeable that the reflectivity of both LP_{01} and LP_{11} exhibits sinusoidal-like dependence on polarization based on the agreement between the measured and fitted data, though such dependence of LP11 modes is much heavier. It can be seen that the LP_{11} reaches its maximum reflectivity at $\theta_{\text{maxR}}^{11}$, and the minimum reflectivity at $\theta_{\text{minR}}^{11}$, which is $\sim 90^{\circ}$ apart from the $\theta_{\text{maxR}}^{11}$. As we expect, for sample H-4, $\theta_{\text{maxR}}^{11}$ corresponds to the polarization parallel to the long axis of the damage points, and $\theta_{\text{minR}}^{11}$ the short axis. In contrast, for sample V-4, the maximum reflectivity appears when the polarization is parallel to the short axis of the damage points, and minimum occurs when polarization is along the long axis of the damage points.

Unlike the LP_{11}, as shown in Fig. 3.16, the peak reflectvity of the LP_{01} has a constant behavior pattern of polarization dependence, regardless of the FBG sample and/or the FBG orientation (Ori1, Ori2). It is hence reasonable to infer that such a constant polarization dependence in Fig. 3.16 is likely caused by the other optical elements used in the characterization setup, particularly the cube beam splitter (Thorlabs BS015) in Fig. 3.7. In principle,

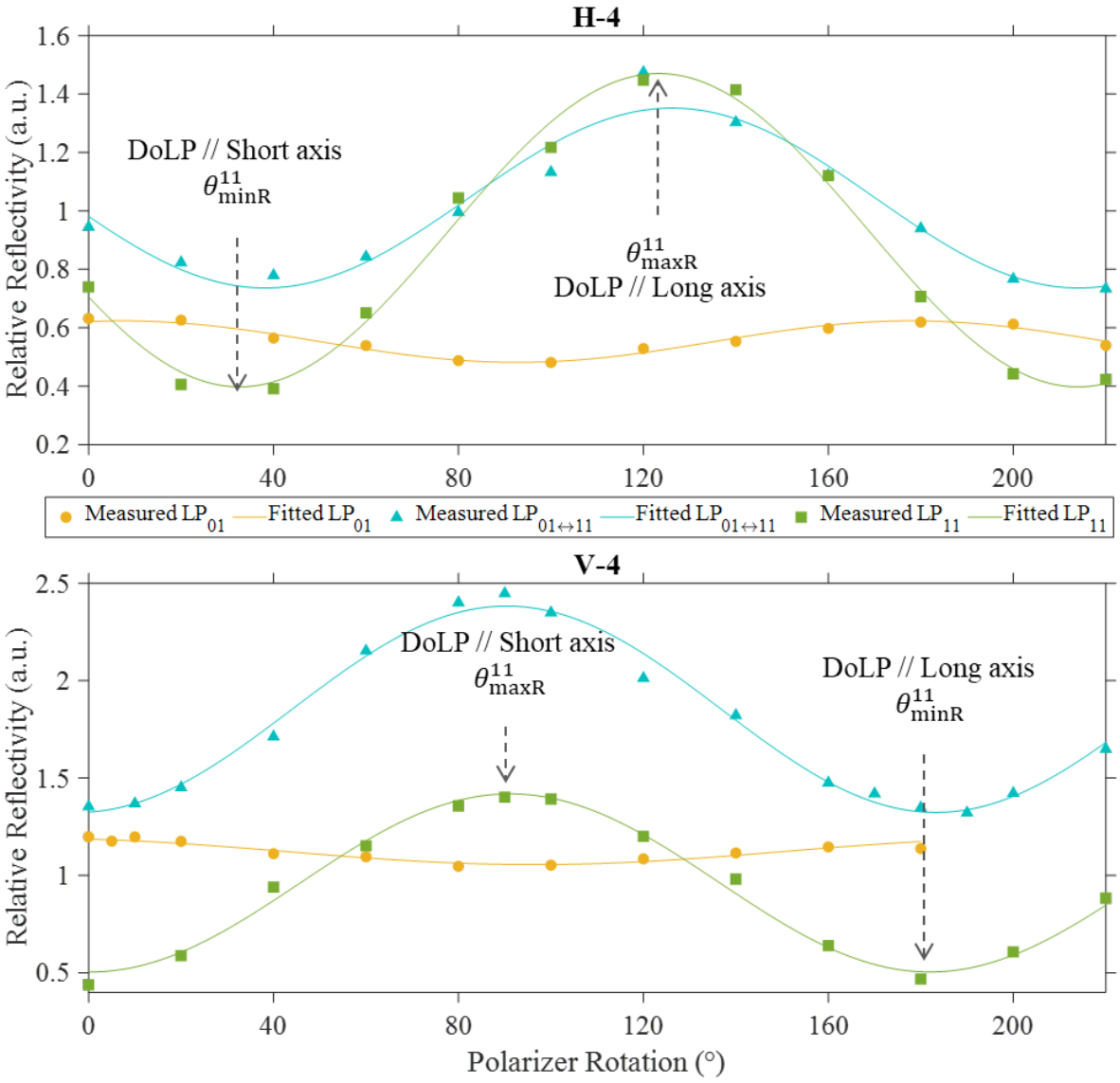

Figure 3.15: Reflectivity of the three LP modes of sample H-4 and V-4 under varied incident polarization.

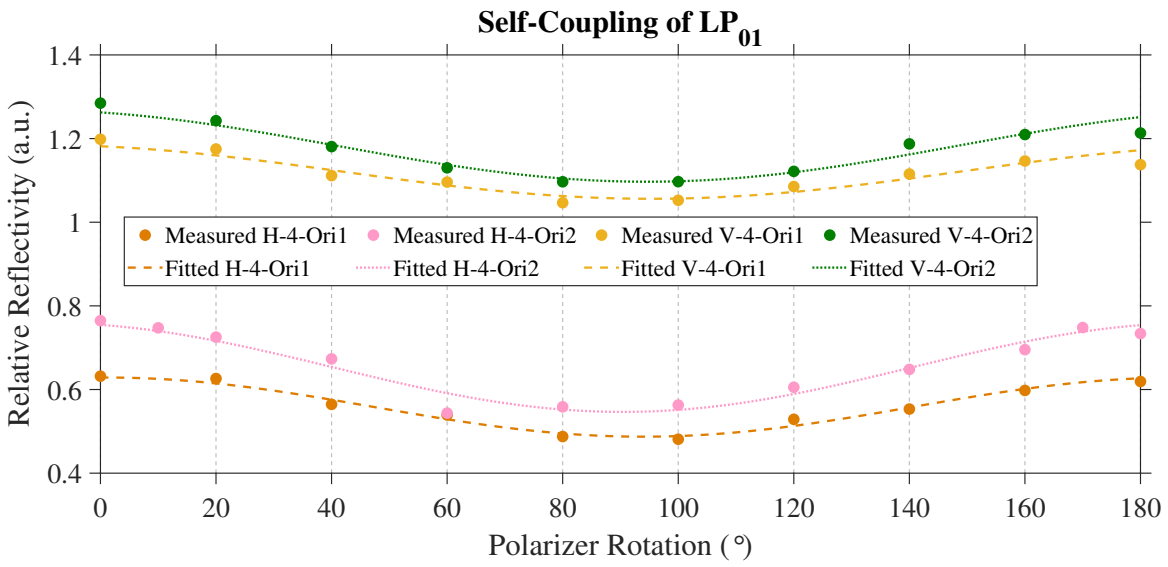

Figure 3.16: Polarization-dependent reflectivity of the LP_{01} under two different FBG orientations (Ori1 and Ori2).

when light is incident on an interface between two different optical media (e.g., glass and air), the transmittance differs for the s- and p-polarized waves, such phenomenon is well described by the Fresnel equations. In particular, the net effect of beam splitter on the normalized reflected signal $\mathbb{R}$ in Eq. (3.3b), and hence the reflectivity measured, is equivalent to a one-time transmission. The transmission at 1559 nm of p-polarized waves is 38.83% and 40.49% for s-polarized waves, according to the vendor-provided calibration of the beam splitter. This indicates the two transmission extrema of the beam splitter are almost 90° apart, which agrees well with the experimental results in Fig. 3.16. Other components that can introduce additional polarization dependence include the PD, the camera, the fiber facet, etc.

3.4.4 Polarization-controlled mode patterns

It is not only the reflectivity have dependence on the polarization, in this section, we show that the reflected mode pattern of the $LP_{01\leftrightarrow11}$ is also linked to the polarization. Moreover, the orientation of the mode pattern can be solely controlled by the DoLP of the incident laser light. As we mentioned before, the LP_{11} has four-fold degeneracy, two of which regards the spatial distribution. For example, with a fixed linearly polarized incident beam, there are two spatially degenerate LP_{11}, namely, the LP_{11a} with dumb line parallel to the DoLP and the LP_{11b} 90° rotated. Here we define the dumb line as the symmetrical axis separating the two lobes. In a TMF with FBG inscribed, the intensity profile of the reflected $LP_{01\leftrightarrow11}$ is a coherent superposition of the intensity profiles of the reflected LP_{01} and LP_{11}. The orientation of the reflected $LP_{01\leftrightarrow11}$ is therefore determined the reflected LP_{11} since LP_{01} is axial symmetrical. The intensity profiles of the reflected $LP_{01\leftrightarrow11}$ of sample H-4 are presented in Fig. 3.17(a); also presented in this figure are the intensity profiles of the reflected LP_{11}. All images are captured by the camera in Fig. 3.7 at their corresponding Bragg wavelengths. Moreover, to be more general, three distinct randomly-chosen excitation conditions (EC1-EC3) are tested for both directions of the linear polarization (DoLP-L and DoLP-S). To vary the excitation conditions, we manually tune the fiber input end to introduce different offsets between the fiber core and the focused beam (refer to Fig. 3.7), and therefore change the coupling coefficient of the free-space optical field to the individual LP mode (see Eq. (2.8)), which ultimately leads to varied proportions of the LP_{01}, LP_{11a}, and LP_{11b} as seen by the gratings. It is evident in Fig. 3.17(a) that the $LP_{01\leftrightarrow11}$ keeps a constant orientation regardless of the excitation conditions, once the DoLP is constant. Physically, this means the forward-propagating LP_{01} couples backwardly to only one spatial LP_{11}, and the spatial degeneracy of the LP_{11} is lifted. On the contrary, the reflected LP_{11} has varied orientations under different excitation conditions. Such variation is caused by a coherent combination of the two spatially

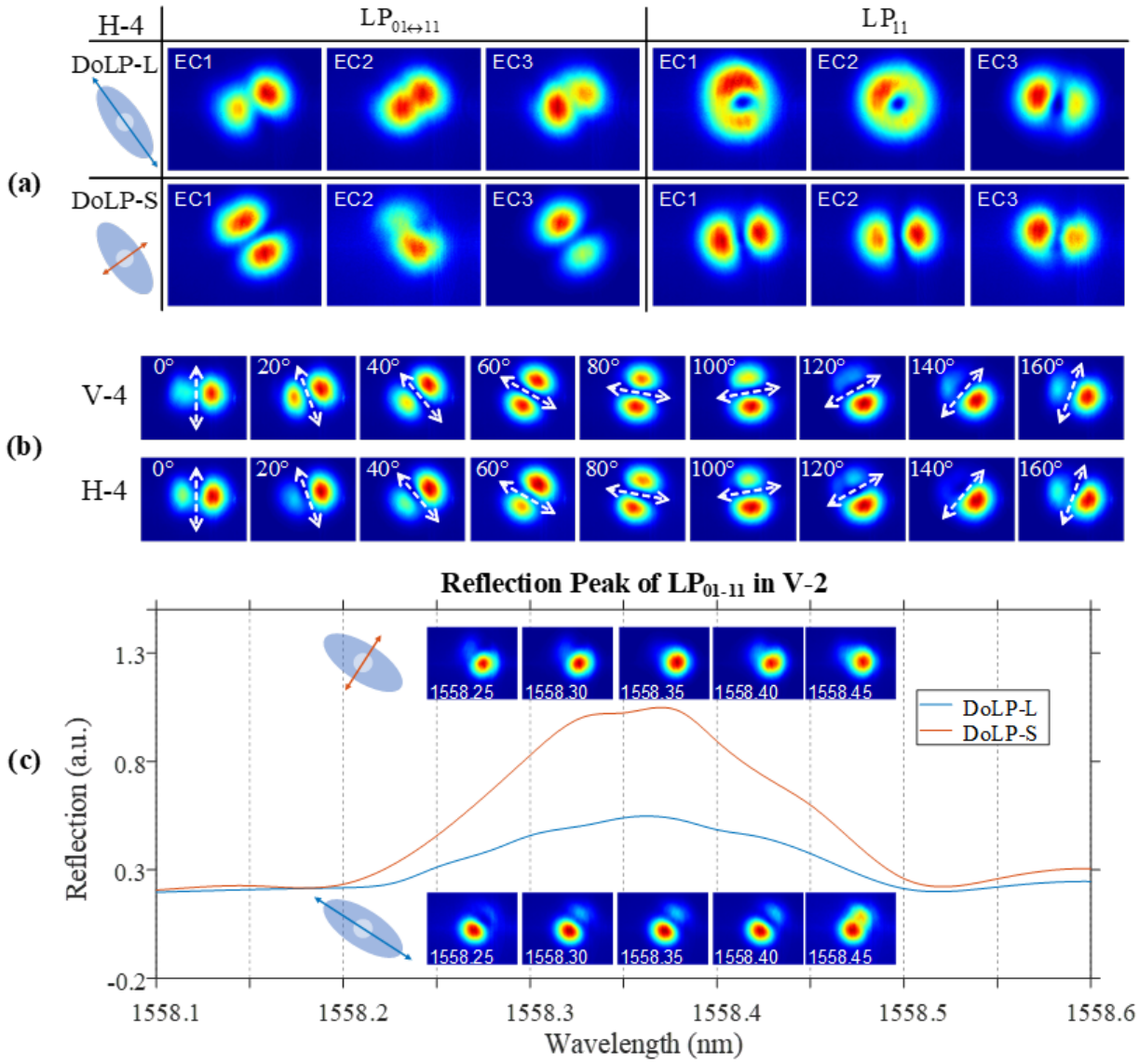

Figure 3.17: (a) Reflected intensity profiles of the $LP_{01\leftrightarrow11}$ and LP_{11} of H-4 captured at the corresponding Bragg wavelengths. (b) Reflected intensity profiles of the $LP_{01\leftrightarrow11}$ under varied DoLPs for sample V-4 and H-4. (c) Reflection spectra and associated reflected intensity profiles of the $LP_{01\leftrightarrow11}$ for sample V-2.

orthogonal LP_{11a} and LP_{11b}, which two are both involved in the self-coupling of the LP_{11}.

To further characterize the relationship between the DoLP and the orientation of the reflected $LP_{01\leftrightarrow11}$, we fix the excitation condition and rotate the linear polarization from 0° to 160° per 20°, the recorded mode patterns are displayed in Fig. 3.17(b). The DoLPs are marked by the double-headed arrows, and it is clear that the DoLP is parallel to the dumb line of the reflected $LP_{01\leftrightarrow11}$, which provides the potential to control the field pattern through polarization. Besides, we show in Fig. 3.17(c) the wavelength dependence of the reflected $LP_{01\leftrightarrow11}$ of sample V-2 as an instance. Both the intensity profiles of the relfected $LP_{01\leftrightarrow11}$ and the the reflection spectra are displayed. It can be seen that the there is little or no dependence of the intensity profiles of the reflected $LP_{01\leftrightarrow11}$ on the wavelength within the reflection bandwidth. It is worth noting that the properties we report in Fig. 3.17 are shared by all other off-axis TM-FBGs we fabricated, although only the H-4, V-4, and V-2 are presented.

We may now conclude this section by the stating that for FS-PbP off-axis TM-FBGs, the forward-propagating LP_{01} couples backwardly to only one spatially degenerate LP_{11} whose dumb line parallel to the DoLP, it suggests that one can manipulate the mode patterns through polarization merely. This property is reported for this first time to the best of our knowledge, although the orientation competition of the LP_{11} was mentioned in [53], it actually studied the relationship between the reflectivity and the LP_{11} orientation, and without polarization control.

3.5 Discussions

To quantitatively analyze the experimental results presented above, one may need to refine the conventional model for FBG spectra analysis [63]. First, the conventional model is

established under the approximation that the electric field in the perturbed waveguide can be expressed by the superposition of the ideal modes of the pristine waveguide, given that the presence of the grating is in fact dielectric perturbation. For the FBGs directly inscribed by FS pulses, however, the induced RIM or dielectric perturbation is rather strong which may induce significant modifications to the modal structure of the unperturbed fiber. In Fig. 3.18, we show the propagation of the individual LP mode under the presence of the damage points with FDTD simulation (Lumerical FDTD). For a better view, the cladding region is removed. Again, the red arrows indicate the propagation of the writing pulses, only two damage points are presented for our purpose. Here we only simulate the sample H-4 under DoLP-S for illustration. In the side-view of Fig. 3.18(a), the LP modes propagate from the "source plane" all the way upwards, and four monitoring planes are placed to record the evolution of the LP modes. One can see that the two damage points can induce noticeable modification on the intensity profile of the LP modes. Of our particular interest is T_4, the intensity profiles fail to recover their original status even without the presence of the damage points. Note that there are nearly five thousand damage points for a 5-mm-long FBG with grating pitch of 1.076 µm. It is therefore reasonable to propose that the presence of the damage points can alter the modal structure of the pristine fiber.

To investigate the resulting modal structure of the perturbed fiber, we may start with the extreme case, where the perturbation is uniform along the fiber axis, and its transverse profile takes the form of an ellipse with a central void circle (i.e., the 2D projection of the damage point). Such a case is presented in Fig. 3.19. In Fig. 3.19(a), we show the cross-section of a new waveguide, as well as its first six eigenmodes (Mode 1 to Mode 6). In particular, the perturbation is uniform along the fiber axis, with a void centered at $(0, 3)$ µm and a shell centered at $(-0.1, 3)$ µm, to imitate the laser-induced damage points that has additional RIM at the bottom. The size of the void is further based on the ratio of

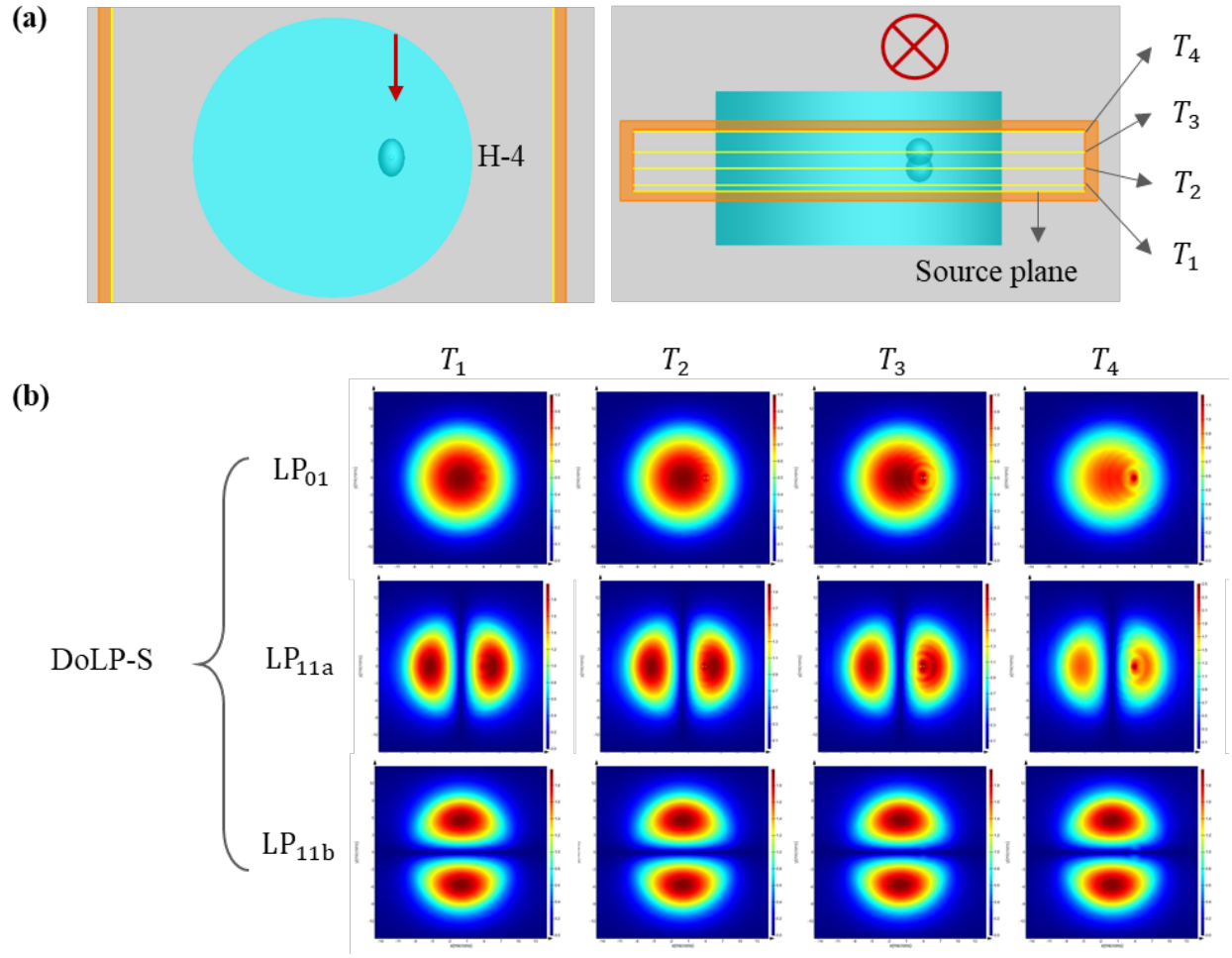

Figure 3.18: FDTD simulation of the mode propagation under the presence of the damage points. (a) Structure under tested. T_1–T_4: Monitoring planes. (b) Intensity profiles with single-mode excitation.

the Rayleigh range to the focal spot size of the objective used in the fabrication. The values of the refractive indices (n) of the void and shell are chosen arbitrarily but within the range from literature [62]. Also shown in Fig. 3.19(a) are the mode profiles of the first 6 eigenmodes, which correspond to the two-fold degenerate LP_{01} and four-fold degenerate LP_{11} modes of the ideal TMFs. The polarization of the eigenmodes is marked by the white arrow. Summarized in Fig. 3.19(b) is the effective refractive indices of the perturbed and the pristine

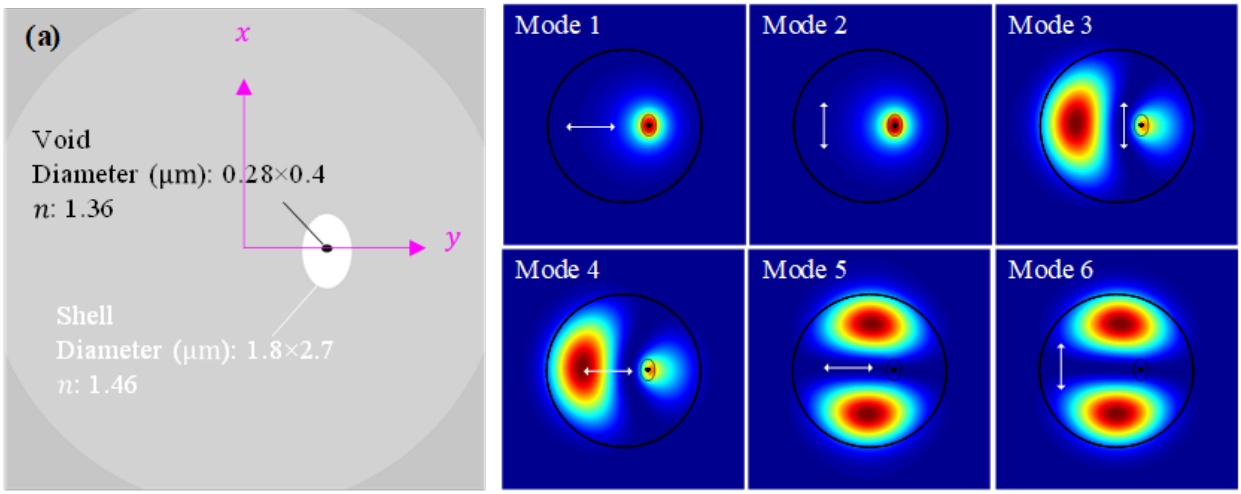

(b)	Mode 1	Mode 2	Mode 3	Mode 3	Mode 4	Mode 5
n_{eff} of the perturbed fiber	1.442640	1.442640	1.440628	1.440621	1.440279	1.440263
n_{eff} of the pristine fiber	LP_{01}: 1.441597		LP_{11}: 1.440251			

Figure 3.19: (a) Cross-section of the perturbed TMF and the mode profiles of the first 6 eigenmodes with polarization marked in white arrows. (b) Comparison of the effective refractive indices between the perturbed and the unpertubed fiber.

TMF used in this work. From Fig. 3.19 we can have a general view on the dissimilarities of the modal structure between the unperturbed TMF and the type-II-grating-perturbed one. Accordingly, the accuracy of the conventional model might be degraded due to the failure of the ideal-mode approximation.

Of more importance, we point out here, is that one may need to take into account the tensor nature of the dielectric perturbation. Note that in Eq. (3.6) and Fig. 3.19(a),

we have assumed that the void and the shell of the induced RIM are respectively uniform and isotropic. The experimental results, particularly the distinctive behavior of the PDPR of the LP_{01} and LP_{11} modes, strongly suggests that the dielectric perturbation induced in the type-II FBGs is in fact anisotropic. This necessitates the refinement of the conventional model utilizing the tensor form of the dielectric perturbation. For example, one may re-write Eq. (3.6) as

$$K_{kn} = \frac{\omega}{4} \iint \begin{bmatrix} \mathrm{E}^*_{k,x} & \mathrm{E}^*_{k,y} & \mathrm{E}^*_{k,z} \end{bmatrix} \cdot \begin{bmatrix} \Delta\varepsilon_{xx} & \Delta\varepsilon_{xy} & \Delta\varepsilon_{xz} \\ \Delta\varepsilon_{yx} & \Delta\varepsilon_{yy} & \Delta\varepsilon_{yz} \\ \Delta\varepsilon_{zx} & \Delta\varepsilon_{zy} & \Delta\varepsilon_{zz} \end{bmatrix} \begin{bmatrix} \mathrm{E}_{n,x} \\ \mathrm{E}_{n,y} \\ \mathrm{E}_{n,z} \end{bmatrix} dx\, dy. \tag{3.7}$$

The material properties of the laser-induced RIM, however, requires more precise characterization (particularly in its tensor form) in the future, and is beyond the scope of this work.

Chapter 4

Cross-axis TM-FBGs Inscribed with a FS Laser PbP Technique

Point-by-point (PbP) cross-axis Bragg gratings in a step-index two-mode fiber are fabricated by tightly-focused femtosecond laser pulses. The gratings are formed by inscribing a line of periodic damage points crossing the fiber axis at a certain tilting angle. In this chapter, we experimentally show that the reflections involving higher-order modes exhibit multiple mainband resonances with wavelength spacing proportional to the tilting angle. The results show that the combination of the higher-order modes and the PbP technique can add a new dimension to designing gratings with arbitrary spectral characteristics.

4.1 Introduction

Fiber Bragg gratings (FBGs) have been widely used in numerous applications including optical communication, sensing, and fiber laser technology. In general, a Bragg grating is formed by periodic perturbations along the wave propagation direction, and its frequency response can be featured by one or multiple narrowband reflections, depending on the number of modes that can interact with the periodic structure [17]. In practice, however, it is often desirable to create gratings with more complex frequency-response characteristics [64, 65, 66, 67]. For example, due to the finite grating length, uniform gratings with constant pitch-

averaged perturbation amplitude often suffer from sideband resonances, causing problems in WDM systems [68] and fiber laser applications [69]. To reduce the sideband reflection, apodization technique [64, 70] was introduced to sophisticatedly control the perturbation profile along the grating length, taking the form of a modified raised cosine function. In addition to suppressing the sidelobe of the Bragg grating, it is also of great interest to achieve desired bandwidth, rapid roll-off rate, and highly linearized dispersion-delay response, whcih can benefit applications such as dispersion compensators and wavelength-selective filters [64, 65, 66, 67, 71, 72, 73]. Furthermore, to obtain predetermined wavelength spacing, wide wavelength tuning range, and sharp wavelength selectivity for optical filtering and multi-wavelength lasing, in [66, 67], the elementary perturbation profile were periodically repeated. These approaches above to tailor the frequency-response characteristics of the grating, however, were limited to single-mode (SM) waveguides through modulating the perturbation profile alone, whereas the extra degrees of freedom provided by the higher-order modes (HOMs) have not been reported yet to the best of our knowledge.

Fabrication of FBGs with modulated perturbation profiles in SM fibers has been demonstrated using both phase masks [74] and point-by-point (PbP) technique [12]. With phase masks, the modulation can be achieved by varied diffraction efficiency [75] and local changes of the light intensity reaching the fiber [74], to name just a few. The phase mask technique often results in large laser-modified regions even with infrared femtosecond (FS) radiation [76]; with UV radiation and H_2-loaded fibers, the modified regions spread across the entire core such as in [74]. Moreover, the utilization of pre-made masks significantly reduces the inscription flexibility. In contrast, PbP inscription can modulate the perturbation of each pitch through a complete position control [41], owing to the use of objectives with high NA. PbP inscription of FBGs can be realized with both excimer lasers [40] and infrared FS lasers [41]. Compared to the UV-based PbP inscription, the FS PbP technique takes additional

advantages such as the obviation of photosensitization and the highly localized index modulation [5]. We therefore employ FS laser PbP technology for FBG fabrication in this work, as it provides the possibility of exploring the dependence of the gratings' spectral responses on the mode intensity profiles.

The main purpose of this chapter is to show that the HOMs can provide extra degrees of freedom for designing gratings with arbitrary frequency-response characteristics. Until now, to the extent of our knowledge, the exploit in arbitrary-response-design was reported only in SM waveguides via varying the perturbation profile alone [12, 64, 65, 66, 67, 77]. We demonstrate the extra design flexibility added by the HOMs via inscribing a straight-line of damage tracks crossing the axis of a step-index two-mode fiber (TMF) at a certain tilting angle. We fabricate multiple cross-axis FBGs with varied tilting angles, characterize their spectral properties, and identify each reflected linearly-polarized (LP) mode through mode-decomposition.

4.2 Design and fabrication of cross-axis TM-FBGs

The schematic of the cross-axis FBG is shown in Fig. 4.1, where the FS pulses, the TMF, and the damage points are out-of-scale for better illustration. As is shown, the damage points form a straight line which crosses the fiber axis in a plane perpendicular to the propagation direction of the FS pulses. The distances between the fiber axis and the two ends of the grating are the same and denoted by x µm. By varying the distance x we fabricate five cross-axis FBGs: X-2.5, X-5, X-7.5, X-10, and X-12.5, where X is the acronym of "cross", and the numbers represent the values of x in micrometers. A greater value of x corresponds to a larger tilting angle. Furthermore, all five gratings are 5-mm long with a pitch of 1.076 µm, this corresponds to a second-order FBG with Bragg wavelength designed around 1550 nm. The

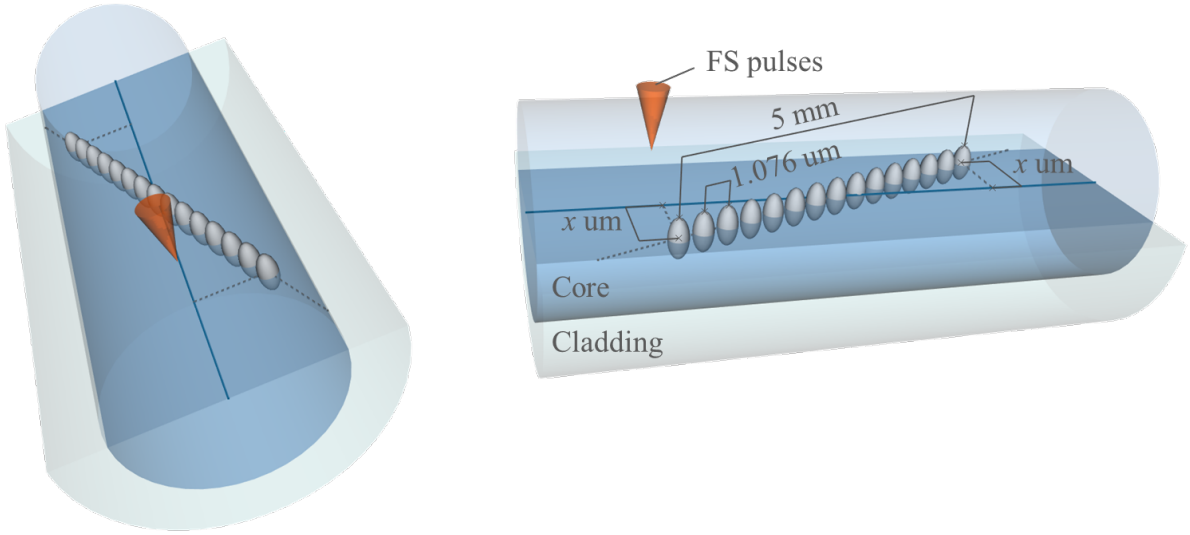

Figure 4.1: Out-of-scale schematic of a cross-axis FBG in a step-index TMF under two different views.

fabrication setup and procedure are similar to those descried in one of our previous work [78], and the setup is shown in Fig. 2.15. We use a regeneratively amplified Ti:Sapphire laser with 800 nm center wavelength, 500 Hz repetition rate, and ∼100 fs pulse width for fabrication. The energy per pulse is tuned to 128 nJ, which slightly exceeds the single-shot damage threshold of the glass [42]. The pulses are focused by a 100× oil-immersion objective (NA: 1.25) onto the TMF (OFS, 19 µm core diameter), which is mounted on an air-bearing 5-axis translation stage. Two representative microscope images of the damage points are displayed in Figs. 4.2(a) and 4.2(b), where the red arrows indicate the propagation direction of the FS pulses. It can be seen clearly that the damage point is featured as a central spherical void surrounded by a densified shell [55], closely resembling a spheroid. We note that due to the limited field of view, the microscope can only capture a rather short section (∼20 µm) of the 5-mm-long grating per frame, and therefore cannot reveal the geometrical shape of the damage track.

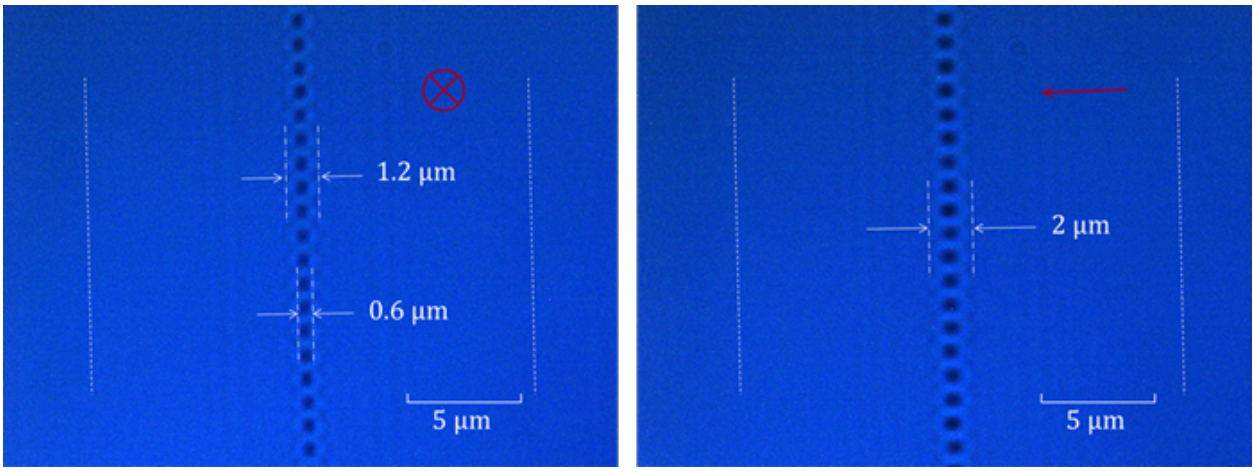

Figure 4.2: Representative (a) top-view and (b) side-view of the damage points, red arrows indicate the propagation direction of the FS pulses

4.3 Characterization of cross-axis TM-FBGs

To fully characterize the spectral properties of the FBGs, particularly with HOMs considered, a free-space-based setup depicted in Fig. 4.3 is used. This is because for most fiber-based FBG interrogators, their parameters such as the aperture and NA are designed for the SM fiber with core diameter less than 19 µm, such mismatch can partially block the signals carried by the HOMs whose energies spread out more towards the core-cladding interface, and therefore understate the reflectivity of the HOMs. A tunable laser generates a narrow-

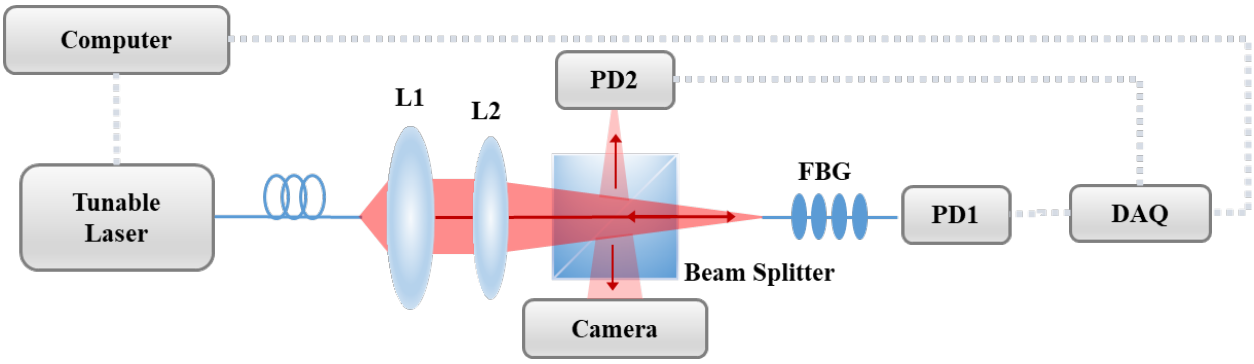

Figure 4.3: Experimental setup used to characterize the spectral properties of the cross-axis TM-FBGs. L1: collimator; L2: focusing lens; PD: photodiode.

linewidth continuous wave at a desired wavelength. The laser beam is then coupled into the TMF after passing through a collimator (L1), a focusing lens (L2), and a beam splitter. The TMF (∼2 m in length with the FBG inscribed near the distal end) is slightly bent to eliminate reflections from the LP_{21} and LP_{02}, which can propagate within a short distance in a straight TMF [78]. Out-of-fiber transmitted signals are collected by a photodiode (PD1), and reflected signals are captured by an infrared camera. The reflected optical power can be obtained by taking the sum over all pixels. To reveal the reflected mode patterns, an infrared camera (Goldeye, G-032) is uesd to detect the reflected signal, while the optical power can be obtained by summing all camera pixels. Prior to entering the fiber, the beam is partially reflected off the beam splitter to another PD (PD2), this signal is used to eliminate the influence of power fluctuations of the tunable laser during wavelength scanning. Additionally, PD2 is used to eliminate the influence of power fluctuations of the tunable laser during wavelength scanning. Consequently, a normalized transmitted signal $\mathbb{T}_\lambda$ and a normalized relative reflected signal $\mathbb{R}_\lambda$ can be obtained from Eq. (3.3) ($\mathbb{T}_\lambda = P_{1,\lambda}/P_{2,\lambda}, \mathbb{R}_\lambda = P_{\text{cam},\lambda}/P_{2,\lambda}$). Here we set the wavelength scanning rate to 0.01 nm/s, and keep all other parts of setup as still as possible during the scanning.

4.3.1 Spectra

The resulting spectra are shown Fis. 4.4–4.8 as dash-dotted traces. The solid curves are Gaussian fittings. The reflection spectra with respect to the left axis in blue are normalized by a background reflection $\mathbb{R}_0$ along with a total coupled-in power $\mathbb{T}_0$ via $(\mathbb{R} - \mathbb{R}_0)/\mathbb{T}_0$, and the transmission spectra shown by the right axis in red are normalized through $\mathbb{T}/\mathbb{T}_0$. $\mathbb{R}_0$ and $\mathbb{T}_0$ are obtained at a wavelength longer than the rightmost resonance, and they need characterizing for each scanning trial. Besides, to show higher dynamic range and better spectral resolution, in the insets we present the reflection spectra in decibels measured by a

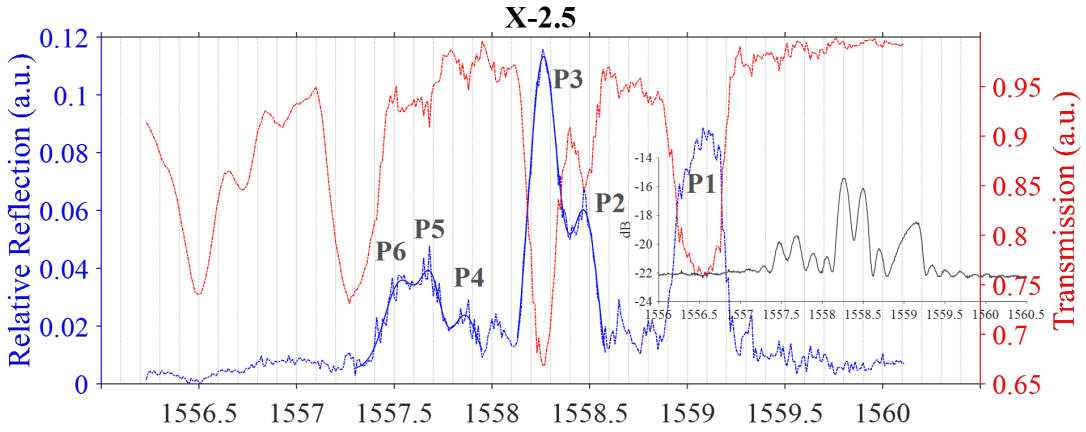

Figure 4.4: Transmission and reflection spectra of sample X-2.5.

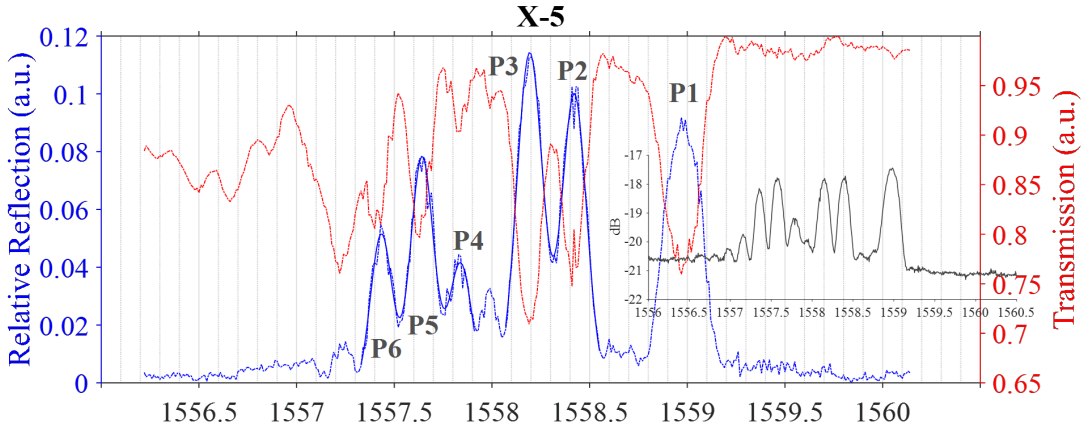

Figure 4.5: Transmission and reflection spectra of sample X-5.

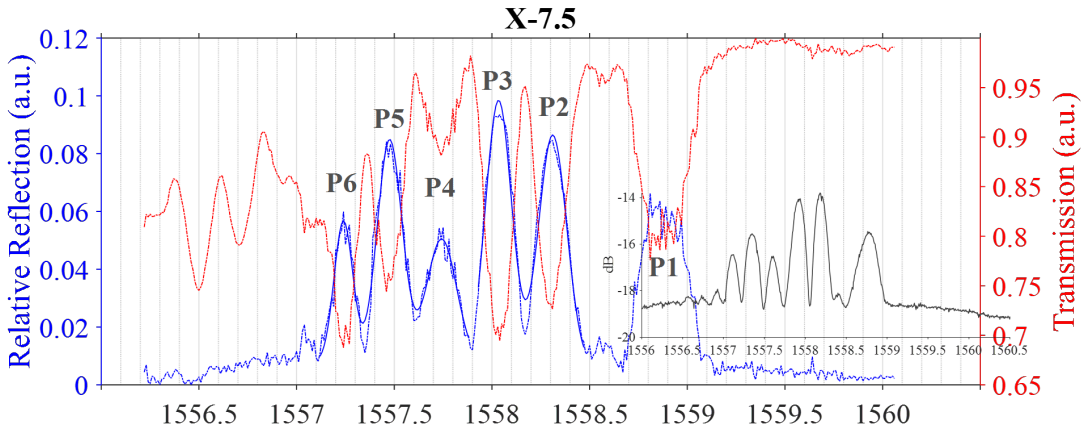

Figure 4.6: Transmission and reflection spectra of sample X-7.5.

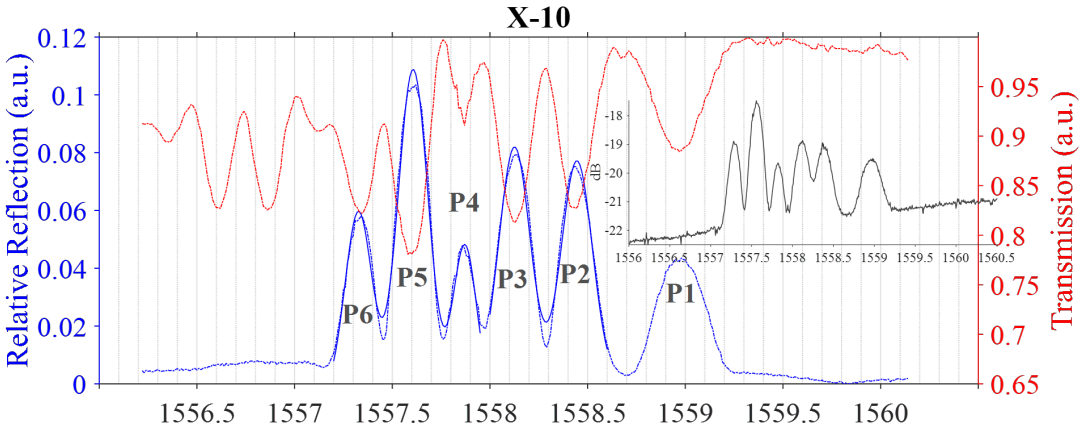

Figure 4.7: Transmission and reflection spectra of sample X-10.

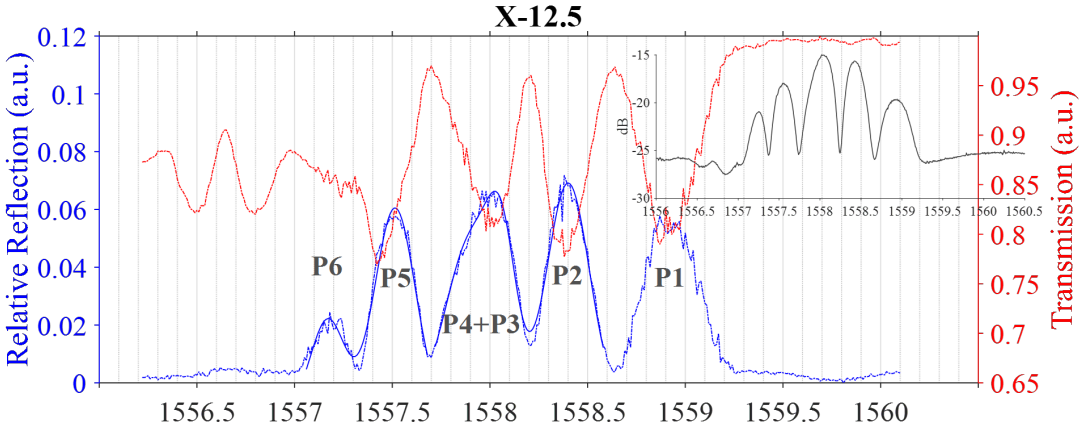

Figure 4.8: Transmission and reflection spectra of sample X-12.5.

swept-laser spectrometer (Micron optics, SM125), nut note that the reflection shown in the insets cannot reveal the actual reflection strength, since the spectrometer is connected with a standard SM fiber, of which the core is positioned with lateral offset to the core of the TMF to excite the HOMs. Unlike the conventional TM-FBGs (FBG in TMFs) which show at most three main reflection peaks, namely, the self-coupling of the LP_{01} and the LP_{11}, and optionally the cross-coupling of the LP_{01} and LP_{11} ($LP_{01\text{-}11}$), the cross-axis TM-FBGs exhibit six primary reflection peaks, as marked in the spectra. Note that for the X-12.5 in Fig. 4.8, we denote the middle peak as "P4+P3", and fit it by a sum of two Gaussian functions. It is also worth noting that in Fis. 4.4–4.8, the random but minor fluctuations along the traces is primarily caused by the limited frame rate of the camera (25 Hz); the additional transmission losses at the shorter wavelengths are caused by couplings to the cladding and radiation modes.

In addition to an increased number of peaks, it can also be seen that the wavelength spacing of the peaks varies with the tilting angle. We intentionally choose $\Delta\lambda_{56}$ (wavelength difference between P5 and P6), $\Delta\lambda_{45}$, and $\Delta\lambda_{23}$ to represent wavelength spacing, the rationale behind it will be explained in the following paragraph. The peak wavelengths are acquired through Gaussian fittings shown in Fis. 4.4–4.8. As summarized in Fig. 4.9, where each $\Delta\lambda_{ij}$

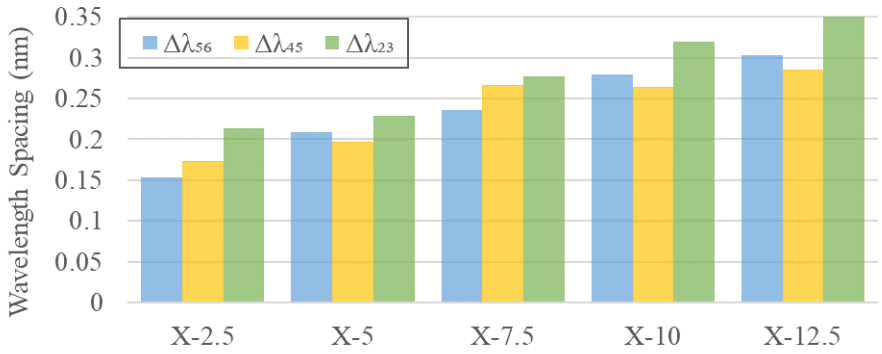

Figure 4.9: Measured wavelength spacing.

are presented in distinct colors, we can see that all three $\Delta\lambda$ increase with increasing tilting angle. Furthermore, generally $\Delta\lambda_{23}$ is greater than other two in each grating sample.

4.3.2 Identification of reflection peaks (mode-decomposition)

Now we give the reasons of utilizing $\Delta\lambda_{56}$, $\Delta\lambda_{45}$, and $\Delta\lambda_{23}$ as representatives of wavelength spacing. As an example, the reflected mode patterns of sample X-7.5 are present in Fig. 4.10, they are captured by the camera shown in Fig. 4.3 at each reflection peak. Empirically, from

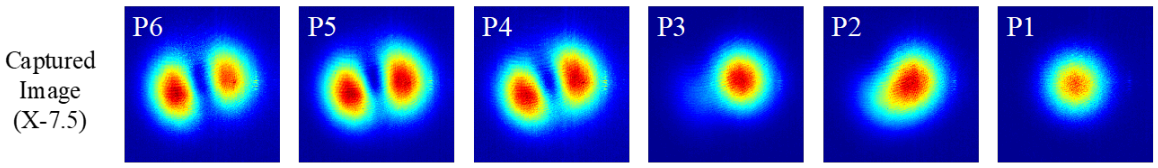

Figure 4.10: Intensity profiles at the peak reflections of sample X-7.5.

the shape of the intensity profiles merely, it is reasonable to attribute P1 as the self-coupling of the LP_{01}, P2 and P3 the cross-coupling of the $LP_{01\text{-}11}$, and P4–P6 the self-coupling of the LP_{11}.

To evaluate this statement, one needs to quantify the mode compositions based on the intensity profile. In principle, it is well-known that transverse optical field of a step-index TMF can be expressed as superposition of three spatial LP modes, namely, LP_{01}, LP_{11a}, and LP_{11b}, under the weakly-guiding approximation:

$$I(x,y) = \Big|\sum_{lm} A_{lm}\exp(i\theta_{lm})\mathbf{e}_{lm}(x,y)\Big|^2, \tag{4.1}$$

where $A_{lm}\exp(i\theta_{lm})$ is the complex amplitude of the LP_{lm}, and $\mathbf{E}_{lm}$ is the electric field

distribution normalized by

$$\iint |\mathbf{e}_{lm}(x,y)|^2 \, dx \, dy = \frac{2\omega\mu}{\beta_{lm}}. \tag{4.2}$$

Therefore, mode-decomposition based on the optical intensity profile can be formulated as a nonlinear optimization problem. The flowchart is shown in Fig. 4.11. The vector $\mathbf{X}$ in

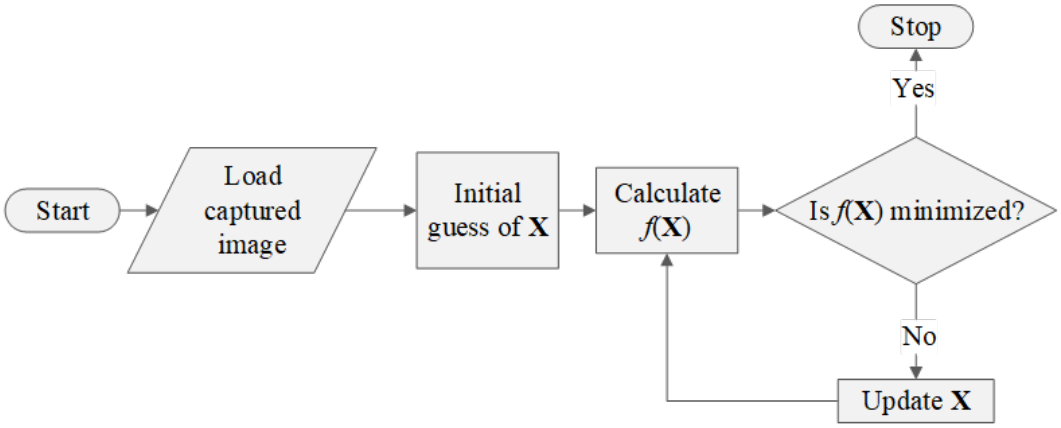

Figure 4.11: Flowchart of the nonlinear optimization process for mode-decomposition.

Fig. 4.11 is defined as

$$\mathbf{X} = \left[A_{01} = 1, \theta_{01} = 0, A_{11\mathrm{a}}, \theta_{11\mathrm{a}}, A_{11\mathrm{a}}, \theta_{11\mathrm{b}}\right] \tag{4.3}$$

with four unknowns to be found. The objective function $f(\mathbf{X})$ can be defined as

$$f(\mathbf{X}) = 1 - \frac{\sum\limits_{x,y} \left(I_{\mathrm{cam}}(x,y) - \bar{I}_{\mathrm{cam}}\right)\left(I_{\mathbf{X}}(x,y) - \bar{I}_{\mathbf{X}}\right)}{\sqrt{\sum\limits_{x,y} \left(I_{\mathrm{cam}}(x,y) - \bar{I}_{\mathrm{cam}}\right)^2 \sum\limits_{x,y} \left(I_{\mathbf{X}}(x,y) - \bar{I}_{\mathbf{X}}\right)^2}}, \tag{4.4}$$

where I_{cam} represent the captured images as shown in Fig. 4.10; $I_{\mathbf{X}}$ is the reconstructed image with (4.3) substituted into (4.1). Here we apply one constraint to the optimization problem, i.e., $A_{11} \in [0, 100]$. For one captured image, the optimization process using MATLAB

(Mathworks, 2018) on a personal laptop takes ∼3 minutes.

In Fig. 4.12 we display the reconstructed images using the optimized vector $\mathbf{X}$, along with their complex amplitudes and the amount of the LP_{01}. $LP_{01}\%$ is calculated through

$$LP_{01}\% = \frac{|A_{01}|^2}{|A_{01}|^2 + |A_{11a}|^2 + |A_{11b}|^2} \times 100\%. \tag{4.5}$$

Supported by $LP_{01}\%$, it is evident that P6, P5, and P4 correspond to the self-coupling of

Reconstructed Image (X-7.5)	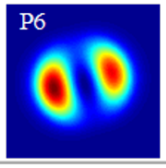 P6	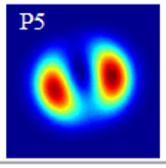 P5	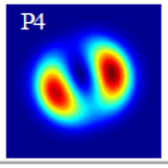 P4	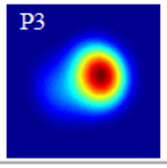 P3	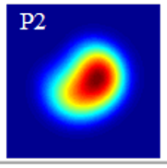 P2	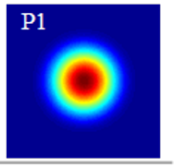 P1
Correlation coefficient	0.9740	0.9769	0.9758	0.9899	0.9919	0.9943
A_{11a}	20.2634	3.9751	4.7104	0.5909	0.4535	0.0261
θ_{11a}	2.8249	1.3990	5.0036	0.9244	5.1369	5.2268
A_{11b}	9.8265	1.8178	2.6510	0.2140	0.3434	0.0014
θ_{11b}	3.9190	2.5082	3.9433	1.1078	4.5333	0.9796
$LP_{01}\%$	0.20%	4.97%	3.31%	71.69%	75.55%	99.93%

Figure 4.12: Reconstructed mode patterns along with the their complex amplitudes and the amount of the LP_{01} ($LP_{01}\%$) after optimization.

the LP_{11}, P3 and P2 represent the cross-coupling of the LP_{11} and LP_{01} ($LP_{01\text{-}11}$), whereas P1 stands for the self-coupling of the LP_{01}, although the LP_{01} is still present in P6-P4 with percentage less than 5%, and similarly the LP_{11} in P1. This impurity is likely caused by the random coupling between the two LP modes after reflected by the grating as the fiber is slightly bent. Further, we use the near-fields for the optimization process, whereas it is the far-fields that are captured by the camera.

4.4 Numerical simulation

Qualitatively, one can interpret the spectral response of a grating as the Fourier transform of the coupling profile along the grating [79] that is determined by the transverse overlap between the perturbation and the mode intensity profiles [63]. For example, the magnitude of the coupling-profile envelope of the LP_{11} in the cross-axis TM-FBGs we fabricated can be treated as a "symmetric bimodal distribution" with peak separation inversely proportional to the tilting angle. The spectral separation, after Fourier transformation of the coupling profile, is therefore proportional to the tilting angle. Quantitatively, coupled-mode theory is a well-developed framework to model various fiber gratings [63, 79], however, the implementation into the PbP-inscribed cross-axis gratings is not straightforward, particularly with the HOMs involved. We therefore start with building a numerical model for the PbP gratings with several assumptions.

4.4.1 Numerical modelling of PbP gratings

In general, under the assumption of weak perturbation and negligible longitudinal component, one can express the transverse component of the coupling coefficient between the k-th n-th modes as

$$K_{kn}^{t}(z) = \frac{\omega}{4} \iint \mathbf{e}_{k}^{t*} \cdot \Delta\varepsilon(x, y, z)\mathbf{e}_{n}^{t}\, dx\, dy, \tag{4.6}$$

where z is implicitly defined as the direction of the fiber axis, $\mathbf{e}^{t}$ represents the transverse component of a waveguide mode normalized by Eq. (4.2), we re-write this equation here:

$$\iint |\mathbf{e}(x, y)|^{2}\, dx\, dy = \frac{2\omega\mu}{\beta}. \tag{4.7}$$

For the PbP-inscribed cross-axis gratings, one can still model $K^t_{kn}(z)$ as a periodic function along z with a modified envelope which also varies along z:

$$K^t_{kn}(z) = K^{\text{env}}_{kn}(z)\Delta\varepsilon^{\text{eq}}_z(z). \tag{4.8}$$

Periodicity

We first work on the periodicity $\Delta\varepsilon^{\text{eq}}_z(z)$. As shown in Fig. 4.2, each damage point consists of a micro-void surrounded by a densified shell, resembling a spheroid with featuring radius of h, w, and w. Assuming a constant refractive index of the regions where the FBGs are to be inscribed, and hence identical damage points, the periodicity is therefore a projection of the perturbation profile onto the fiber axis. We further assume that the voids would dominate once present, and the shells take effect only in the regions between two adjacent voids. Since the damage point is small as compared to the fiber core, the optical field can be treated uniform within one damage point, based on which we expand the transverse dimension of the void to the same size as the shell. The comparison between the spheroidal damage points and the simplified structure is shown in Fig. 4.13 viewed from varied angles. The vertical displacement between the damage points and the simplified structure are manually induced in Figs. 4.13(a) and 4.13(c) for better view, virtually there is no displacement except the projection onto the fiber axis. As shown in Fig. 4.13(a) for example, one grating period, denoted as "unit", is simplified as one void-layer ($\Delta\varepsilon^{eq}_v$) plus one shell-layer ($\Delta\varepsilon^{eq}_s$), shaped as a cylinder with an elliptical cross-section; h and w denote the major and minor axes. Λ_z is the grating pitch projected onto z, and d_s represents the width of the shell-layer. The resulting periodicity can therefore be modelled as alternating layers as illustrated in Fig. 4.14. Thus the periodicity after simplification is equivalently a pulse-wave function, as plotted in Fig. 4.15, the subscript z presents the z-projection. This pulse wave can be expanded into

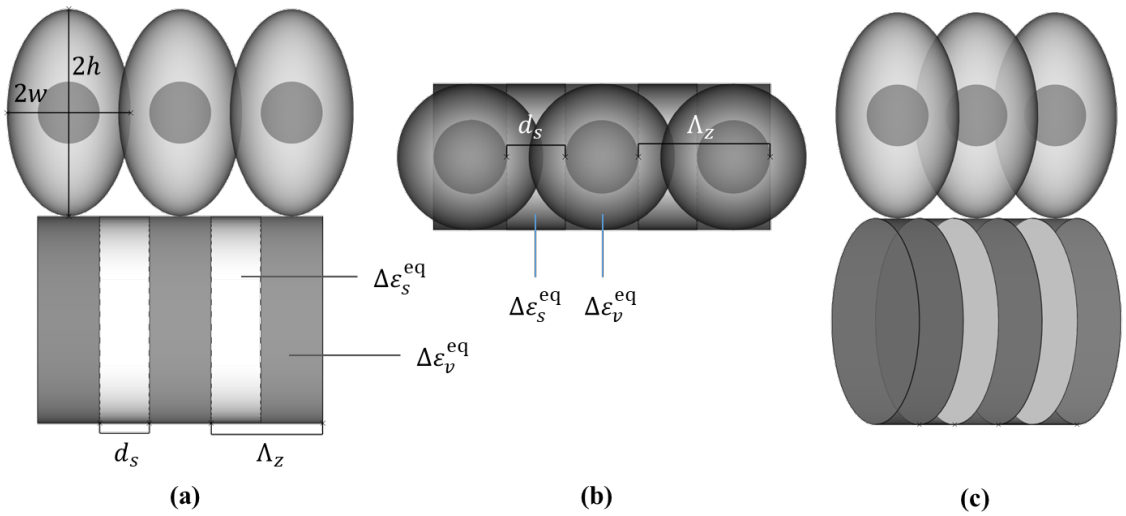

Figure 4.13: Comparison between the damage points and the simplified structure viewed from varied angles in (a), (b), and (c).

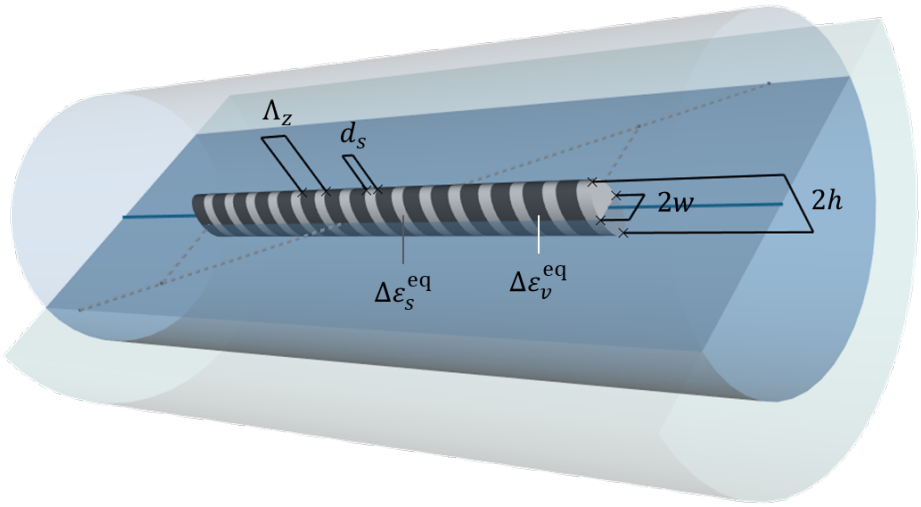

Figure 4.14: Out-of-scale illustration of simplified PbP grating periodicity.

Fourier series:

$$\Delta\varepsilon_z^{eq}(z) = \Delta\varepsilon_A\left[\frac{d_s}{\Lambda_z} - \frac{|\Delta\varepsilon_v^{eq}|}{\Delta\varepsilon_A} + \sum_{n=1}^{\infty}\sin(n\pi\frac{d_s}{\Lambda_z})\cos(n\frac{2\pi}{\Lambda_z}z)\right], \tag{4.9}$$

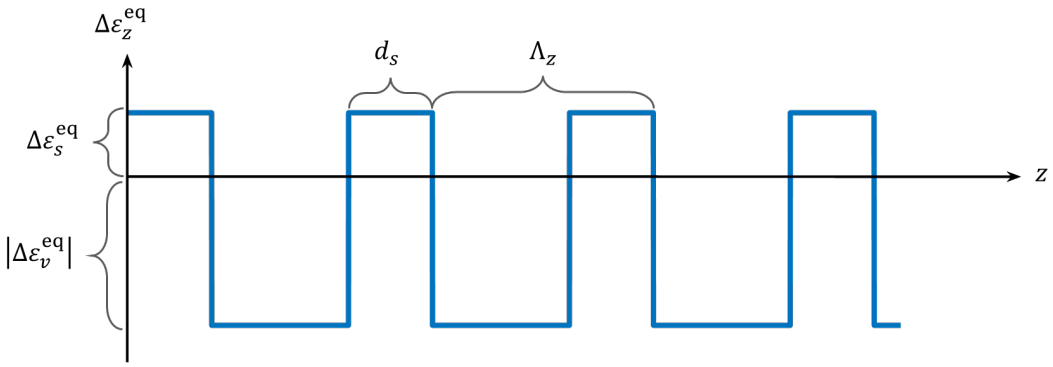

Figure 4.15: Simplified perturbation profile along the fiber axis.

where

$$\Delta\varepsilon_A = \Delta\varepsilon_s^{\mathrm{eq}} + |\Delta\varepsilon_v^{\mathrm{eq}}| \tag{4.10}$$

signifies the amplitude of the pulse wave. For a second-order grating of our interest, only the DC and $n = 2$ terms are kept.

Envelope function

We next work on the perturbation's envelope function $K_{kn}^{\mathrm{env}}(z)$ which also varies along the grating length. To do so, we apply (4.6) to a single transverse slice of each "unit" at its original position before projected onto the z-axis. In particular, the $\Delta\varepsilon(x, y, z)$ used for finding $K_{kn}^{\mathrm{env}}(z)$ is only a logic function true for the regions within the unit, for example, for the i-th unit centered at (x_i, y_i, z_i),

$$\Delta\varepsilon^{\mathrm{env}}(x, y, z_i) = \begin{cases} 1 & \frac{(x-x_i)^2}{h^2} + \frac{(y-y_i)^2}{w^2} \leq 1 \\ 0 & \text{otherwise.} \end{cases} \tag{4.11}$$

In Fig. 4.16, we display the resulting transverse overlaps for the sample X-7.5 in three individual cases, namely, the self-coupling of the LP_{01} ($LP_{01\text{-}01}$), the cross-coupling of the LP_{01} and LP_{11} ($LP_{01\text{-}11}$), and the self-coupling of LP_{11} ($LP_{11\text{-}11}$). The size of the damage points are from experimental characterization in Fig. 4.2 with $h = 1$ µm and $w = 0.6$ µm. $\Delta\varepsilon^{\text{env}}(x, y, z_1)$ presents the first unit at $z = z_1$; the mode pattern shown in the upper half denote the electric fields normalized using Eq. (4.7). For the case of $LP_{11\text{-}11}$, we use the doughnut-shaped electric field of the HE_{21} in order to eliminate the variation induced by the orientation of the LP_{11}. In $LP_{01\text{-}11}$, however, the LP_{11a} and LP_{11b} are applied. This is because the LP_{01} is linearly polarized, it can only couple to the other modes that have the same polarization (see the vector fields used in Eq. (4.6)), with such a polarization restriction, the hybrid modes HE_{21},TE_{01}, and TM_{01} are in fact two-lobed. In addition, to account for the orientation variations, 50% LP_{11a} and 50% LP_{11b} are considered. Consequently, a 2D

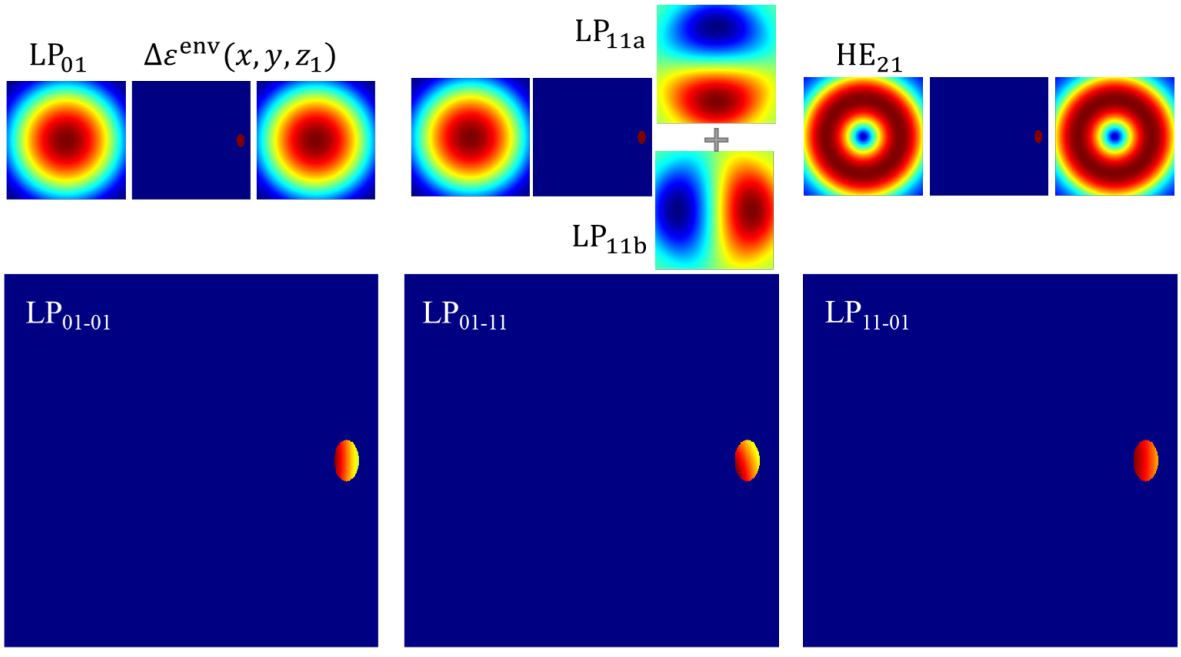

Figure 4.16: Transverse overlap between the LP modes and the perturbation at the first unit of sample X-7.5.

integral of the these transverse overlaps yields $K_{kn}^{\text{env}}(z_1)$. Similar 2D integral is performed for

each unit sequentially (∼5000 times in our case), and the resulting envelop function $K_{kn}^{\text{env}}(z)$ of sample X-7.5 is presented in Fig. 4.17, where the LP_{01} and LP_{11} are equally presented.

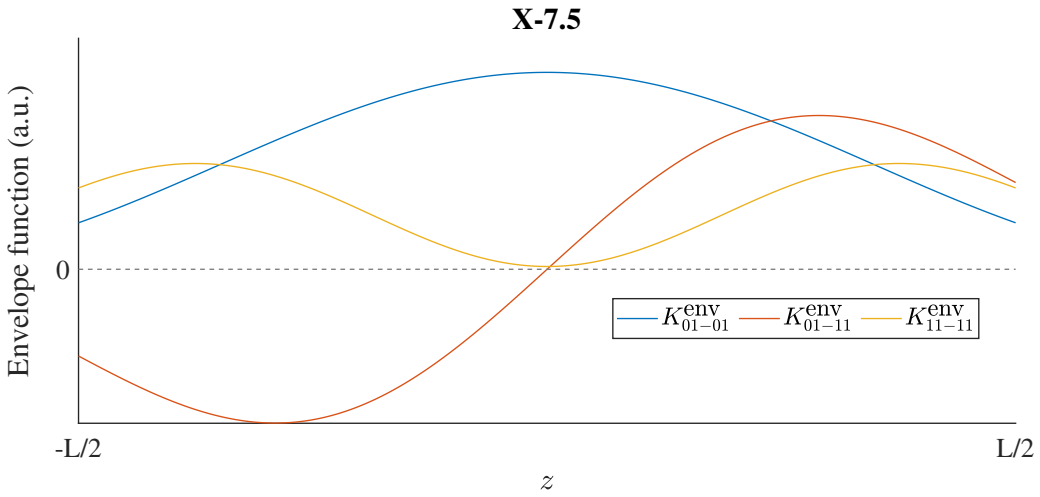

Figure 4.17: Envelope function of sample X-7.5, with equally excited LP_{01} and LP_{11}.

4.4.2 Implementation of coupled-wave analysis to PbP gratings

Following the standard coupled-wave theory [19, 80], with the ideal-mode approximation, we can express an arbitrary optical field presented the optical fiber in the form of its electric field:

$$\mathbf{E}(x,y,z,t) = \sum_k \left[A_k(z)\exp(-i\beta_k z) + B_k(z)\exp(i\beta_k z)\right]\cdot \mathbf{e}_k(x,y)\exp(i\omega t), \tag{4.12}$$

where A_k and B_k are the slowly varying amplitudes of the forward- and backward-propagating k-th mode $\mathbf{e}_k$, which is the normal mode of an ideal fiber with the orthogonality relation of

$$\frac{|\beta_k|}{2\omega\mu}\int \mathbf{e}_n^*(x,y)\cdot\mathbf{e}_k(x,y)\,dx\,dy = \delta_{kn}. \tag{4.13}$$

Substitution of Eq. (4.12) into the Maxwell equations, one can obtain the following well-known form of the coupled-wave equation [80]:

$$\begin{aligned}\frac{dA_n}{dz} =& -i\sum_k A_k(K_{kn}^t + K_{kn}^z)\cdot\exp\big[-i(\beta_k-\beta_n)z\big] \\ & -i\sum_k B_k(K_{kn}^t - K_{kn}^z)\cdot\exp\big[i(\beta_k+\beta_n)z\big]\end{aligned} \tag{4.14a}$$

$$\begin{aligned}\frac{dB_n}{dz} =& i\sum_k A_k(K_{kn}^t - K_{kn}^z)\cdot\exp\big[-i(\beta_k+\beta_n)z\big] \\ & +i\sum_k B_k(K_{kn}^t + K_{kn}^z)\cdot\exp\big[i(\beta_k-\beta_n)z\big].\end{aligned} \tag{4.14b}$$

Since in general the longitudinal coefficient $K_{kn}^z(z)$ is far less than the transverse coefficient $K_{kn}^t(z)$ and therefore can be neglected. $K_{kn}^t(z)$ takes the same form as in Eq. (4.6). For PbP gratings, with the numerical model we just described in 4.4.1, with Eqs. (4.8), (4.9), and (4.10) in particular, we can introduce the "DC" (σ) and "AC" (κ) coupling coefficients for the second-order PbP-FBG as

$$\sigma_{kn}(z) = K_{kn}^{\text{env}}(z)\cdot\Delta\varepsilon_A\Big(\frac{d_s}{\Lambda_z} - \frac{|\Delta\varepsilon_v^{\text{eq}}|}{\Delta\varepsilon_A}\Big) \tag{4.15a}$$

$$\kappa_{kn}(z) = K_{kn}^{\text{env}}(z)\cdot\Delta\varepsilon_A\frac{1}{2\pi}\sin(2\pi\frac{d_s}{\Lambda}), \tag{4.15b}$$

such that

$$K_{kn}^t(z) = \sigma_{kn}(z) + 2\kappa_{kn}(z)\cos(\frac{2\pi}{\Lambda/2}z), \tag{4.16}$$

expressed in the same way as [63]. It can be seen that for the PbP-inscribed gratings, σ and κ are related through the Fourier series expansion of the pulse wave, instead of via the fringe visibility of the sinusoidal wave for the holographic-inscribed gratings in [63]. The envelope function $K_{kn}^{\text{env}}(z)$ can be found by following the steps in 4.4.1. As an example, we show in

Fig. 4.18 the σ and κ of sample X-7.5, with the same parameters used for Fig. 4.17, and additionally parameters listed in Table 4.1 where $\Delta n_v^{\text{eq}} = -0.015$ is used.

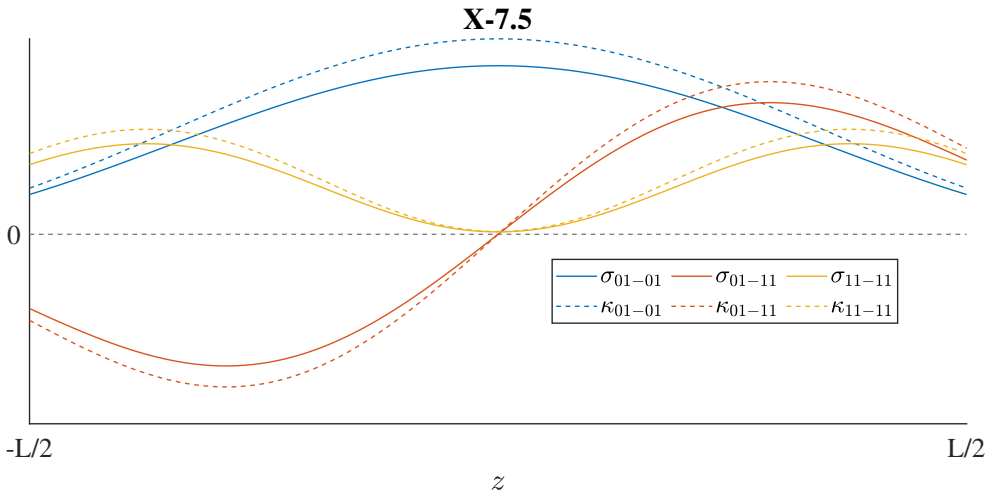

Figure 4.18: DC (σ) and AC (κ) coupling coefficients of sample X-7.5, with equally excited LP_{01} and LP_{11}.

We then combine Eqs. (4.14) and (4.16), and neglect the fast-changing terms contributing to the first-order derivative of the slowly varying amplitudes, we can finally have the simplified coupled-wave equation:

$$\frac{dR}{dz} = -i\left(\sigma + \delta - \frac{1}{2}\frac{d\phi}{dz}\right)R - i\kappa S \tag{4.17a}$$

$$\frac{dS}{dz} = i\left(\sigma + \delta - \frac{1}{2}\frac{d\phi}{dz}\right)S + i\kappa R, \tag{4.17b}$$

where δ is defined as the offset to the designed propagation constant β_D and takes the form of

$$\delta = \beta - \beta_D. \tag{4.18}$$

In addition, R and S are related to A and B in Eq. (4.14) through

$$A = Re^{i(\delta+\sigma)z} \tag{4.19a}$$

$$B = Se^{-i(\delta+\sigma)z} \tag{4.19b}$$

From Eq. (4.17), one can obtain a Riccati differential equation for the amplitude reflection coefficient ρ [79]:

$$\frac{d\rho}{dz} = i\Big(2\delta + 2\sigma - \frac{d\phi}{dz}\Big)\rho + i\kappa(1+\rho^2). \tag{4.20}$$

Since the Bragg grating is designed to have no chirp, here we set $d\phi/dz = 0$, and after separating the phase and magnitude terms, we finally have:

$$\rho = -i\int_{-L/2}^{L/2} \kappa(z)e^{-i2(\delta+\sigma)z}\,dz. \tag{4.21}$$

4.4.3 Simulated spectra

We first list the parameters used for MATLAB (Mathworks, 2018) simulation in this section as in Table 4.1. In particular, Λ_z is regarded the same as the grating pitch inscribed (Λ=1.076 um), since their difference can be neglected (0.014 nm for X-12.5). The sizes of the ellipse (h and w) and d_s are based on the measurement in Fig. 4.2. The mode composition (LP_{01}% and LP_{11}%) is based Fig. 4.12, taking the mean of P3 and P2. The perturbation to the refractive index Δn is related to the perturbation to the permittivity $\Delta\varepsilon$ through

$$\Delta\varepsilon \approx 2n_1\Delta n \cdot \varepsilon_0. \tag{4.22}$$

The value of Δn_s ranges from 0.001 to 0.05 in literature [62], here we fix Δn_s^{eq} to 0.04 while varying Δn_v^{eq} from -0.001 to -0.05. For X-7.5, we find that when $\Delta n_v^{\text{eq}} = -0.015$, the

Table 4.1: Parameters used for simulation

Parameter	Value
Core index n_1	1.4425
Cladding index n_2	1.4375
Λ_z (µm)	1.076
h (µm)	1
w (µm)	0.6
d_s (µm)	0.4
LP_{01}%	27%
LP_{11}%	73%
Δn_s^{eq}	0.04
Δn_v^{eq}	-0.001 to -0.05

simulation shows the best agreement with the experimental data regarding the reflection strength (based on the transmission spectra in Fig. 4.6). The resulting simulated spectrum of X-7.5 is shown in Fig. 4.19 in solid black, which is obtained by summing up the individual spectrum of the three LP modes represented in varied colors. For better comparison, the experimentally measured spectrum from Fig. 4.6 is also overlaid here in magenta. We notice a blue shift of the simulated spectra in Fig. 4.19 compared with the measured spectra, this is likely caused by the difference between the actual and the as-stated fiber indices. The blue shift, however, applies to the entire range of the wavelengths and thus have little effect on the wavelength spacing of our interest. Furthermore, we also note the relative strong reflectivity of the $LP_{01\text{-}11}$ in simulation is likely due to we have a predetermined 50% LP_{11a} and 50% LP_{11b}, whereas in the actual case the percentage of the LP_{11b} (refer to Fig. 4.16) could be less than 50% and reduce the reflection strength of the $LP_{01\text{-}11}$.

Additionally, we display the simulated spectra of the other four remaining cross-axis TM-FBGs as well, with the same parameters used for X-7.5 in Fig. 4.19. Without mode-decomposition of each of the sample, here we skip the overlaying comparison with the measured spectra.

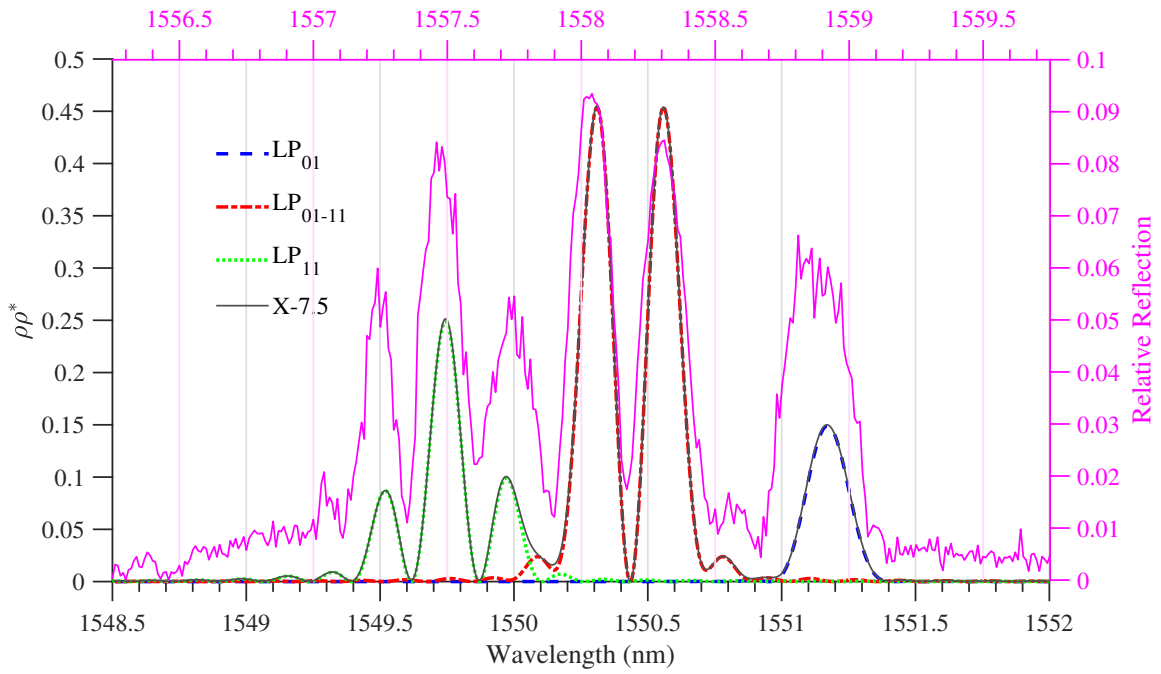

Figure 4.19: Simulated spectra of X-7.5 and the comparison with the experimentally measured spectrum.

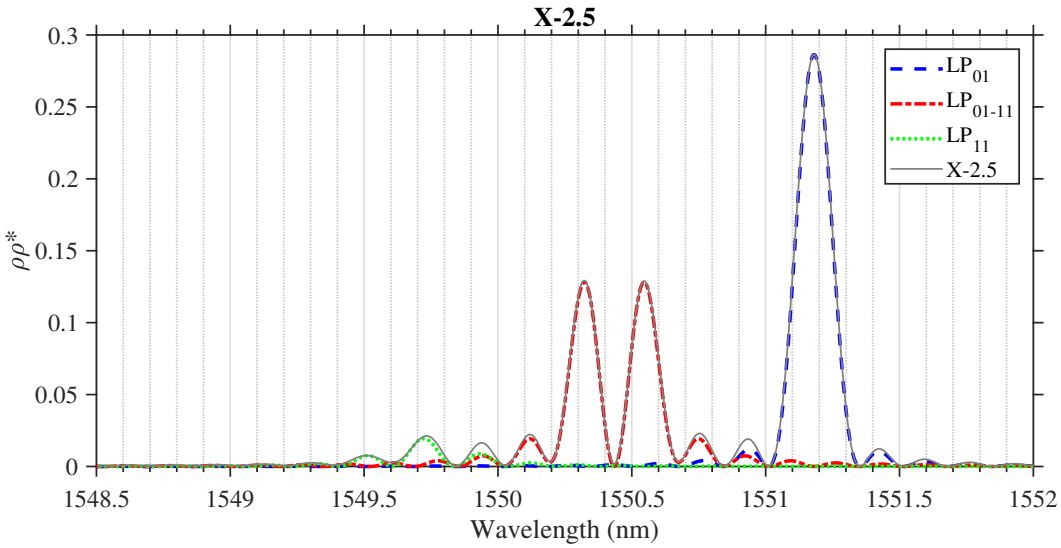

Figure 4.20: Simulated spectra of X-2.5.

In Fig. 4.24, we summarize the wavelength spacing of all samples from the experiments (Exp.) and simulations (Sim.). Simulated $\Delta\lambda$ is identified from the individual spectrum of

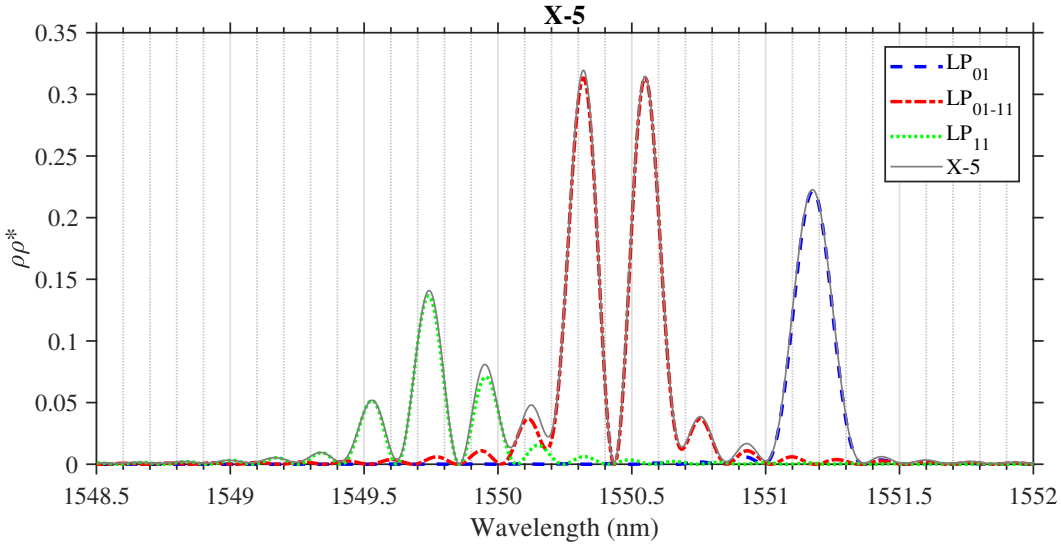

Figure 4.21: Simulated spectra of X-5.

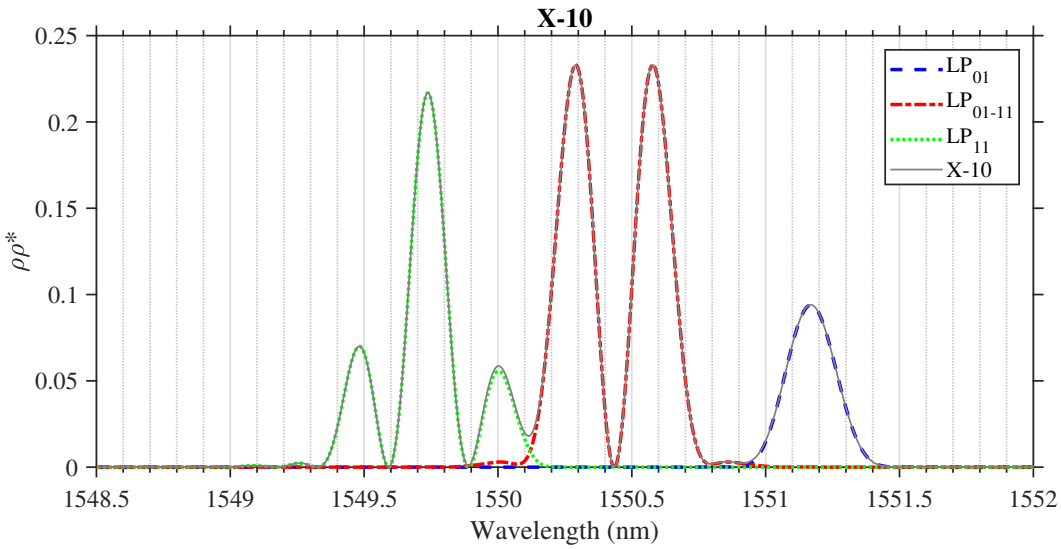

Figure 4.22: Simulated spectra of X-10.

the LP modes. The simulation is performed with varied values of Δn_v^{eq} listed in Table 4.1, and the standard deviation resulted from varied Δn_v^{eq} is used as the error bar. In general, the simulations are consistent with the experimental findings: All three $\Delta\lambda$ increase with increasing tilting angles, and $\Delta\lambda_{23}$ outnumbers the other two in each grating tested. The slight discrepancies are likely caused by inaccurate locating of the peak wavelengths exper-

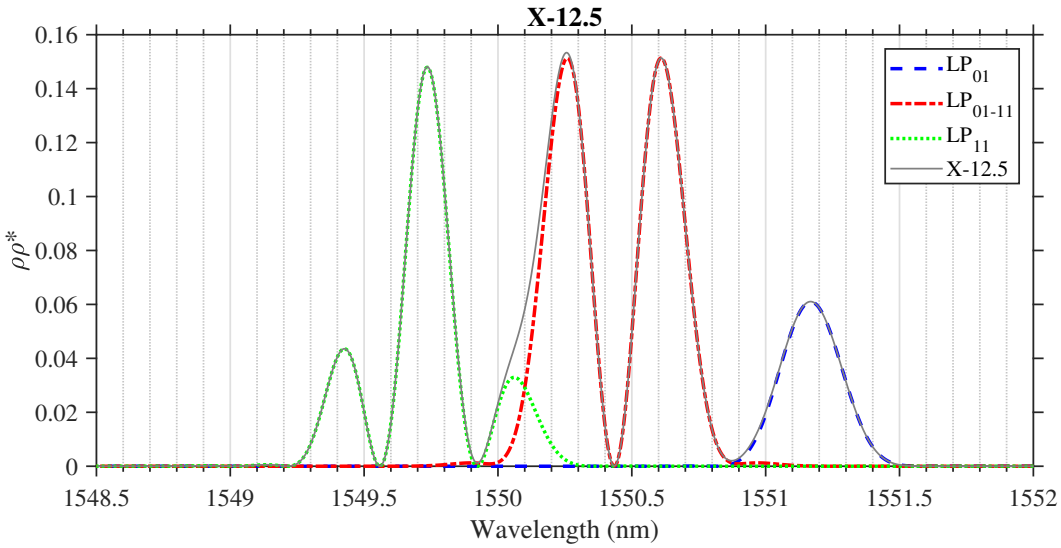

Figure 4.23: Simulated spectra of X-12.5.

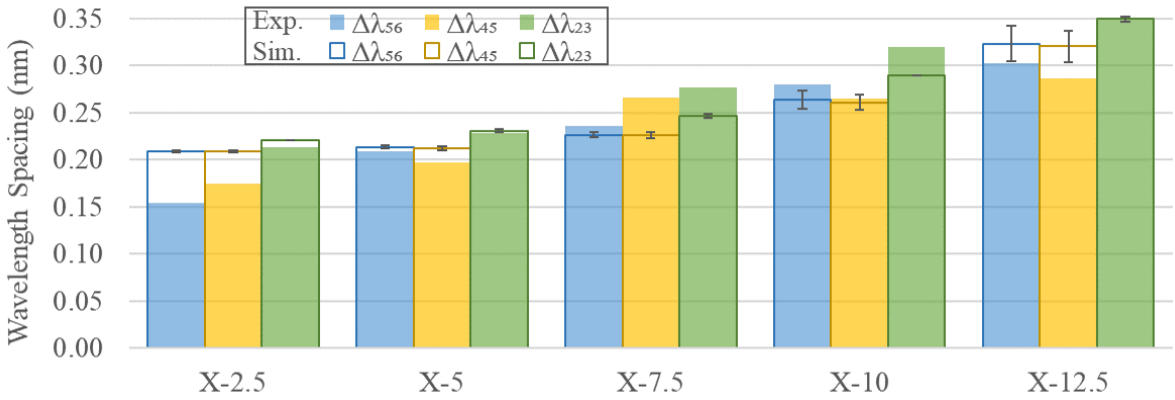

Figure 4.24: Comparison of the wavelength spacing between the experiments (Exp.) and simulations (Sim.).

imentally due to the noises. Furthermore, the experimentally measured spectra are in fact the sum of three individual spectrum of the LP_{01}, LP_{11}, and $LP_{01\text{-}11}$, the peak wavelengths identified from the sum-up spectra may differ slightly from those obtained from the individual spectrum in the simulations. Besides, the simulated $\Delta\lambda$ is obtained based on the parameters provided in Table 4.1, which can also be a source of the slight discrepancies.

4.4.4 Numerical investigation of cross-axis TM-FBGs on bending sensing

In this section, we present the numerical investigation of the feasibility of using our PbP cross-axis TM-FBGs for bending sensing. In brief, the bending can alter the the modal structure of at the bending area [7], as a consequence, as revealed by Eq. (4.6), so is the envelope function $K^{\text{env}}(z)$, which leads to the change of the reflection spectrum. Particularly, here we consider three different situations, where the bending radius (r_b) are 0, 1 cm, and 5 cm, one of the eigenmodes in three cases are plotted in Fig. 4.25, where the core-cladding interface is marked in white. The envelope function and the simulated spectra of the LP_{11}

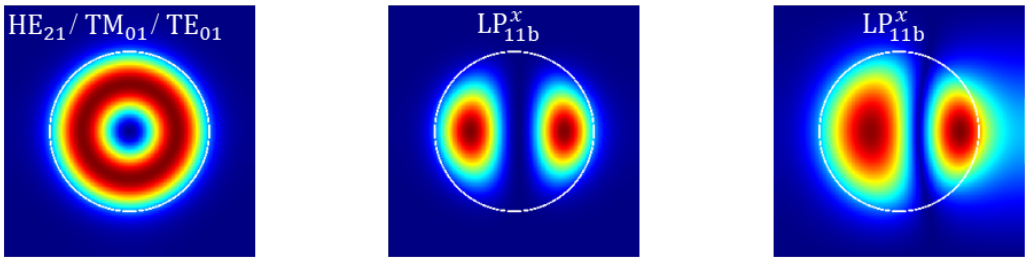

Figure 4.25: Representative eigenmode of a TMF with varied bending radius. (a) $r_b = 0$ (straight fiber), (b) $r_b = 5cm$, and (c) $r_b = 1cm$.

shown in Fig. 4.25 are plotted in Fig. 4.26 and Fig. 4.27, respectively. Since we are more interested in the relative change of the spectra under varied bending radius, it is reasonable here to directly set all other parameters as unity, such as the size of the damage points, the refractive index modulation induced by the laser pulses. As revealed in Fig. 4.27, the bending can indeed induce additional variation to the spectra, which has the potential to achieve simultaneous multi-parameter sensing with a single FBG.

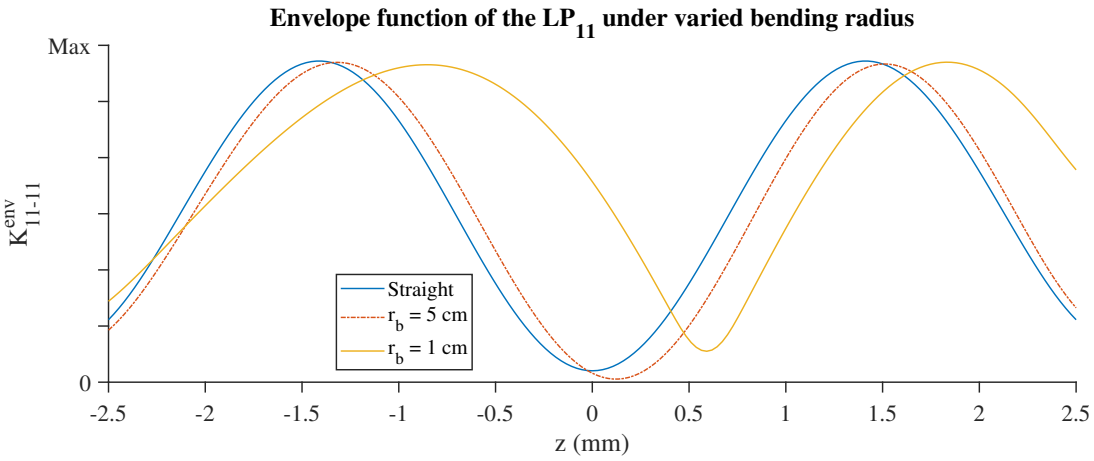

Figure 4.26: Envelope function of the LP_{11} under test.

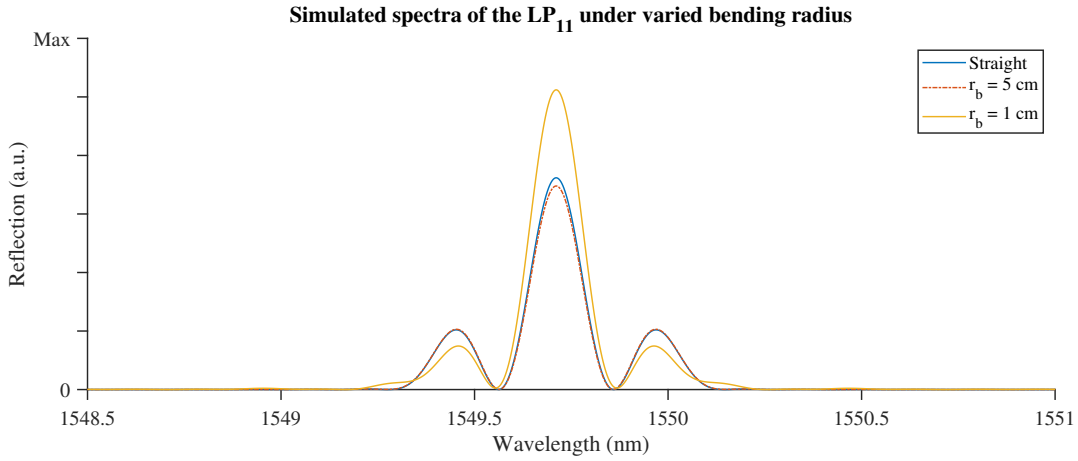

Figure 4.27: Simulated reflection spectra of the LP_{11} under test.

4.5 Conclusion

In summary, through a simple modulation of the perturbation profile along the FBG length, we show that HOMs can provide extra degrees of freedom for designing gratings with arbitrary frequency-response characteristics, which could benefit applications such as multi-channel dispersion compensators, wavelength-selective filters, as well as for fiber sensing [34, 64, 65, 66, 67]. We also develop a numerical model for the PbP-inscribed FBGs based on pulse-wave approximation and the standard coupled-wave analysis. This model can potentially offer a useful tool for the design of PbP FBGs with more complex perturbation profiles and more modes involved.

Chapter 5

Conclusions and Future Work

In this work, we numerically and experimentally investigate the off-axis and cross-axis FBGs in a step-index TMF fabricated by an FS laser PbP technique, through which we demonstrate that the HOMs of the optical fiber can add some extra degrees of freedom for device innovation.

Off-axis TM-FBGs

- Polarization-dependent reflectivity.

  For the off-axis FBGs, we find that the reflectivity of the the LP_{11} has strong polarization discrimination capability, with the much stronger reflectivity constantly corresponding to the polarization perpendicular to the line connecting the damage point and the fiber center. Such polarization discrimination can potentially benefit the fiber laser applications. For example, one can control the lasing lines in [35, 36, 37] simply by adjusting the polarization state of the injected light, instead of using an external polarization controller.

- Polarization-controlled mode patterns.

  Moreover, we report that the forward LP_{01} couples backwardly to only one spatial LP_{11} with dumb line parallel to the direction of linear polarization, through which one can manipulate the spatial orientation of the the radially asymmetric LP modes by

merely altering the polarization. With such capability, the transmission capacity of the MDM-based systems mentioned in [21, 22, 23, 24] can be further increased via selective mode excitation of arbitrarily oriented radially asymmetric LP modes. Furthermore, the spatial orientation manipulation can also be utilized for cylindrical vector beam [81] and orbital angular momentum [82, 83] generations which generally require two spatially orthogonal LP modes with certain phase delays, these can find applications in optical trapping and tweezers [84, 85, 86].

- Strong cross-coupling between modes.

  Besides, the rather high reflectivities of the cross-coupling of the off-axis FBGs can find immediate applications as mode converters such as in [31, 32, 87, 88], with the bandwidth increased by further chirp designs. Our characterization results also shed some light on the morphology of the structural changes induced by FS lasers.

Cross-axis TM-FBGs

- Tailoring grating's spectral response

  For the cross-axis FBGs, we find that the wavelength spacing can be tuned by the mode-dependent coupling-profile envelope, through which one can manipulate the reflection spectrum with the versatile numerical model we developed in Section 4.4, this may find applications in fiber laser technology and optical communication.

- Bending sensing

  Furthermore, as we numerically demonstrated in Section 4.4.4, the cross-axis TM-FBGs are capable for bending sensing, future work on this topic may include advanced design of the grating structure with the versatile numerical model we developed in Section 4.4 to improve the sensitivity and resolution.

Other topics

- PbP FBGs in a graded-index MMF

  As we show in Figs. 2.10–2.12, the intensity profile of a degenerate-mode group can be random even in a rather short section of an MMF, this is because of the coherent superposition of multiple LP modes identical propagation constant. Note that the FBGs were fabricated by UV irradiation, and therefore almost all LP mode can have nontrivial transverse overlap with the perturbation. Here we display the reflected mode intensity profiles of the MM-FBG shown in Fig. 2.9, inscribed with FS PbP technique in the same MMF shown in Figs. 2.10–2.12. All damage points are on the fiber axis. The higher reflection peaks are formed by the self-coupling of a single degenerate-mode group, and the relatively smaller ones are for cross-coupling. As one can see from Fig. 5.1, unlike the random fields shown in Figs. 2.10–2.12, the reflected mode pattern of one degenerate-mode group takes similar shape of a single LP mode that has the most concentrated field distribution, since the transverse overlap between the on-axis damage points and the less-concentrated higher-order LP modes within this particular degenerate-mode group can be trivial. The damage points therefore can act like an additional mode selector in a graded-index highly MMF and turn the MMF to an FMF.

- Estimation of the overall refractive index modulation of a single FS pulse

  We have reported multiple novel properties of the PbP TM-FBGs, particularly the polarization-dependent reflectivity and the polarization-controlled mode patterns, but with no exact physical mechanisms proposed. To fully understand these novel properties for future applications, it is essential one can characterize the refractive index modulation (RIM) induced by the FS laser. The numerical simulation we performed in Fig. 4.4 may shed some light on this topic, however, the numerical model itself is

developed based on certain assumptions and therefore induces additional uncertainties. Consequently, a direct measurement of the laser-induced RIM is preferred. We have employed the in-fiber Fabry-Perot (FP) interferometry for such purpose. In particular, we inscribed multiple identical damage points to-be-characterized inside an FP cavity, the RIM can hence be obtained from the difference of the optical path difference (OPD) of the FP cavity before and after the damage points were inscribed. A representative interferogram of a 1 mm FP cavity is shown in Fig. 5.2(a), with the raw data in blue, the ready-to-demodulate signal after denoising using a finite impulse bandpass filter [89] in orange. The demodulation is based on total-phase peak-tracking algorithm as outlined in [90], The demodulated OPDs are displayed in Fig. 5.2(b). This method indeed revealed the overall RIM to certain extent, however, the damage points may induce additional wavelength-dependent phase term resulting from the coupling between the core modes and the radiation modes. It is therefore necessary to either quantify such coupling, albeit weak in principle, or to further develop the demodulation algorithm for higher accuracy and hence less damage points are needed for demodulation.

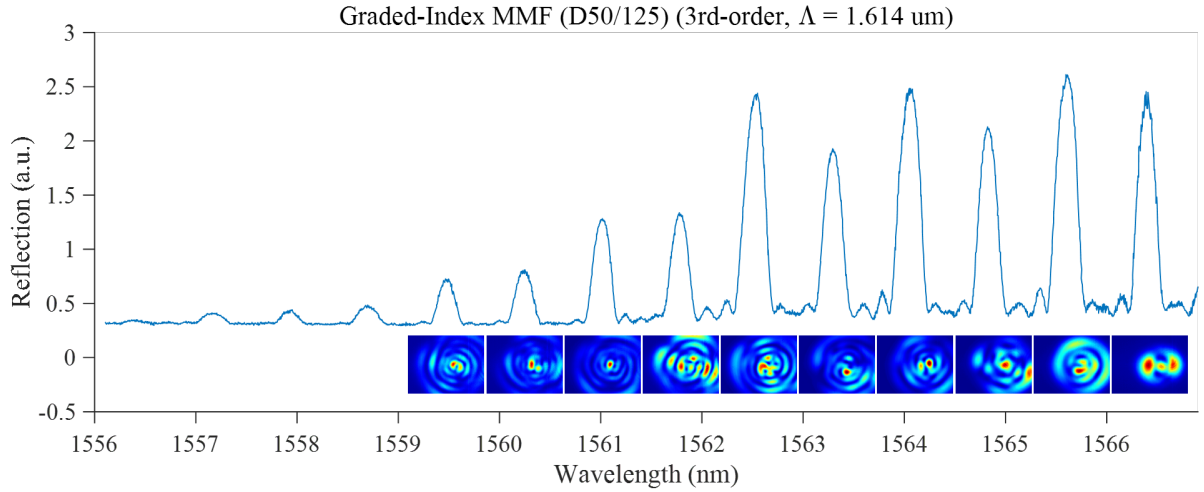

Figure 5.1: Reflection spectrum along with the reflected intensity profiles of an on-axis MM-FBG inscribed with FS PbP technique.

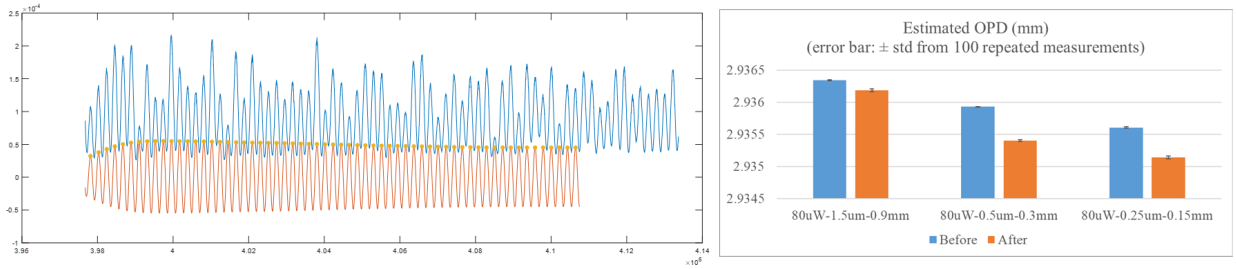

(a) (b)

Figure 5.2: (a) Interferogram of a 1-mm-long FP caivity. Blue: Measured trance; Orange: Denoised signal with peaks marked bu dots. (b) Demodulated OPDs before (blue) and after (orange) the damage points are inscribed. Format of the horizontal axis: Pulse average power-total length of the damage points-separation between two adjacent damage points.

Bibliography

[1] Tetsuya Miki and Hideki Ishio. Viabilities of the wavelength-division-multiplexing transmission system over an optical fiber cable. *IEEE Transactions on Communications*, 26(7):1082–1087, 1978.

[2] Joel Carpenter and Timothy D Wilkinson. All optical mode-multiplexing using holography and multimode fiber couplers. *Journal of Lightwave Technology*, 30(12):1978–1984, 2012.

[3] Tomáš Čižmár and Kishan Dholakia. Exploiting multimode waveguides for pure fibre-based imaging. *Nature communications*, 3(1):1–9, 2012.

[4] Ioannis N Papadopoulos, Salma Farahi, Christophe Moser, and Demetri Psaltis. Focusing and scanning light through a multimode optical fiber using digital phase conjugation. *Optics express*, 20(10):10583–10590, 2012.

[5] Rafael R Gattass and Eric Mazur. Femtosecond laser micromachining in transparent materials. *Nature photonics*, 2(4):219–225, 2008.

[6] A Martinez, Y Lai, M Dubov, IY Khrushchev, and I Bennion. Vector bending sensors based on fibre bragg gratings inscribed by infrared femtosecond laser. *Electronics Letters*, 41(8):472–474, 2005.

[7] Christian Waltermann, Konrad Bethmann, Alexander Doering, Yi Jiang, Anna Lena Baumann, Martin Angelmahr, and Wolfgang Schade. Multiple off-axis fiber bragg gratings for 3d shape sensing. *Applied optics*, 57(28):8125–8133, 2018.

[8] Yiping Wang, Ziliang Li, Shen Liu, Cailing Fu, Zhengyong Li, Zhe Zhang, Ying Wang, Jun He, Zhiyong Bai, and Changrui Liao. Parallel-integrated fiber bragg gratings inscribed by femtosecond laser point-by-point technology. *Journal of Lightwave Technology*, 37(10):2185–2193, 2019.

[9] Zhu Yong, Chun Zhan, Jon Lee, Shizhuo Yin, and Paul Ruffin. Multiple parameter vector bending and high-temperature sensors based on asymmetric multimode fiber bragg gratings inscribed by an infrared femtosecond laser. *Optics letters*, 31(12):1794–1796, 2006.

[10] Chun Zhan, Yong Zhu, Shizhuo Yin, and Paul Ruffin. Multi-parameter harsh environment sensing using asymmetric bragg gratings inscribed by ir femtosecond irradiation. *Optical Fiber Technology*, 13(2):98–107, 2007.

[11] Dan Su, Xueguang Qiao, Fengyi Chen, and Qiangzhou Rong. Higher order coupling mode for orientation-dependent bend measurement using an off-axis fbg inscription over few-mode fiber. *IEEE Sensors Journal*, 19(4):1368–1372, 2018.

[12] Graham D Marshall, Robert J Williams, Nemanja Jovanovic, MJ Steel, and Michael J Withford. Point-by-point written fiber-bragg gratings and their application in complex grating designs. *Optics express*, 18(19):19844–19859, 2010.

[13] Shuo Yang, Di Hu, and Anbo Wang. Point-by-point fabrication and characterization of sapphire fiber bragg gratings. *Optics letters*, 42(20):4219–4222, 2017.

[14] Robert J Williams, Nemanja Jovanovic, Graham D Marshall, and Michael J Withford. All-optical, actively q-switched fiber laser. *Optics express*, 18(8):7714–7723, 2010.

[15] Ryuichiro Goto, Robert J Williams, Nemanja Jovanovic, Graham D Marshall, Michael J Withford, and Stuart D Jackson. Linearly polarized fiber laser using a point-by-

point bragg grating in a single-polarization photonic bandgap fiber. *Optics letters*, 36(10):1872–1874, 2011.

[16] Nemanja Jovanovic, Alexander Fuerbach, Graham D Marshall, Michael J Withford, and Stuart D Jackson. Stable high-power continuous-wave yb 3+-doped silica fiber laser utilizing a point-by-point inscribed fiber bragg grating. *Optics letters*, 32(11):1486–1488, 2007.

[17] Toru Mizunami, Tzvetanka V Djambova, Tsutomu Niiho, and Sanjay Gupta. Bragg gratings in multimode and few-mode optical fibers. *Journal of lightwave technology*, 18(2):230–235, 2000.

[18] Tong Qiu, Islam Ashry, Anbo Wang, and Yong Xu. Adaptive control of degenerate mode groups in a highly multimode fiber. *IEEE Photonics Technology Letters*, 30(22):1976–1979, 2018.

[19] Amnon Yariv and Pochi Yeh. *Photonics: optical electronics in modern communications (the oxford series in electrical and computer engineering)*. Oxford University Press, Inc., 2006.

[20] Rodney S Tucker, Gadi Eisenstein, and Steven K Korotky. Optical time-division multiplexing for very high bit-rate transmission. *Journal of lightwave technology*, 6(11):1737–1749, 1988.

[21] S Berdagué and P Facq. Mode division multiplexing in optical fibers. *Applied Optics*, 21(11):1950–1955, 1982.

[22] Roland Ryf, Sebastian Randel, Alan H Gnauck, Cristian Bolle, Alberto Sierra, Sami Mumtaz, Mina Esmaeelpour, Ellsworth C Burrows, René-Jean Essiambre, Peter J

Winzer, et al. Mode-division multiplexing over 96 km of few-mode fiber using coherent 6×6 MIMO processing. *Journal of Lightwave technology*, 30(4):521–531, 2011.

[23] An Li, Yifei Wang, Jian Fang, Ming-Jun Li, Byoung Yoon Kim, and William Shieh. Few-mode fiber multi-parameter sensor with distributed temperature and strain discrimination. *Optics letters*, 40(7):1488–1491, 2015.

[24] Islam Ashry, Anbo Wang, and Yong Xu. Mode-division-multiplexing of absorption-based fiber optical sensors. *Optics Express*, 24(5):5186–5202, 2016.

[25] Sercan Ö Arık, Daulet Askarov, and Joseph M Kahn. Effect of mode coupling on signal processing complexity in mode-division multiplexing. *Journal of Lightwave Technology*, 31(3):423–431, 2013.

[26] Joel Carpenter, Benn C Thomsen, and Timothy D Wilkinson. Degenerate mode-group division multiplexing. *Journal of Lightwave Technology*, 30(24):3946–3952, 2012.

[27] Sergio G Leon-Saval, Alexander Argyros, and Joss Bland-Hawthorn. Photonic lanterns: a study of light propagation in multimode to single-mode converters. *Optics Express*, 18(8):8430–8439, 2010.

[28] Nicolas K Fontaine, Roland R Ryf, Sergio G Leon-Saval, and Joss Bland-Hawthorn. Evaluation of photonic lanterns for lossless mode-multiplexing. In *2012 38th European Conference and Exhibition on Optical Communications*, pages 1–3. IEEE, 2012.

[29] Peng Lu, Anbo Wang, Shay Soker, and Yong Xu. Adaptive mode control based on a fiber bragg grating. *Optics Letters*, 40(15):3488–3491, 2015.

[30] Tong Qiu, Islam Ashry, Anbo Wang, and Yong Xu. Adaptive mode control in 4-and 17-mode fibers. *IEEE Photonics Technology Letters*, 30(11):1036–1039, 2018.

[31] Chuang Wu, Zhengyong Liu, Kit Man Chung, Ming-Leung Vincent Tse, Florence YM Chan, Alan Pak Tao Lau, Chao Lu, and Haw-Yaw Tam. Strong LP_{01} and LP_{11} mutual coupling conversion in a two-mode fiber bragg grating. *IEEE Photonics Journal*, 4(4):1080–1086, 2012.

[32] Yueyu Han and Guijun Hu. A novel mux/demux based on few-mode fbg for mode division multiplexing system. *Optics Communications*, 367:161–166, 2016.

[33] Chun-Liu Zhao, Xiufeng Yang, MS Demokan, and Wei Jin. Simultaneous temperature and refractive index measurements using a 3 slanted multimode fiber bragg grating. *Journal of lightwave technology*, 24(2):879, 2006.

[34] Peng Lu, Islam Ashry, and Yong Xu. Adaptive mode control for few-mode fiber based sensors and sensor networks. *Journal of Lightwave Technology*, 35(16):3562–3568, 2016.

[35] Xinhuan Feng, Yange Liu, Shenggui Fu, Shuzhong Yuan, and Xiaoyi Dong. Switchable dual-wavelength ytterbium-doped fiber laser based on a few-mode fiber grating. *IEEE Photonics Technology Letters*, 16(3):762–764, 2004.

[36] Dae Seung Moon, Un-Chul Paek, and Youngjoo Chung. Multi-wavelength lasing oscillations in an erbium-doped fiber laser using few-mode fiber bragg grating. *Optics express*, 12(25):6147–6152, 2004.

[37] Jiangli Dong and Kin Seng Chiang. Mode-locked fiber laser with transverse-mode selection based on a two-mode fbg. *IEEE Photonics Technology Letters*, 26(17):1766–1769, 2014.

[38] KO Hill, Y Fujii, Derwyn C Johnson, and BS Kawasaki. Photosensitivity in optical fiber waveguides: Application to reflection filter fabrication. *Applied physics letters*, 32(10):647–649, 1978.

[39] Kenneth O Hill, B Malo, F Bilodeau, DC Johnson, and Jacques Albert. Bragg gratings fabricated in monomode photosensitive optical fiber by uv exposure through a phase mask. *Applied Physics Letters*, 62(10):1035–1037, 1993.

[40] B Malo, Kenneth O Hill, F Bilodeau, DC Johnson, and Jacques Albert. Point-by-point fabrication of micro-bragg gratings in photosensitive fibre using single excimer pulse refractive index modification techniques. *Electronics Letters*, 29(18):1668–1669, 1993.

[41] Ams Martinez, Mykhaylo Dubov, Igor Khrushchev, and Ian Bennion. Direct writing of fibre bragg gratings by femtosecond laser. *Electronics Letters*, 40(19):1170–1172, 2004.

[42] Eli N Glezer and Eric Mazur. Ultrafast-laser driven micro-explosions in transparent materials. *Applied physics letters*, 71(7):882–884, 1997.

[43] P Török, P Varga, Z Laczik, and GR Booker. Electromagnetic diffraction of light focused through a planar interface between materials of mismatched refractive indices: an integral representation. *JOSA A*, 12(2):325–332, 1995.

[44] P Maine, D Strickland, P Bado, M Pessot, and G Mourou. Generation of ultrahigh peak power pulses by chirped pulse amplification. *IEEE Journal of Quantum electronics*, 24(2):398–403, 1988.

[45] Amós Martinez, IY Khrushchev, and Ian Bennion. Thermal properties of fibre bragg gratings inscribed point-by-point by infrared femtosecond laser. *Electronics letters*, 41(4):176–178, 2005.

[46] Alessio Stefani, Matthias Stecher, Graham E Town, and Ole Bang. Direct writing of fiber bragg grating in microstructured polymer optical fiber. *IEEE Photonics Technology Letters*, 24(13):1148–1150, 2012.

[47] LB Fu, GD Marshall, JA Bolger, P Steinvurzel, EC Magi, MJ Withford, and BJ Eggleton. Femtosecond laser writing bragg gratings in pure silica photonic crystal fibres. *Electronics Letters*, 41(11):638–640, 2005.

[48] Elodie Wikszak, Jens Thomas, Jonas Burghoff, Bülend Ortaç, Jens Limpert, Stefan Nolte, Ulrike Fuchs, and Andreas Tünnermann. Erbium fiber laser based on intracore femtosecond-written fiber bragg grating. *Optics letters*, 31(16):2390–2392, 2006.

[49] D Homoelle, S Wielandy, Alexander L Gaeta, NF Borrelli, and Charlene Smith. Infrared photosensitivity in silica glasses exposed to femtosecond laser pulses. *Optics Letters*, 24(18):1311–1313, 1999.

[50] Kaiming Zhou, Mykhaylo Dubov, Chengbo Mou, Lin Zhang, Vladimir K Mezentsev, and Ian Bennion. Line-by-line fiber bragg grating made by femtosecond laser. *IEEE Photonics Technology Letters*, 22(16):1190–1192, 2010.

[51] Stephen J Mihailov, Christopher W Smelser, Ping Lu, Robert B Walker, Dan Grobnic, Huimin Ding, George Henderson, and James Unruh. Fiber bragg gratings made with a phase mask and 800-nm femtosecond radiation. *Optics letters*, 28(12):995–997, 2003.

[52] Jens U Thomas, Christian Voigtländer, Stefan Nolte, Andreas Tünnermann, Nemanja Jovanovic, Graham D Marshall, Michael J Withford, and Michael Steel. Mode selective fiber bragg gratings. In *Frontiers in Ultrafast Optics: Biomedical, Scientific, and Industrial Applications X*, volume 7589, page 75890J. International Society for Optics and Photonics, 2010.

[53] Markus Mundus, Jens U Thomas, Christian Voigtländer, Ria G Becker, Cesar Jauregui, Andreas Tünnermann, and Stefan Nolte. Cgh-based real-time analysis of fiber bragg gratings in few mode lma fibers. In *Fiber Lasers IX: Technology, Systems, and Ap-*

plications, volume 8237, page 823712. International Society for Optics and Photonics, 2012.

[54] Muhammad M Ali, Yongmin Jung, Kok-Sing Lim, Md R Islam, Shaif-Ul Alam, David J Richardson, and Harith Ahmad. Characterization of mode coupling in few-mode fbg with selective mode excitation. *IEEE Photonics Technology Letters*, 27(16):1713–1716, 2015.

[55] Amos Martinez, Michael Dubov, Igor Khrushchev, and Ian Bennion. Photoinduced modifications in fiber gratings inscribed directly by infrared femtosecond irradiation. *IEEE photonics technology letters*, 18(21):2266–2268, 2006.

[56] Mattias L Åslund, Nemanja Jovanovic, Nathaniel Groothoff, John Canning, Graham D Marshall, Stuart D Jackson, Alexander Fuerbach, and Michael J Withford. Optical loss mechanisms in femtosecond laser-written point-by-point fibre bragg gratings. *Optics express*, 16(18):14248–14254, 2008.

[57] Bahaa EA Saleh and Malvin Carl Teich. *Fundamentals of photonics*. john Wiley & sons, 2019.

[58] Shoji Asano and Giichi Yamamoto. Light scattering by a spheroidal particle. *Applied optics*, 14(1):29–49, 1975.

[59] Abdullah Rahnama, Keivan Mahmoud Aghdami, Young Hwan Kim, Erden Ertorer, and Peter R Herman. Ultra-compact'spectrometer-in-fiber'based on chirped filament-array gratings (conference presentation). In *Frontiers in Ultrafast Optics: Biomedical, Scientific, and Industrial Applications XX*, volume 11270, page 112700W. International Society for Optics and Photonics, 2020.

[60] Aaron Reupert, Maximilian Heck, Stefan Nolte, and Lothar Wondraczek. Angular

scattering pattern of femtosecond laser-induced refractive index modifications in optical fibers. *Advanced Optical Materials*, page 2000633, 2020.

[61] Shellee D Dyer, Paul A Williams, R Joseph Espejo, Jonathan D Kofler, and Shelley M Etzel. Fundamental limits in fiber bragg grating peak wavelength measurements. In *17th International Conference on Optical Fibre Sensors*, volume 5855, pages 88–93. International Society for Optics and Photonics, 2005.

[62] Nemanja Jovanovic, Jens Thomas, Robert J Williams, MJ Steel, Graham D Marshall, Alexander Fuerbach, Stefan Nolte, Andreas Tünnermann, and Michael J Withford. Polarization-dependent effects in point-by-point fiber bragg gratings enable simple, linearly polarized fiber lasers. *Optics express*, 17(8):6082–6095, 2009.

[63] Turan Erdogan. Fiber grating spectra. *Journal of lightwave technology*, 15(8):1277–1294, 1997.

[64] KO Hill. Aperiodic distributed-parameter waveguides for integrated optics. *Applied optics*, 13(8):1853–1856, 1974.

[65] KO Hill, F Bilodeau, B Malo, T Kitagawa, S Thériault, DC Johnson, Jacques Albert, and K Takiguchi. Chirped in-fiber bragg gratings for compensation of optical-fiber dispersion. *Optics letters*, 19(17):1314–1316, 1994.

[66] BJ Eggleton, PA Krug, L Poladian, and F Ouellette. Long periodic superstructure bragg gratings in optical fibres. *Electronics letters*, 30(19):1620–1622, 1994.

[67] Morten Ibsen, Michael K Durkin, Martin J Cole, and Richard I Laming. Sinc-sampled fiber bragg gratings for identical multiple wavelength operation. *IEEE Photonics Technology Letters*, 10(6):842–844, 1998.

[68] Alejandro Carballar, Miguel A Muriel, and J Azafi. Fiber grating filter for wdm systems: an improved design. *IEEE Photonics Technology Letters*, 11(6):694–696, 1999.

[69] Nemanja Jovanovic, Mattias Åslund, Alexander Fuerbach, Stuart D Jackson, Graham D Marshall, and Michael J Withford. Narrow linewidth, 100 w cw yb 3+-doped silica fiber laser with a point-by-point bragg grating inscribed directly into the active core. *Optics letters*, 32(19):2804–2806, 2007.

[70] Masanori Matsuhara and KO Hill. Optical-waveguide band-rejection filters: Design. *Applied Optics*, 13(12):2886–2888, 1974.

[71] Masanori Matsuhara, KO Hill, and Akira Watanabe. Optical-waveguide filters: Synthesis. *JOSA*, 65(7):804–809, 1975.

[72] Karin Ennser, N Zervas, and RL Laming. Optimization of apodized linearly chirped fiber gratings for optical communications. *IEEE Journal of Quantum Electronics*, 34(5):770–778, 1998.

[73] Yasuo Shibata, T Tamamura, S Oku, and Y Kondo. Coupling coefficient modulation of waveguide grating using sampled grating. *IEEE photonics technology letters*, 6(10):1222–1224, 1994.

[74] B Malo, S Theriault, DC Johnson, F Bilodeau, Jacques Albert, and KO Hill. Apodised in-fibre bragg grating reflectors photoimprinted using a phase mask. *Electronics Letters*, 31(3):223–225, 1995.

[75] J Albert, KO Hill, B Malo, S Theriault, F Bilodeau, DC Johnson, and LE Erickson. Apodisation of the spectral response of fibre bragg gratings using a phase mask with variable diffraction efficiency. *Electronics Letters*, 31(3):222–223, 1995.

[76] Stephen J Mihailov, Christopher W Smelser, Dan Grobnic, Robert B Walker, Ping Lu, Huimin Ding, and James Unruh. Bragg gratings written in all-sio2 and ge-doped core fibers with 800-nm femtosecond radiation and a phase mask. *Journal of Lightwave Technology*, 22(1):94, 2004.

[77] Robert J Williams, Christian Voigtländer, Graham D Marshall, Andreas Tünnermann, Stefan Nolte, MJ Steel, and Michael J Withford. Point-by-point inscription of apodized fiber bragg gratings. *Optics letters*, 36(15):2988–2990, 2011.

[78] Tong Qiu, Shuo Yang, and Anbo Wang. Experimental investigation of point-by-point off-axis bragg gratings inscribed by a femtosecond laser in few-mode fibers. *Optics Express*, 28(25):37553–37565, 2020.

[79] Herwig Kogelnik. Filter response of nonuniform almost-periodic structures. *Bell System Technical Journal*, 55(1):109–126, 1976.

[80] H Kogelnik. Theory of optical waveguides. In *Guided-wave optoelectronics*, pages 7–88. Springer, 1988.

[81] Pengfei Ma, Pu Zhou, Yanxing Ma, Xiaolin Wang, Rongtao Su, and Zejin Liu. Generation of azimuthally and radially polarized beams by coherent polarization beam combination. *Optics letters*, 37(13):2658–2660, 2012.

[82] Robert D Niederriter, Mark E Siemens, and Juliet T Gopinath. Continuously tunable orbital angular momentum generation using a polarization-maintaining fiber. *Optics Letters*, 41(14):3213–3216, 2016.

[83] Shuhui Li, Qi Mo, Xiao Hu, Cheng Du, and Jian Wang. Controllable all-fiber orbital angular momentum mode converter. *Optics letters*, 40(18):4376–4379, 2015.

[84] Arthur Ashkin and James M Dziedzic. Optical trapping and manipulation of viruses and bacteria. *Science*, 235(4795):1517–1520, 1987.

[85] Yu Zhang, Li Zhao, Yunhao Chen, Zhihai Liu, Yaxun Zhang, Enming Zhao, Jun Yang, and Libo Yuan. Single optical tweezers based on elliptical core fiber. *Optics Communications*, 365:103–107, 2016.

[86] Qi Mo, Zhikun Hong, Dawei Yu, Songnian Fu, Liang Wang, Kyunghwan Oh, Ming Tang, and Deming Liu. All-fiber spatial rotation manipulation for radially asymmetric modes. *Scientific reports*, 7(1):1–9, 2017.

[87] Ya Gao, Junqiang Sun, Guodong Chen, and Chaotan Sima. Demonstration of simultaneous mode conversion and demultiplexing for mode and wavelength division multiplexing systems based on tilted few-mode fiber bragg gratings. *Optics express*, 23(8):9959–9967, 2015.

[88] Muhammad Khairol Annuar Zaini, Yen-Sian Lee, Kok-Sing Lim, Nurul Asha Mohd Nazal, Hang-Zhou Yang, and Harith Ahmad. Enhanced optical delay line in few-mode fiber based on mode conversion using few-mode fiber bragg gratings. *IEEE Journal of Quantum Electronics*, 54(5):1–7, 2018.

[89] Fabin Shen and Anbo Wang. Frequency-estimation-based signal-processing algorithm for white-light optical fiber fabry–perot interferometers. *Applied optics*, 44(25):5206–5214, 2005.

[90] Cheng Ma, Evan M Lally, and Anbo Wang. Toward eliminating signal demodulation jumps in optical fiber intrinsic fabry–perot interferometric sensors. *Journal of lightwave technology*, 29(13):1913–1919, 2011.